

On Ultrasound Elastography: Simulation, Experiment, and Algorithm Development

A THESIS SUBMITTED TO
THE DEPARTMENT OF ELECTRONIC AND ELECTRICAL ENGINEERING
AND THE COMMITTEE FOR POSTGRADUATE STUDIES OF THE
UNIVERSITY OF STRATHCLYDE
FOR THE DEGREE OF
DOCTOR OF PHILOSOPHY

By
Aws Al-Azawi
June 2015

Declaration of Authenticity and Author's Rights

This thesis is the result of the author's original research. It has been composed by the author and has not been previously submitted for examination, which has led to the award of a degree. The copyright of this thesis belongs to the author under the terms of the United Kingdom Copyright Acts as qualified by University of Strathclyde Regulation 3.50. Due acknowledgement must always be made of the use of any material contained in, or derived from, this thesis.

Aws Al-azawi

June 2015

Acknowledgements

I would like to thank many people for their support and encouragement over the past few years.

First of all I would like to thank my supervisor Prof John Soraghan for his support and advice. I would also like to thank Associate Prof Reffat Hussian for his encouragement.

I would like to thank a PhD candidate Jerzy Dziewierz and Dr Scott Inglis for their help on implementing the experiment scenarios.

A special thank for Iraq ministry of higher education and scientific research for the financial support.

Finally to my wife and children, my parents, my brothers and their family, to the memory of my father in law Talal Al-Nujaify, to the memory of the dean of Mosul Engineering College Maan Shaker, to friends and colleagues.

Abstract

Ultrasound elastography is investigated in this thesis based on processing backscattered raw ultrasonic data (radio frequency signals) using standard cross-correlation tool (SCC). The data are obtained using separate simulation, and experiment. In the simulation scenario, ultrasound imaging is simulated using the Field-II program, while the deformation object is simulated using finite element modelling (FEM) of ANSYS-11 program. A composition algorithm is proposed that combine Field-II and ANSYS-11 programs to produce backscattered raw data before and after compression. The experimental scenario was performed in collaboration with the Centre for Ultrasound Engineering, University of Strathclyde using DYNARY ultrasonic Phased Array Controller (Zetec, Québec, Québec, Canada) and Tissue Mimicking Material (TMM), which was manufactured in the Medical Physics Department, Edinburgh Royal Infirmary. In the experiments, uniform compression was applied over the TMM object using an adaptor that employs the 10MHz transducer and the head of an XYZ scanner, while freehand compression is applied using 5MHz transducer.

A deformation estimation algorithm of displacement and a strain mapping algorithm have developed according to three levels of compression of 0.2%, 1%, and 2%-4%. The algorithm was assessed for the three stages based on the level of compression. In the first stage of 0.2% compression, backscattered raw data from a simulation model are utilized. Displacement and strain fields are estimated using the proposed deformation algorithm and then compared favourably with FEM numerical solution. In second stage of 1% compression, backscattered raw data of simulation and experiment models are utilized. Displacement and strain fields are estimated using the proposed novel deformation algorithm of refinement that includes the regularization for non-consistent measurements based on surrounding neighbours information. Results from simulation and experiment are compared, which shows a good agreement in terms of displacement field consistency and strain field contrast. In the third stage of 2%-4% compression, backscattered raw data of experiment are utilized. Displacement and strain fields are estimated using advance refinement process that involves an exclusion of estimation outliers. Displacement and strain

fields are compared with two dimensional (2D) median filter operation. Results show a superiority of the proposed algorithm over 2D median operation in terms of signal-to-noise ratio (SNR) and contrast-to-noise ratio (CNR). In the proposed algorithm, a small correlation window length is used to ensure sufficient spatial resolution of strain estimation.

Finally, the deformation estimation algorithm is validated using backscattered raw data of freehand compression. Result of freehand compression shows superiority against 2D median operation.

Contents

Declaration of Authenticity and Author's Rights	ii
Acknowledgements	iii
Abstract	iii
Contents	vi
List of Figures	ix
List of Tables	xiv
List of Abbreviations	xv
List of Symbols	xvii
1 Introduction	1
1.1 Diagnosis of Biological Tissue Disease	1
1.2 Motivation of Research	3
1.3 Summary of Original Contributions	4
1.4 Thesis Organization	6
2 Ultrasound Elastography	8
2.1 Introduction	8
2.2 Ultrasound System	9
2.2.1 Transducers	10
2.2.2 Phased array scanning modes (beam-forming)	10
2.2.3 Display Methods	12
2.2.4 Resolutions	15
2.3 Ultrasound Simulation	16
2.4 Artefacts in Elastography	18
2.5 Ultrasound Technology	20
2.6 Conclusion	25
3 Ultrasound Scattering	26
3.1 Introduction	26
3.2 Ultrasound Wave Propagation	27
3.2.1 Reflections of wave	27
3.3 Pulse-Echo Ultrasound Scattering	30
3.4 Fundamentals on tissue similarity measurement	33
3.4.1 Influence in similarity measurement of strained speckle signals	35
3.4.2 Strain estimation techniques	36
3.5 Similarity Compensation of Strained Speckle Signals	40
3.5.1 Axial compensation of strained speckle signals	42
3.5.2 Lateral/elevation compensation of strained speckle signals	43
3.5.3 Multi-step processing	44
3.6 Conclusion	44

4 Dynamic Ultrasound Scatterer Simulation Model	46
4.1 Introduction	46
4.2 Methodology	47
4.3 Field-II Simulation Model.....	49
4.3.1 Transducer model.....	49
4.3.2 Simulation model of biological tissue.....	52
4.3.3 Linear phased array scanning model.....	53
4.3.4 Raw data simulation model.....	55
4.4 FEM Simulation Model	58
4.4.1 Simulation model of biological tissue.....	58
4.4.2 Mechanical compression model.....	61
4.5 Composition Model of Field-II and FEM	61
4.6 Axial Displacement/Strain Fields Estimation	65
4.7 Results and Discussion.....	68
4.7.1 Small scale applied compression	68
4.7.2 Small correlation window length	73
4.7.3 Performance against 1% compression	75
4.8 Conclusion	76
5 Axial Displacement Field Regularization	78
5.1 Introduction	78
5.2 Refinement Process Method	79
5.2.1 Correlation windows length	81
5.2.2 Initial displacement field.....	85
5.2.3 Refinement process	87
5.2.4 SNR and CNR of strain.....	92
5.3 Materials.....	93
5.3.1 Raw data acquisition	93
5.3.2 Anthropomorphic phantom	94
5.3.3 Experiment scenario.....	96
5.4 Results and Discussion.....	97
5.4.1 Visual and quantitative comparison	97
5.4.2 Effectiveness of refinement parameters	100
5.4.3 Investigation of refinement process for simulation model.....	105
5.4.4 Performance against 2% compression	109
5.5 Conclusion	112

6 Large Scale Compression and Freehand Compression	113
6.1 Introduction	113
6.2 Estimation of Displacement and Strain.....	114
6.2.1 Difficulties into refinement operation.....	115
6.2.2 Exclusion of Estimation Outliers	117
6.3 Materials.....	121
6.4 Results and Discussion.....	123
6.4.1 Visual and quantitative comparison	123
6.4.2 Consistency robustness	134
6.4.3 Investigation of large-scale compression	137
6.4.4 Investigation of freehand compression	143
6.5 Conclusion	148
7 Conclusions and Future Works	149
7.1 Conclusions	149
7.2 Future Works.....	151
Appendix A	152
Author's Presentations and Publications	156
References	157

List of Figures

2.1	(a) Linear array transducer and (b) phase array transducer of linear scan and (c) sectorial scan	11
2.2	B-mode image of malignant patient breast	12
2.3	M-mode display for ROI of malignant patient breast	13
2.4	Simulation of biological soft tissue using Field II for, (a) three months foetus, (b) left kidney in longitudinal scan	14
2.5	(a) axial displacement field, (b) lateral displacement field	14
2.6	(a) axial strain field, (b) lateral strain field	15
2.7	Simulation of biological soft tissue using Field II for, (a) three months foetus, (b) left kidney in longitudinal scan	17
2.8	Illustration of signal processing artefacts of (a) zebra lines, (b) worm noise	19
2.9	General block-diagram of ultrasound technology	20
2.10	RF data formulation of linear scanning phased array transducer	22
2.11	IQ-demodulation and envelope detection	23
2.12	Ultrasound image formation with their corresponding (a) A-lines of RF-data (b) envelope-data (c) and logarithmic compression-data	24
3.1	Ultrasound wave experienced through acoustic homogeneous medium	29
3.2	Ultrasound wave travelling through acoustically heterogeneous medium	29
3.3	Geometry of wave function far away from scattering centre	30
3.4	Representation of incident k_i and scatter k_s vectors in spherical coordinates	33
3.5	Geometry of nearly incompressible object under axial compression .	36
3.6	Strain estimation using four displacement measurements	39
3.7	RF signals of pre-compression (solid line) and post-compression (dashed line) of, (a) window length of 7λ , (b) their corresponding correlation function, (c) window length of 25λ , and (d) their corresponding correlation function	41
4.1	Block diagram of proposed methodology	48
4.2	Main flowchart of linear array transducer modelling	50
4.3	(a) Linear phased array transducer aperture information and (b).pulse echo field	51
4.4	Randomly distributed scatterers position in 3D object	52
4.5	Flowchart of linear phased array scan model	53
4.6	Apodization methods of (a) Rectangular, (b) Hanning, and (c) Cosine-tapered	54
4.7	Linear phased array scan model of 128 transducer elements and 16 active elements, (a) single RF A-line, (b) image of RF-data with time uncorrected, and (c) image of RF-data with time corrected	56

4.8	Flowchart of raw data simulation model	57
4.9	(a) Linear phased array scan model of 128 transducer elements and 16 active elements, envelope raw A-line, (b) image of envelope raw-data , (c) Log envelope A-line, and (d) image of Log envelope –data	57
4.10	FEM simulation of nearly incompressible model, meshes responding before and after axial uniform compression, and (b) 3D mapping of displacement vectors	59
4.11	3D simulation of heterogeneous FEM model, cube inclusion (a), and cylinder inclusion (b)	60
4.12	Scatterer-nodes composition algorithm flowchart	62
4.13	Tetrahedral structure unit	63
4.14	Block diagram of axial displacement and strain estimation	66
4.15	(a) Proposed method of smoothing process and (b) displacement window set of averaging operation	67
4.16	(a) Non-interpolated, (b) FEM, (c) interpolated, (d) smoothing process	68
4.17	Non-smoothed displacement vector (dotted-line) and smoothed displacement vector	69
4.18	(a) Strain fields without smoothing process and (b) with smoothing process	70
4.19	(a) Heterogeneous model mapping of normalized correlation coefficient , (b) non-interpolated displacement , (c) displacement without smoothing , (d) strain without smoothing , (e) displacement with smoothing , and (f) strain with smoothing	71
4.20	Strain field of FEM heterogeneous model at 0.1mm compression ...	72
4.21	Heterogeneous model of 0.2 % compression, (a) displacement of 4λ and 50% , (b) strain, (c) displacement of 4λ and 80%, (d) strain	74
4.22	(a) Heterogeneous model at 1% compression, displacement of 10λ , (b) strain, (c) displacement of 5λ , (d) strain	76
5.1	Block diagram of proposed methodology	80
5.2	A segment of displacement field with certain 3x3 region of interest (highlighted by green colour) at, (a) non-optimal correlation windows length, (b) optimal correlation windows length. Symbol x represents estimation outlier, while symbol o represents correct estimation	82
5.3	Pre-compression (solid line) and post-compression (dashed line) RF signals of two different regions, (a) for high correlation, (b) correspondent correlation function, (c) low correlation and (d) correspondent correlation function	84
5.4	Sequential correlation windows (pre-compression and post-compression windows) are overlapped by 50% in each frame. The length of pre-compression window is slightly longer than post-compression one	85
5.5	Flowchart of displacement filed refinement process	87
5.6	Identification of the eight neighbours for different CUI locations ...	88

5.7	Diagram of experiment set up	93
5.8	Experiment scenario of, (a) initial and (b) applied compression	96
5.9	(a and b) Displacement and (c and d) strain (bottom) fields of homogeneous TMM, (a and c) without and (b and d) with refinement process. The yellow dashed triangle represents the region of interest for SNR calculation	97
5.10	Mean and STD (error bar) of strain region of interest with (solid line) and without (dashed line) refinement process	98
5.11	SNR of strain region of interest without (dashed line) and with (solid line) refinement process	99
5.12	(a and b) Displacement,(c and d) strain fields of heterogeneous TMM, (a and c) without and (b and d) with refinement process	100
5.13	CNR of strain region of interest without (dashed line) and with (solid line) refinement process	101
5.14	Strain field of homogeneous TMM for $T_{cd}=2$, 1.4 pre-to-post window length ratio and different correlation window length of (a) 4λ and (b) 5λ	102
5.15	Strain field of heterogeneous TMM without (left) and with refinement process (right) of $T_{cd}=4$, 1.4 pre-to-post window length ratio and different correlation window length of 2λ - 5λ from top to bottom	103
5.16	(a, c, e) Displacement and (b, d, f) strain fields of heterogeneous TMM for 3λ correlation window length and 1.6 pre-to-post-window length ratio of, (a and b) without refinement process, with refinement process $T_{cd}=4$ (c and d) $T_{rd}=0.1$, and of (e and f) $T_{rd}=0$.	104
5.17	(a, c) Displacement and (b, d) strain fields of heterogeneous simulation model for 1% applied compression, correlation window length, 1.4 pre-to-post window length ratio, (a and b) without refinement process, with refinement process of $T_{rd}=0.03$, $T_{cd}=4$	106
5.18	(a and c) Displacement and (b and d) strain fields of heterogeneous simulation model for 1% applied compression, 3λ correlation window length, 1.8 pre-to-post window length ratio, (a and b)without refinement process, with refinement process of $T_{rd}=0.03$, $T_{cd}=4$	107
5.19	(a and c) Displacement and (b and d) strain fields of heterogeneous simulation model for 1% applied compression. Using 3λ correlation window length, 1.9 pre-to-post window length ratio. (a and b) without refinement process and (c and d) with refinement process of $T_{rd}=0.03$, $T_{cd}=4$	112
5.20	(a, c) Displacement and (b, d) strain fields of heterogeneous TMM for 2% applied compression, 5λ correlation window length, 1.4 pre-to-post window length ratio, (a and b) without refinement process, with refinement process of $T_{rd}=0.03$, $T_{cd}=4$	114
5.21	(a, c) Displacement and (b, d) strain fields of heterogeneous TMM for 2% applied compression, 8λ correlation window length, 1.4 pre-to-post window length ratio, (a and b) without refinement process,	

	with refinement process of $T_{rd}=0.03, T_{cd}=4$	115
6.1	Noise block occupations and, (a-d) median filter operation for 3x3 dimensions, (e-g) refinement operation	116
6.2	Flowchart of displacement recalculation process	118
6.3	Heterogeneous TMM under compression scenarios are performed using (a) uniform compressions, (b) freehand with transducer-plate adaptor and (c) freehand with transducer only	122
6.4	(a,c,e) Displacement and (b,d,f) strain (right column) fields of homogeneous TMM (a and b) without refinement, (c and d) median filter and (e and f) with refinement processes	124
6.5	Histogram of correlation coefficients (a) at 3λ of equal correlation windows length and (b) at 3λ correlation window length and 1.6 pre-to-post window length ratio (c and d) correlation coefficient map, and (e and f) displacement field	126
6.6	SNR as a function of cross window length for non-refinement (dotted line), median filter (solid line), and refinement (dash-dot line) processes	127
6.7	SNR as a function of cross window length for non-refinement (dotted line), median filter (solid line), and refinement (dash-dot line) processes	129
6.8	(a,c,e) Displacement and (b,d,f) strain fields of heterogeneous TMM, (a and b)without refinement, (c and d)median filter and (e and f) with refinement processes	131
6.9	CNR as a function of cross window length for non-refinement (dotted line), median filter (solid line), and refinement (dash-dot line) processes	133
6.10	Refined strain profile of (a) $T_{rd}=0.03$ solid line and $T_{rd}=0.1$ dotted line, (b) $T_{rd}=0.03$ solid line and $T_{rd}=0.2$ dotted line, (c) $T_{rd}=0.03$ solid line $T_{rd}=0.3$ and dotted line	134
6.11	Refined strain profile of (a) $T_{cd}=0$ dotted line, $T_{cd}=2$ dash-dot line and $T_{cd}=4$ solid line, (b) $T_{cd}=4$ solid line, $T_{cd}=6$ dotted line and $T_{cd}=8$ dash-dot line	135
6.12	Refined strain profile of (a) $T_{cc}=0.04$ solid line and $T_{cc}=0.1$ dash-dot line. (b) $T_{cc}=0.04$ solid line and $T_{cc}=0.2$ dash-dot line. (c) $T_{cc}=0.04$ solid line and $T_{cc}=0.3$ dash-dot line	136
6.13	(a,c,e) Displacement and (b,d, f) strain fields of heterogeneous TMM (a and b) without refinement, (c and d) median filter and (e and f) with refinement processes at 2% applied compression	138
6.14	(a, c, e) Displacement and (b, d, f) strain fields of heterogeneous TMM (a and b) without refinement, (c and d) median filter and (e and f) with refinement processes at 3% applied compression	140
6.15	(a, c, e) Displacement and (b, d, f) strain fields of heterogeneous TMM (a and b) without refinement, (c and d) median filter and (e and f) with refinement processes at 4% applied compression	142

6.16	(a, c e) Displacement and (b, d f) strain fields of freehand compression over heterogeneous TMM using 5MHz transducer-plate adapter, raw data process (a and b) without refinement, (c and d) median filter and (e and f) with refinement	144
6.17	(a, c e) Displacement and (b, d f) strain fields of freehand compression over heterogeneous TMM using 5MHz transducer-plate adapter, raw data process (a and b) without refinement, (c and d) median filter and (e and f) with refinement	145
6.18	(a, c e) Displacement and (b, d f) strain fields of freehand compression over heterogeneous TMM using 5MHz transducer, raw data process (a and b) without refinement, (c and d) median filter and (e and f) with refinement	147

List of Tables

5.1	Estimation of initial displacement	86
5.2	Refinement process	91
5.3	Strain estimation based LSQSE	92
5.4	Standard components of the IEC 61685 agar-based tissue mimicking material	95
6.1	Estimation of initial displacement	114
6.2	Refinement process with recalculation of inconsistent estimation	120
6.3	Setting parameters of DYNARY imaging system	121

List of Abbreviations

A/D	Analog-to-digital convertor
ACR	American college of radiology
C	Binary output vector
CNR	Contrast-to-noise ratio
CRLB	Cramér–Rao lower bound
CUI	Cell under interest
1D	One dimension
2D	Two dimension
3D	Three dimension
DICOM	Digital Imaging and Communications in Medicine
FEM	Finite element method
IQ	In-phase and quadrature-phase receiver
LPF	Low pass filter
LSQSE	Least square strain estimator
NCC	Normalized cross correlation
NEMA	National electrical manufacturers Association
PAL/SECAM	Phase Alternating Line/Sequential Colour with Memory
PSF	Point spread function
RF	Radio frequency
R_L	Length ratio

SAD	Sum absolute difference
SCC	Standard cross correlation
SUI	Segment under interest
SNR	Signal-to-noise ratio
SSD	Sum square difference
TGC	Time gain composition
TMM	Tissue mimicking material

List of Symbols

B_o	Adiabatic compressibility
B_i	Binary output vector
C	Counter of ones
C_o	Wave velocity
CLP	Classifier lower pointer
CUP	Classifier upper pointer
Cov	Covariance
d_{CUI}	Displacement of the cell under interest
d_{N_i}	Displacement of the neighbour index i
d_{NS}	Displacement vector of the neighbours that have survived (considered as neighbours have consistent displacement)
d_{SN_j}	Displacement vector of sorted neighbours
F	Constitution formula
k	Wave number
k_i	Incident vector
k_s	Scatter vector
l_o	Length of windows overlapping
L_a	Window length after compression
L_b	Window length before compression

$mean$	Mean value
n_{pre}	Additive noise in pre-compression state
n_{post}	Additive noise in post-compression state
NC_i	Normalized comparison vector
N_i	Neighbour of index (i)
NLC_j	Normalized comparison vector of lower rank
NUC_j	Normalized comparison vector of upper rank
p	Pressure perturbation wave
p_i	Incident pressure wave
p_o	Amplitude of pressure wave
p_s	Scattering pressure wave
q	Density distribution
\bar{q}	Spatial mean value of density
\tilde{q}	Spatial variation in density
Q	Objective quadratic function
r_{pre}	Radio frequency signal of pre-compression
r_{post}	Radio frequency signal of post-compression
R_{SCC}	Standard cross correlation function
R_{NCC}	Normalized cross correlation function

R_{SAD}	Sum absolute difference function
R_{SSD}	Sum square difference function
std	Standard deviation
S	Strain
S_i	Strain value for inclusion region of interest
S_b	Strain value for background region of interest
t	Time
T	Tissue impulse response
T_{cd}	Consistency decision threshold
T_{rd}	Row dependent threshold
T_{cc}	Consistency classifier threshold
V	Volume
Var	Variance
$V(t)$	Received signal
x	Direction of wave propagation
x_i	Independent parameter of depth for index (i)
y	Perpendicular direction of wave propagation
y_i	Dependent parameter of displacement for index (i)
α	Consistency comparison threshold

ν	Gradient parameter
$\hat{\nu}$	Optimal estimator of ν
δ	Intersection parameter
$\hat{\delta}$	Optimal estimator of δ
\emptyset	Empty set
γ	Classifier threshold
ω_{dem}	Demodulated angular frequency
ω	Angular frequency
τ	Time delay
λ	Wavelength
$\tilde{\beta}$	Spatial variation in compressibility
$\bar{\beta}$	Spatial mean value of compressibility
ψ	Scattering angle
ϕ	Azimuth angle
θ	Elevation angle
θ_i	Incident angle θ
θ_s	Scattering angle of θ
ψ_i	Incident angle of ψ
ψ_s	Scattering angle of ψ

Chapter 1

Introduction

1.1 Diagnosis of Biological Tissue Disease

Although worldwide authorities have provided sufficient legislations and funds toward reducing the mortality rate caused by tissue diseases of cancer and heart fibrosis, these diseases remain some of the most threatening of life. Some tissue diseases are examined by external test (palpation) while other are considered as non-palpable requiring an internal observation by imaging or laboratory test of specimen samples. Palpation by a physician is a common method for the detection of relatively large or superficial mass of malignancy, while heart global function is commonly diagnosed using ECG diagram and echocardiography. Currently there is a growing interest in the medical profession is the early detection of biological tissue disease by determination of malignancy's region and size to be removed by surgical operation. Furthermore, local function assessment of the heart disease can also influence the level of healing [4]. This challenge motivates collaboration between medical, physics and engineering disciplines.

Imaging techniques were introduced as remote sensing modality to view inside the body. Mammography is the most effective imaging modality particularly for early diagnosis of breast cancer, which provides a higher spatial resolution than other imaging modalities. However, the technology of ionizing radiation can have a damaging effect on exposed healthy tissues. In addition, the sensitivity of mammography is less accurate for dense breast [5] and its inconvenience procedure result in many women not using the screening [6]. Mammogram diagnostic report may recommend further examination and tests such as ultrasound or biopsy to make sure of the type of tumour.

Ultrasound imaging was introduced as a non-invasive remote sensing modality for imaging soft tissue such as breast, liver, kidney, prostate, heart, etc. The standard ultrasound imaging utilized to differentiate tissue diseased regions is based on noticeable ultrasonic echogenicity variation, which is in some cases are difficult to notice. In ultrasound imaging, an inter-observer variability caused researchers to investigate an elasticity called elastography [7, 8]. Ultrasonic elastography, was introduced based on mechanical attributes for imaging tissue compliance [9, 10] in small/non-palpable suspicious mass of 5-20mm diameter [11] which can subsequently reduce the requirement of biopsy laboratory tests [8]. In ultrasound elastography, stress stimulus is essential to induce a tissue deformation that can be mapped by tracking of narrow band scattered (RF-echo) signals before and after deformation. Stress stimulus of a passive organ is conducted by applying external compression using the transducer itself, such as breast, prostate, liver, kidney, etc. [10, 12]. While active organs such as the heart acts as a self-stimulus as it dynamically progresses through the pumping interval [4, 13, 14]. Generally, stiff tissue region experiences low strain that can be differentiated from higher strain surrounding normal tissue background [3]. Cardiac elastogram was found to be useful for myocardial regional function assessment, which reduces expert dependency on early detection of myocardial infraction [4].

In addition, *magnetic resonance imaging* (MRI) was also developed to map the tissue elasticity which is called *magnetic resonance elastography* (MRE) based on shear wave imaging. MRE has some advantages relative to ultrasound elastography, however ultrasound is preferred in terms of expense, real time capabilities and mobility [15].

1.2 Motivation of Research

The motivation behind this research is the potentials of ultrasound imaging in medical applications. This importance is demonstrated in the current utilization of ultrasound imaging for different human ages and body organs. This reflects a big trust in its performance in terms of accuracy and health safety, even though there are other imaging technologies have been discovered later, ultrasound has its own unique attributes. These attributes can be summarised as follows; real time imaging, less expensive, non-invasive, mobility, and degree of comfort.

The main aim of this research is to develop new signal-processing methods that use raw echo data for an estimation of elastic map of biological tissue, with the objective of moving from global to regional assessment of heart function and at the same time an early detection of breast tissue disease by addressing the following specific issues:

- i. Constructing a simulation model which combines ultrasound imaging program of Field-II and finite element analysis program of ANSYS-11, to provide the raw ultrasound data before and after compression.
- ii. Constructing an experimental set-up that includes the use of an ultrasound system of DYNARAY and tissue mimicking phantom, to provide the raw data before and after compression.
- iii. Using standard signal-processing tool in low complexity situations that adapts the algorithm parameters and upgrades its structure for more complex situations.
- iv. Investigation of algorithm performance against complex situation that is analogous to clinic practice situation.

1.3 Summary of Original Contributions

The knowledge contribution of this research study reinforces the field of biomedical signal and image processing, particularly in the field of ultrasound imaging of medical application. In addition, the research outcome is not limited for this particular field, but also can be extended for other related physical meaning of imaging and engineering technologies. The original contributions in this thesis can be summarized as follows:

1. Simulation model Scenario-A is proposed to create raw data that measures the before and after compression (deformation) sample. The simulation model of scenario-A combines Field-II program of ultrasound imaging and ANSYS-11 program of finite element analysis. A frame of raw data before applying compression is created by Field-II model of phased linear-array scan, while a frame after applying compression is created using same Field-II model for the new scatterer positions, which are moved according to displacement information of ANSYS-11 model. The ANSYS-11 model is set up to be homogeneous and nearly incompressible and is compressed by 0.2%. The raw data before and after compression are processed using a new proposed algorithm to estimate the deformation fields (displacement and strain). This deformation estimation algorithm uses standard cross-correlation to estimate the displacement field, which is smoothed using moving average window before strain estimation. The strain field is estimated using a gradient operation.
2. Simulation model of scenario-B comprises a heterogeneous (hard inclusion) and nearly incompressible design, which is compressed by 0.2% and 1%. Performance of the deformation estimation algorithm is investigated for the simulation model of scenario-B.
3. An experimental model of scenario I was designed and carried out in collaboration with the Centre for Ultrasonic Engineering, Dept. Electronic and Electrical Engineering, University of Strathclyde. The experimental apparatus used was an ultrasound phased array system of DYNARAY which

was used for phased linear-array scanning of tissue mimicking phantom model that has been manufactured in Dept Medical Physics, Edinburgh Royal Infirmary. Raw data was acquired before compression of 1% applied by XYZ controller. The raw data of before and after compression are processed using a second version of deformation estimation algorithm. The second version of deformation estimation algorithm used standard cross-correlation to estimate the displacement field, which was regularized using proposed refinement process before strain estimation. Strain field was estimated using least square approach.

4. The refined version of deformation estimation algorithm was further investigated using raw data created from simulation model of scenario-B.
5. Experiment model of scenario-II was carried out in the similar set-up of scenario-I at higher applied compression of 2%, 3%, and 4%. Raw data was acquired before compression that was applied using the XYZ controller. The raw data before and after compression was processed using new version of the deformation estimation algorithm. This third version of deformation estimation algorithm used a robust regularization process of displacement field before strain estimation. Robustness was achieved by refining sorted neighbours before applying the median operation. Strain field was estimated using least square approach.
6. For a clinic practice situation, experiment model of scenario-III was carried out for freehand compression over the heterogeneous model of tissue mimicking phantom. The robustness of the third version of deformation estimation algorithm was investigated using the data acquired from experiment model of scenario-III.

1.4 Thesis Organization

The remainder of this thesis is organized as follows;

Chapter 2 provides an overview of ultrasound imaging. Fundamentals of ultrasound system is explained in section 2.2, which includes transducer definition, phase array scanning, displaying methods, and resolution definition. Artefacts in ultrasound elastography are also explained in section 2.3. Ultrasound technology used to access raw data for advance processing such as speckle tracking and Doppler measurements is presented in section 2.3.

Chapter 3 reviews ultrasound scattering. A fundamental of ultrasound body interaction is introduced in section 3.2, which includes wave propagation equation and the principles of wave reflection. Scattering principles of pulse echo ultrasound is also explained in section 3.3. Speckle tracking approaches for similarity measurement are also reviewed in section 3.4.

Chapter 4 includes the simulation models of scenario-A and scenario-B, which uses ultrasound simulation programme of Field-II (section 4.3) and finite element analysis of ANSYS-11 (section 4.4). The simulation model combines these two programmes by proposed compensation algorithm (section 4.5). The first version of deformation estimation algorithm is also included in this chapter (section 4.6). Results and discussion are also provided in section 4.7.

Chapter 5 describes the experiment model of scenario-I. In this experiment scenario, phased linear array scanning is performed using DYNARAY system. Raw data is acquired using a 10MHz probe of 128 elements. Compression of 1% is applied axial using XYZ controller over the upper surface of the tissue mimicking phantoms of homogeneous and heterogeneous models. An analytic description of the second version of deformation estimation algorithm is presented in section 5.2. Experiment materials are described in section 5.3. Results and discussion are also provided in section 5.4, which is also includes the performance investigation of second version of the algorithm for the situation of simulation model of scenario-B.

Chapter 6 describes the experiment model of scenario-II. In this experiment scenario, phased linear array scanning is performed using DYNARAY system. Raw data are acquired using 10MHz probe of 128 elements. Compression of 2%, 3%, and 4% are applied axial using XYZ controller over the upper surface of the tissue mimicking phantoms of homogeneous and heterogeneous models. An analytical description of the third version of the deformation estimation algorithm is also described in section 6.2. Details of the experiment materials are provided in section 6.3. Results and discussion are also provided in section 6.4, which is also includes the performance investigation of third version of the algorithm for the situation of freehand compression.

Chapter 7 provides conclusions to the thesis outcomes of simulation, experiment, and proposed algorithms. This chapter also describes a plan of the future works that can highlight the main points to extend some of the work in the project.

Chapter 2

Ultrasound Elastography

2.1 Introduction

Ultrasound imaging is a common imaging modality that has been used in many different fields due to its physical property of propagation through materials. Ultrasound waves causes oscillations in material particles which ultimately produce a sequential difference in pressure areas called “compressional” and “rarefactional” [16]. Normally, ultrasound is used in diagnosis of biological tissue by displaying a series of images in real time known as sonograms that represent an intensity of reflected (backscattered) waves.

Modern diagnostic ultrasound systems provide a new dimension of diagnostic information known as strain map. The strain map identifies the size and location of stiff diseased regions that has been embedded in soft normal tissue background which are difficult to be recognized in sonogram [17], particularly at early stage of disease. Even in the advanced stage of the disease, it is not straight forward to classify the disease as benign or malignant using sonograms as it is subject to observer variability [8, 18]. There are many experimental studies that have been conducted for elastic map of various body organs, such as breast [8], prostate [19], liver [20], brain [21], kidney, ablation monitoring [1], and heart [4, 22-25]. Although these experiments were performed, most of ultrasound elastography techniques have not clinically proven [26].

Ultrasound elasticity or elastography is an imaging technique of mapping tissue elasticity, which was developed from the concept of palpation. Palpation is a clinic technique for sensing an existence of underneath tissue stiffness by hand pressing over a tissue region of interest. Accordingly the physician assesses tissue to be

normal or tumorous [17]. Elastography was introduced to address palpation challenges of tissue accessibility, quantitative assessment, certain range of tumour size, and frequent need for biopsy [8].

There are three main types of ultrasound elastography, quasi-static, dynamic, and organic [17]. In this thesis, a quasi-static approach is considered which is based on tracking of ultrasound backscatter before and after tissue mechanical stimulation by static compression. An axial elastogram is formed from a similarity comparison of a gated pre and post-compression RF-echo signals using cross-correlation [27-29]. The lags are representing a regional displacement map of tissue under compression. Consequently, displacement gradient is considered as a regional strain map [27, 30].

In this chapter, the fundamentals of ultrasound imaging will be considered from an elastography point of view, in terms of the following: ultrasound imaging system, artefacts in elasticity imaging, and ultrasound technology, finally conclusion will be provided to highlight the main points.

2.2 Ultrasound System

Pulse echo ranging began during World War II. RADAR is a term to describe a system that applied electromagnetic wave for radio detection and ranging. Development in pulse echo ranging was then extended to underwater target detection using ultrasound known as sound navigation and ranging SONAR. After World War II, ultrasound was used for probing the human body. In medical diagnosis, the principle of using pulse echo ultrasound is analogous to RADAR and SONAR [15]. Waves are transmitted through a medium and the backscatter from the target recorded. Diagnostic ultrasound system operates in the frequency band of 2-18 MHz as continuous or pulse waveform. This chapter focuses on pulse echo ultrasound exclusively.

2.2.1 Transducers

An ultrasound transducer (medical probe) is a sensing device that is used for transmitting and receiving of RF pulses. The transducer is mainly made from an array of piezoelectric crystal elements that converts alternating electrical current into oscillating ultrasound waves and vice versa. In medical applications, transducers are categorized based on elements feeding techniques (beam-forming), as linear array and phased array. Basically, linear array transducers are designed by linearly setting of elements number (typically 128 elements), each element is designed for certain focusing point and beamwidth (lateral resolution). Linear array scanning provides a high frame rate, where all elements activate in one time as illustrated in Figure 2. 1(a). On the other hand, electronic scanning is used in phased array transducers, where the focusing point, beamwidth, and beam steering angle are programmed according to the focal law. The focal law of phased array transducer is performed by applying different time delays to the elements to create a constant phase front based on constructive interference [31]. Phased array techniques provide flexibility for universal body organ imaging even though a small window of observation.

2.2.2 Phased array scanning modes (beam-forming)

Generally there are two phased array scanning techniques, linear scan and sectorial scan. In linear scan, equi-spaced groups of elements from the total number of elements are activated in each shot to perform a certain radiation field that interacts with the medium under imaging to form the echo A-line. Sequential activation of same element number is incremented by one step element toward the direction of scanning, which is formulating the targeted field by stacking the echoes of digitized A-lines, Figure 2. 1(b).

In the sectorial scan mode, the scanning scenario is performed by simultaneous activation of all elements. Beam angle changes according to the focal law that can be adjusted in programmable way. In this scenario, scanning performs a greater field using a smaller aperture window, Figure 2. 1(c).

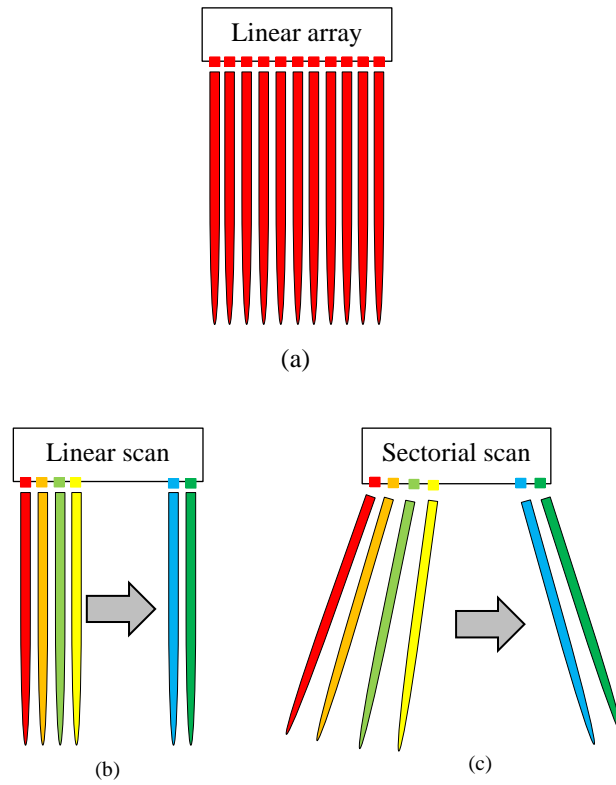


Figure 2. 1 (a) Linear array transducer and phase array transducer of (b) linear scan and (c) sectorial scan.

2.2.3 Display Methods

In echo ultrasound, there are three modes of display that may be categorized according to the purpose of indication as, A-mode, B-mode, and M-mode [32]. Elastography is displayed in two common fields of displacement and strain that describes the tissue regional function.

A. Echo Display Modes

Echo signals are picked-up by transducers and then displayed on three different modes namely A-mode, B-mode and M-mode.

A-mode is the display of envelope detected echo amplitude as function of depth (time of arrival) for single shot. In medical application, the utility of A-mode is limited due to a lagging on direction and size (cross-section) of object of interest. However, it was used in early echo display and also used for some studies like ophthalmology to detect an optic nerve. Figure 2. 2 shows raw envelop detected of echo ultrasound signal for certain depth (see the red line in Figure 2. 3), of malignant patient breast that has examined using linear array transducer from Siemens AntaresTM Ultrasound System, hence data is provided by Insana Lab/ University of Illinois.

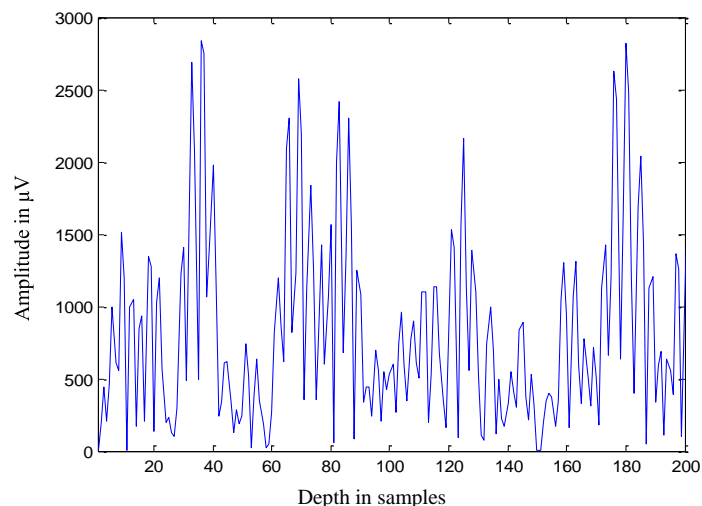


Figure 2. 2 A-mode for certain depth of patient breast malignant tumor.

B-mode is a general usage mode that represents a brightness image of echo amplitude or intensity. In brightness mode, sequential A-modes are aligned together, where the brightness image is formulated in grey scale. In Figure 2. 3, B-mode image is shown on intensity scale of dB, for malignant patient breast region of interest that has been provided by Insana Lab/ University of Illinois, where horizontal and vertical axes represent width (360 lines) and depth (1556 samples) respectively. Basically, horizontal axis line of the image represents lateral resolution (beamwidth in mm), while vertical axis pixel depicts axial resolution (depth in mm), and range of grey scale characterizes echo strength. B-mode provides an ability to sight cross section of body organ, the cross section can be recognized in terms of tissue region and edges. Edges are constructed from boundary reflection, while the tissue region is constructed from scattering of small irregularities [33].

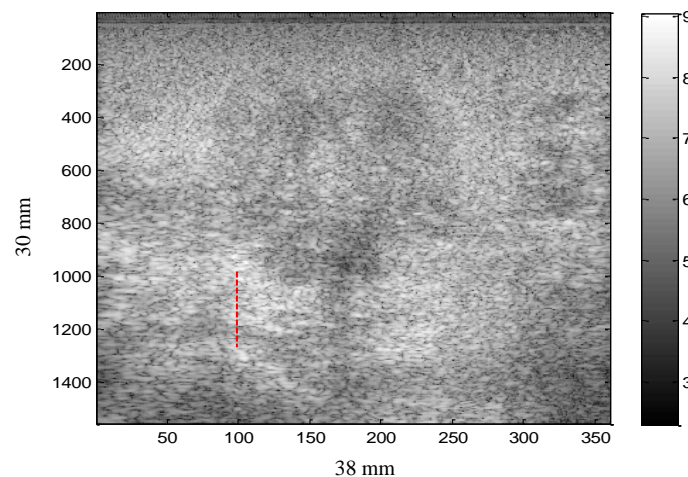


Figure 2. 3 B-mode image of malignant patient breast.

M-mode is a temporal indication of echo amplitude to verify the region of interest contraction (motion ability), particularly for cardiac and foetus imaging. Figure 2. 4 shows M-mode display of the region of interest that has been highlighted in red vertical line in Figure 2. 3. 180 frames are acquired during a 12 second using a linear transducer array of 17 fps (frame rate) from malignant patient breast region of interest under freehand compression by transducer face. It is clear that the breast lesion contraction is highly conducted for frame range (1-30), and then the movement of the lesion is reduced for the frame range (40-98), while no contraction

is appeared from frame 99 to the end. This is a simple example to display the tissue contraction using M-mode.

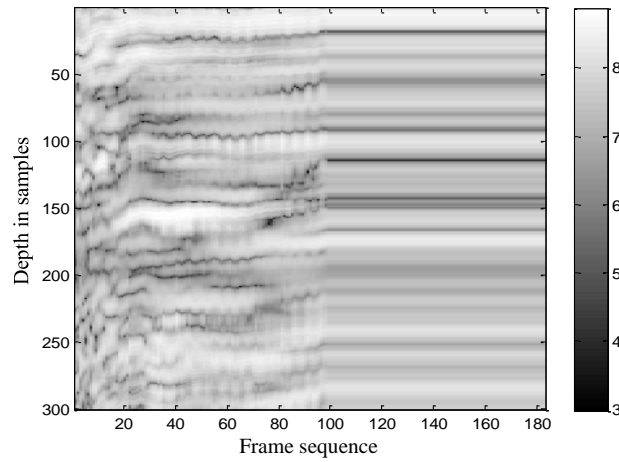


Figure 2. 4 M-mode display for ROI of malignant patient breast.

B. Elastography Display Map

Displacement-map is a distribution field of biological tissue scatterers' motion that describes regional axial displacement (in the direction of mechanical stimulation) Figure 2. 5(a) and lateral displacement (perpendicular to the direction of mechanical stimulation) Figure 2. 5(b) [9].

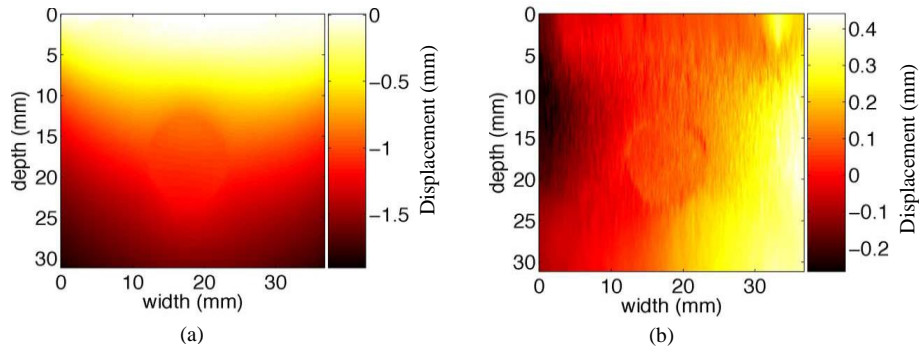


Figure 2. 5 (a) axial displacement field, (b) lateral displacement field [1].

Strain-map is a stress distribution of the biological tissue region of interest that describes a spatial variation due to mechanical stimulation Figure 2. 6. Strain can be determined by either indirect estimation based displacement gradient [9, 30] or direct estimation wavelet transform [34], iterative phase [35], and based spectral shift [36].

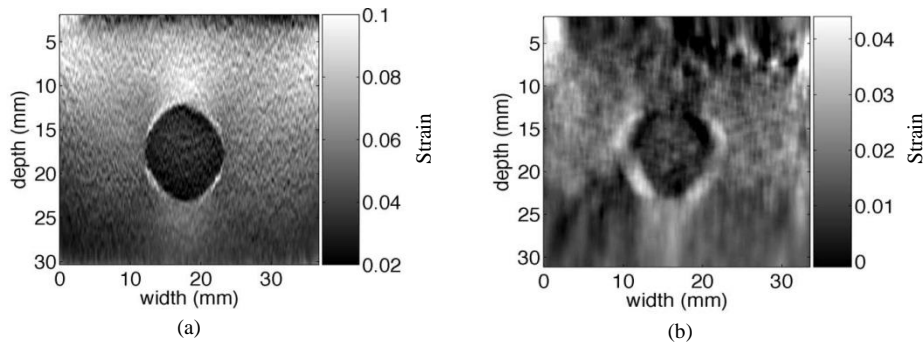


Figure 2. 6 (a) axial strain field, (b) lateral strain field [1].

2.2.4 Resolutions

In imaging, resolution is considered as a standard performance measurement, particularly in ultrasound imaging (sonography). In general, resolution is defined as an ability to recognize a certain event in spatial/temporal domains. The spatial domain is defined relative to the direction of radiation beam as axial and lateral resolutions, while temporal domain is verified according to capturing of certain instant event which is conducted by a resonant time frame rate. From an elastography point of view, resolution is considered to be an algorithmic performance measure of merit [37], which reflects an ability to recognize elastic property of two closely regions of interest, in axial/lateral orientations relative to direction of incidence and stimulation.

Axial resolution is an ability to determine a relative location of two close objects in the direction of wave propagation. Axial resolution is directly proportion to a spatial pulse length. The latter is improved by increasing an operating frequency, at an expense of degradation in a body penetration (increasing attenuation) particularly in paediatric ultrasound which uses relatively high frequencies. In elastography, axial resolution is influenced by signal processing parameter such as cross correlation

window length, at the expense of decorrelation noise development [38]. Axial resolution in elastography is found to be less than in sonography.

Lateral resolution is an ability to distinguish two objects that are located perpendicular to the direction of beam propagation. This is limited by radiation beamwidth that is inherently in lower order than axial resolution. Lateral resolution is directly proportion to the operating frequency and inversely proportion to gain. In elastography, lateral resolution is recognized in a same order of sonography lateral resolution [39], and that was the reason to ignore lateral strain map, however some robust speckle tracking algorithm have been developed based on interpolation to provide good enough lateral resolution of strain map [39, 40].

Temporal resolution is the transient capturing of a particular event during time series imaging, as example of cardiac left ventricle contraction, cardiac valve movements, etc. Frame rate adjustment can be used to alter the time resolution and can be performed manually by resonant adjustment of minimum pulse repetition frequency, limiting sector around area of interest, minimizing line density (keep certain lateral resolution).

2.3 Ultrasound Simulation

Simulation models are regarded as a standard framework for wide range of research areas, particularly in the area that deals with biological tissues. In this particular area, there is a limitation that relates to the patient agreement, case availability, and ultrasound scanner, but otherwise processing of real data might presuppose more information that enhances features and this sometimes add extra complexity. Field-II is an ultrasound imaging program that has been used in this work [41, 42]. Field-II program determines the transmitted and pulse-echo fields for a wide range of transducers, such as linear array and phased array transducers. In addition, the program is capable of simulating arbitrary linear imaging as well as biological tissue imaging, such as foetus, kidney, and cyst phantoms. Figure 2. 7

shows two examples of simulation model of biological soft tissues, foetus and kidney that have been simulated using Field-II program.

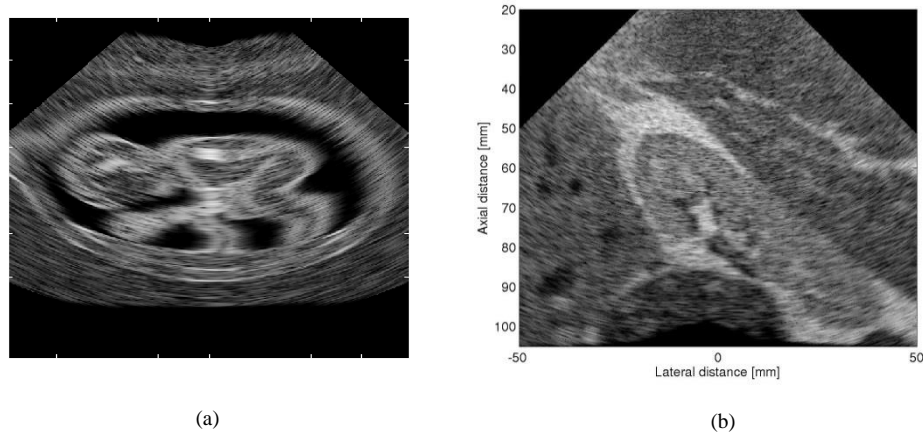


Figure 2. 7 Simulation of biological soft tissue using Field II for, (a) three months fetus, (b) left kidney in longitudinal scan [2].

In speckle tracking, scatterers are excited dynamically by applying an axial compression over an object of interest and then pulse-echo imaging is performed sequentially to produce frames of before and after applied compression. The Field-II program deals with scatterers as static particles that are compatible for image analysis. For flow measurement, a dynamic scatterer is required, in which the Field-II program may be developed in terms of scatterer motion and data acquisition in real time [43, 44]. In [43], parallel processing was considered to reduce the simulation time. In [44], reduction in simulation time is obtained by considering a grid approximation convolution. In this methodology a constant Point Spread Function (PSF) is assumed whereas a spatial varying PSF is actually realized. Finite Element Modelling (FEM) has been used in simulations of complicated dynamic engineering problems [45].

As in speckle tracking, the speckle is repositioned according to the FEM model [46], the model is adequate for impulsive radiation force and is validated using phantom tissue experiments. In [46], a hexahedron method of FEM model was used on

meshing the simulated homogeneous phantom where the displacement vectors of the eight surrounding nodes were interpolated to translate each scatterer in Field-II model. Further models have been developed for homogeneous and heterogeneous nearly incompressible media under external compression using both of FEM and Field-II simulation programs for linear array [47] and phase array [25] transducers.

In addition, a reliability of Field-II for speckle tracking was approved by comparing the deformation field with FEM [47] and also with phantom experiments [25]. In [25], the author does not refer to the methodology of moving the scatterers according to the FEM model. In the same way, the effect of decorrelation noise was reduced by ignoring an out of plane motion (motion in elevation direction) of the scatterers, this situation might effect on the reliability of the simulation model relative to the experiment.

2.4 Artefacts in Elastography

Medical imaging artefacts refers to any unwanted component that appears on a display that might lead to confusion in clinician interpretation [48]. In particular, ultrasound imaging encounters common artefacts due to its inherent operator dependence that leads to considerable inter- and intra-variability. In elastography, these common imaging artefacts also affect the quality of elastogram, and are termed acoustic artefacts. In addition, elastography involves additional artefacts, which are related to mechanical action and signal processing limitations. Accordingly, the additional artefacts termed mechanical artefacts and signal processing artefacts [49].

Acoustic artefacts are apparent errors that have been caused by the parameters of the sonogram system. Sonography artefacts may be categorized as follows: (1) beam artefacts in terms of beamwidth, side lobe and grating lobe, (2) multiple reflections artefacts due to closely located strong reflectors, (3) echogenic artefacts due to errors in assumption of constant speed and in time compensation of depth dependent attenuation [48]. Although these artefacts can affect the quality of elastogram,

however the correlation nature between acquired raw data before and after compression can minimize the effect of these common artefacts [3].

Signal processing artefact are unwanted components that appear on the elastogram (strain map) in form of the zebra lines and worm noise [3]. The zebra lines Figure 2. 8(a) comprise cyclic biased errors of black and white over the entire strain map, the repetition of these lines are directly proportional with the strain [50]. The reason of zebra artefact is the limitation of using discrete signals, where time delay is not aligned with integral multiples of sampling period, even though the sampling period increased [51]. However, this cyclic error was reduced by increasing the precision delay estimation using parabolic interpolation.

In addition, worm noise Figure 2. 8(b) occurs as a result of signal processing operation of sequential large cross correlation window overlap to produce a good enough spatial resolution of strain estimation. This type of signal processing artefact is shown to be also occurred as lines in strain map, but it differs from the zebra lines by thin and short structure and independent of strain [3].

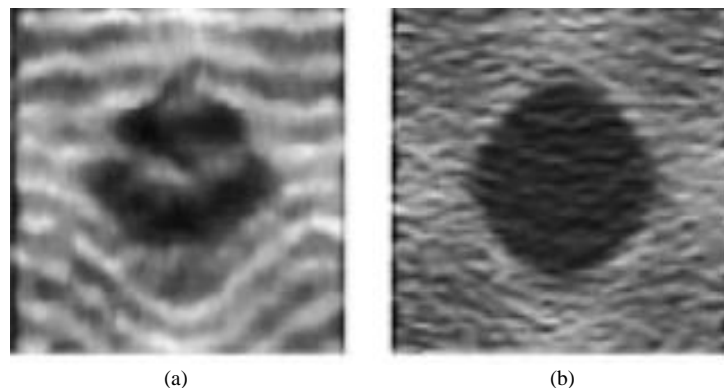


Figure 2. 8 Illustration of signal processing artifacts of (a) zebra lines, (b) worm noise [3].

Mechanical artefact has a significant influence on the strain variations. Strain variation in the object, mainly depends on the mechanical properties of the elastic modulus and boundary conditions. This category of artefact dose not just hinder the accuracy of the strain measurement, it may change the strain variation subjectively,

while sometimes supports the objective of the test by highlighting the inclusion (mass) region of interest [3].

In freehand compression, real time processing can play objectively to restore a subjective influence of mechanical artefact, by changing a scale of applied compression and an orientation of imaging probe.

2.5 Ultrasound Technology

Today's ultrasonic technology provides ultrasound systems for different applications. Medical applications have particular importance in ultrasound system design due to acoustic wave interaction with human body that provides instantaneous information for real time data processing. Figure 2. 9 demonstrates a block diagram of the RF data processing that has been ended by display. Display indicates organ region of interest that describes valuable information that can help physiologist on diagnose the organ state. In the past, researchers only were able to analyse Digital Imaging and Communications in Medicine (DICOM), which is considered as a back-end image data. Indeed, DICOM data is only useful for non-coherent processing, while coherent processing is able to produce a new diagnostic approach for diseases. Recently, technology addresses this limitation by producing a modern ultrasound imaging system for research institutions to conduct their contributions objectively in real life state. This new technology provides direct access to the raw data to be utilized for research purposes. In this thesis, radio frequency RF data is provided using AntaresTM system [52, 53] manufactured for medical application, while experiments are carried-out using DYNARAY system [54] manufactured for deferent applications .Both these two systems provide direct access to the RF data. In this section, the block diagram of the general medical ultrasound system is illustrated in Figure 2. 9.

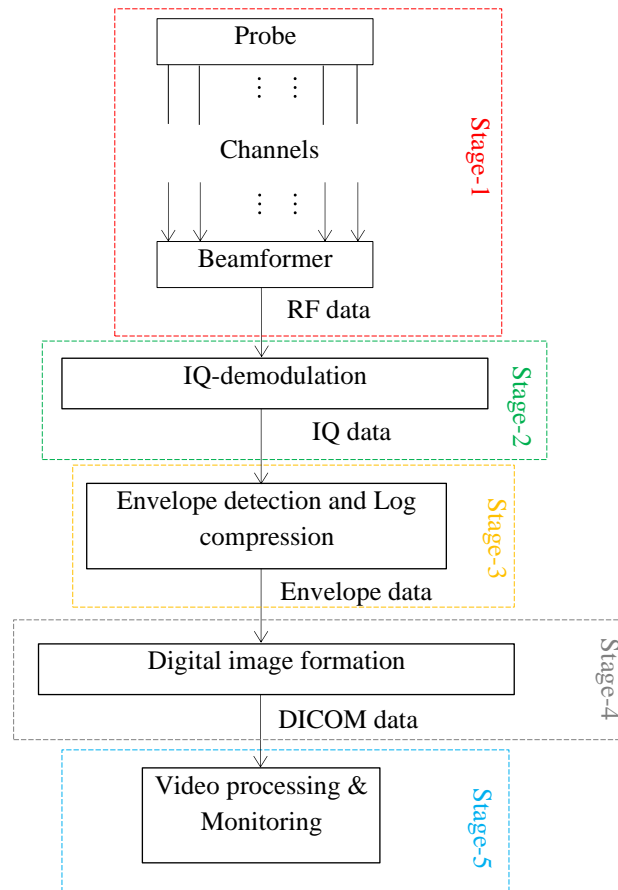


Figure 2. 9 Block-diagram of ultrasound technology.

Stage-1 is considered as a front-end stage, where the sensors send ultrasound waves through an object region of interest and then the reflections are received. A sensing probe (transducer) consists of piezoelectric elements that convert pressure variations into electric signals. Signals are supplied to the beamforming unit through the channels see Figure 2. 9 (stage-1).

- Beamforming times compensate the signals during an activation of channels in sending and receiving sessions. In the compensation, individual series of operations are performed for each analogue signal channel, where Time Gain Compensation (TGC) is considered proportional to the depth, conversion to digital signal, signal delayed for certain depth and direction and finally weighted to attain the required beam apodization. The RF signal line is constructed by summation of phase aligned signals of compensation process, see Figure 2. 10.

Stage-2 is a coherent process that demodulates the RF signal to IQ-signal by preserving the phase and amplitude information at lower frequency band. IQ-data signal can be obtained by multiplication of the RF-signal by complex exponential signal ($e^{(-j\omega t)}$) of demodulated angular frequency (ω_{dem}). For hardware implementation the mixing sinusoidal signal can be multiplied by the RF input to form in-phase signal channel, while 90° phase shifted sinusoid multiplied to form quadratic signal channel as illustrated in Figure 2. 11.

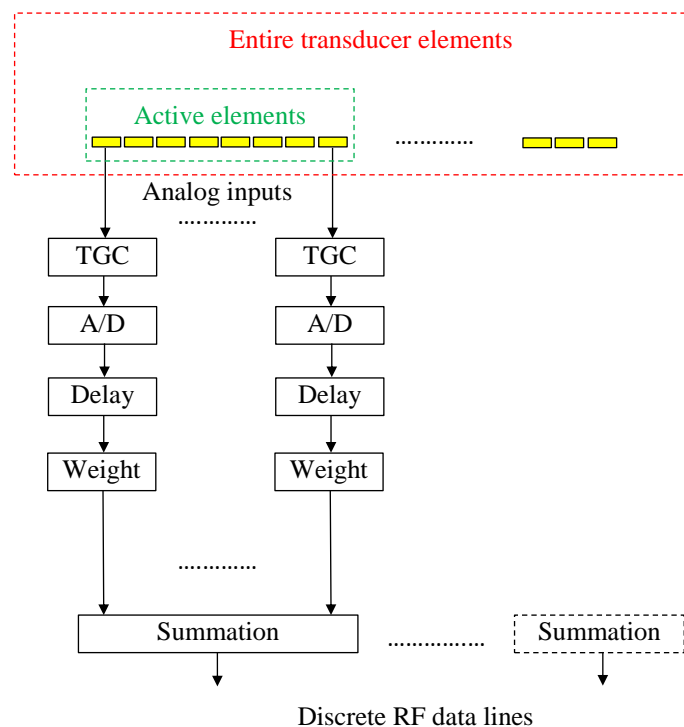


Figure 2. 10 RF data formulation of linear scanning phased array transducer.

Stage-3 comprises non-coherent processes that filters the complex signal to obtain the desired frequency spectrum by removing unwanted frequency components. The resulting envelope detection and logarithmic compression are performed to produce the final grey scale display as B-mode image, see Figure 2. 11.

Stage-4 is a digital image formation standard for archiving and communication that is termed DICOM, which has been published by the American College of Radiology (ACR) and the National Electrical Manufacturers Association (NEMA). Since 1993, DICOM has been a standard platform in US hospitals that archives patient and imaging modality data and it distributed through the networks. In EUROPE since 1995, DICOM was adopted as the standard medical imaging format.

Stage-5 video processing of consecutive B-mode frames for monitor compatibility, such as PAL/SECAM systems.

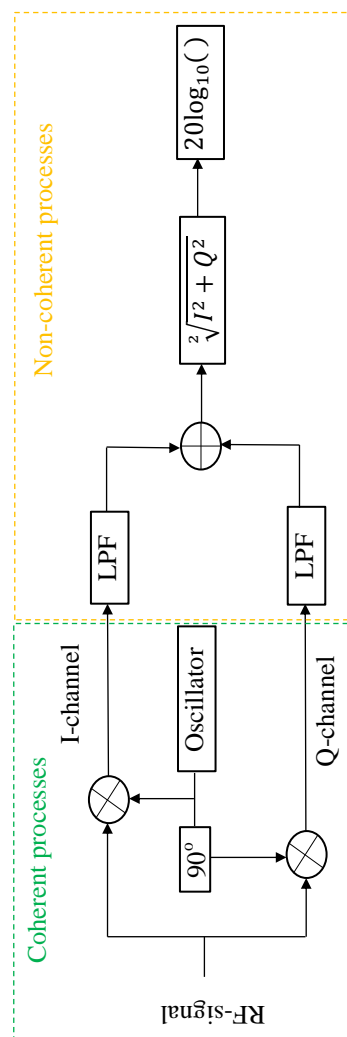


Figure 2. 11 IQ-demodulation and envelope detection.

Figure 2. 12 shows how the ultrasound image is formed using the A-lines that are aligned together based on time of arrival. The data was acquired using Siemens AntaresTM Ultrasound System on imaging a heterogeneous block phantom produced from animal hide, in which image formation illustrates RF-data Figure 2. 12(a), envelope-data Figure 2. 12(b), and envelope with logarithmic compression Figure 2. 12(c). In Figure 2. 12, A-line for each data formation is demonstrated, which is picked-up from the middle of 2D data matrix (highlighted in dashed red vertical line Figure 2. 12). It is clear that soft region (injected by acid to change the regional stiffness) has low amplitude reflection due to weaker interaction between ultrasound wave and low scatterer region. This region is centred at 1000 axial sample and 30 lateral A-line.

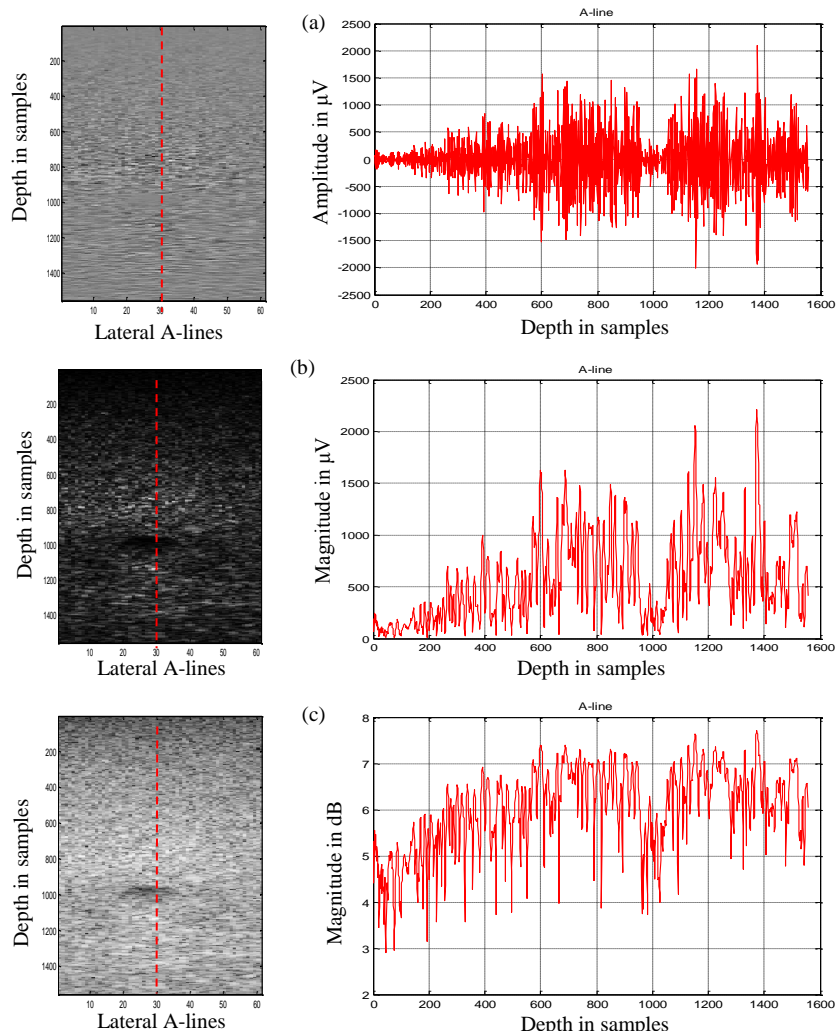


Figure 2. 12 Ultrasound image formation with their corresponding (a) A-lines of RF-data (b) envelope-data (c) and logarithmic compression-data.

2.6 Conclusion

In this chapter, the fundamentals of ultrasound imaging were reviewed by considering imaging system, imaging artefacts, and imaging technology. An overview of ultrasonic transducers, scanning modes, display methods, and resolutions were presented that are relevant to elastography. The effects of elastography artefacts were also discussed in different aspect of sonography, algorithm, and mechanical action. New data access technologies were described along with associated signal representations.

The conclusion behind this background, is to consider an ultrasound imaging system that would be used to acquired RF data of before and after applying compression. The ultrasound system parameters of operating frequency, sampling frequency, and acoustic beamwidth will be considered to provide useful data for processing. The consideration of system parameters can summarized as follows;

Transducer of phased linear array is considered to design such parameters of total elements, operating frequency, active elements, timing of feeding signals, and the weights of signal amplitude. All of these parameters can contribute on providing a useful acquired data for processing.

Resolution is also considered to provide a good enough spatial content elastic map, particularly in axial direction by high enough operating frequency and sampling frequency. The trade of between depth dependent attenuation and spatial resolution is also considered on choosing the operating frequency.

To display the deformation map of displacement and strain is also considered to describe main feature of hard inclusion region by improving the contrast of low strained region of interest.

The acoustic artefacts is also considered to be alleviated before acquisition of the data. The consideration to reducing the acoustic artefacts can summarized by, firm contact between transducer physical surface and the object of interest, firm contact of object surfaces particularly for elastic heterogeneous model, and be sure that the object of interest designed and also manufactured to be acoustic homogeneous.

Chapter 3

Ultrasound Scattering

3.1 Introduction

Ultrasound is a non-invasive modality that has been utilized for many areas of applications, particularly in medical diagnosis [13]. In medical diagnosis, ultrasound systems have been used to visualize inside a human soft tissue in real time for different organs, e.g. kidney, liver, breast and heart, while in advanced systems blood/tissue Doppler imaging and tissue elasticity imaging are also included. In therapy, ultrasound based lithotripsy has been developed for dealing with kidney stones, and as High Intensity Focused Ultrasound (HIFU) for regionally heat and diseased tissue destruction through ablation [55]. Diagnostic ultrasound is a non-invasive, inexpensive, mobility with real time observation capability compared to other approaches [15].

In diagnostic ultrasound physical properties of ultrasound wave scattering are exploited. Generally, there are two categories of wave scattering namely (i) specular scattering and (ii) diffuse scattering. Specular scattering occurs as a result of spatial change in refractive index [56], while diffuse scattering occurs as a result of spatial variation in refractive index. A phenomenon of specular reflection is employed for delineation of organ region of interest as in intensity ultrasound image [57]. On the other hand, diffuse reflection is employed for analysis of Doppler based vector velocity and speckle tracking based elasticity imaging [13, 58].

In cardiology, cardiac function is commonly diagnosed using *echocardiography* that provides a 2D series of images of the heart's cross section [59]. Presently, a new version of 3D echocardiography is now clinically available for 3D visualization of dynamic heart region of interest. Even with 3D visualisation for heart function

monitoring [60], the methods are still mainly limited for global function only. Currently, new research programmes are ongoing that aim to address the need of early diagnose of heart stability disruption that marks a move from global function to regional function assessment of the heart. Accordingly, a potential effort is conducted by developing medical ultrasound imaging techniques which enables a discriminative localization of diseased region in a soft tissue background [61].

Tracking of ultrasound backscatter reflections before and after deformation was developed to determine quantitative measurement methods of tissue deformation. In cardiac assessment a regional fibrosis of heart muscle has low deformation relative to normal regions which can be recognized as a result of tissue stiffness changes according to pathological developments [10]. An interaction between ultrasound wave and tissue scatterers is considered in this chapter by addressing the followings; physical and mathematical fundamentals of ultrasound-body interaction, and scattering theory of pulse-echo ultrasound, fundamentals on tissue similarity measurement.

3.2 Ultrasound Wave Propagation

In physics, wave propagation depends on phenomenal perturbation causing it (e.g. ultrasound wave, electromagnetic wave, etc.) to travels through the media (tissue, blood, water, free space, etc.). The propagation properties (e.g. reflection, scattering, refraction, attenuation, etc.) are common for different modalities. From that, principles of scattering can be considered from different modalities, where Radar scattering theory is the most relevant work field can excerpt from to impose pulse-echo ultrasound [62]. In ultrasound, there are two different approaches to deal with scattering from soft tissue, one considers it as a noise, while the other considers it as predictable component.

A pulse-echo ultrasound propagates into different media such as water (acoustic homogeneous medium), soft tissue (acoustic heterogeneous medium) with a spatially

varying intensity. The wave propagation equations of homogeneous and heterogeneous media are explained in Appendix A.

In normal state, the soft tissue can be considered as stationary medium. On the other hand, propagation of ultrasound wave inside the soft tissue modifies the stationary state in terms of pressure perturbation (p) and density disturbance (ρ). The pressure perturbation and density disturbance causes a local motion that displaces the small elements of the soft tissue [63]. The local motion was employed to track tissue deformation based on acoustic radiation force [64]. In this research, the local motion is ignored, where it is no longer effective due to the external applied compression.

An interesting wave propagation concept is to highlight the coincidences between electromagnetic and acoustic wave propagation, where both of them have the same properties of reflection, refraction, diffraction, etc. Parameters of compressibility and density for acoustic have been analogous to the permittivity and permeability of the electromagnetic wave in terms of their influence over wave propagation equation [67].

3.2.1 Reflections of wave

Acoustic wave can propagate in acoustic homogeneous medium. Changes in acoustic impedance of the medium causes reflection for a fraction of incident energy. The strength of reflected energy depends on the rate of change of acoustic impedance. The latter is defined as a product of medium density and acoustic velocity. Reflections can be categorized based on the rate of change in acoustic impedance as specular reflection and diffused reflection. Specular reflection occurs at a boundary of transition in acoustic impedance, i.e. the transition boundary between heart tissue and blood pool. While diffused reflection occurs when acoustic wave is travelling through medium with spatially varying acoustic impedance and can be developed by system parameter of operating frequency and medium parameter of the scatterer space [68], i.e. reflection from biological organ containing different tissue layers. In ultrasound imaging, specular reflection from boundaries is utilized in segmentation process to calculate the size of the region of interest, such as

left ventricle blood pool. While, diffused reflection is utilized for tissue tracking to estimate the deformation maps.

Figure 3. 1 illustrates the acoustic wave travelling through acoustically homogeneous medium of water in a tank, and how the incident wave travels with no diffuse reflections which is then reflected back at transition boundary of the tank. On the other hand, Figure 3. 2 illustrates the acoustic wave travelling through a block of tissue mimicking material, which is shown how the incident acoustic wave experienced diffuse reflections because medium density changes spatially and also specular reflection at transition surface.

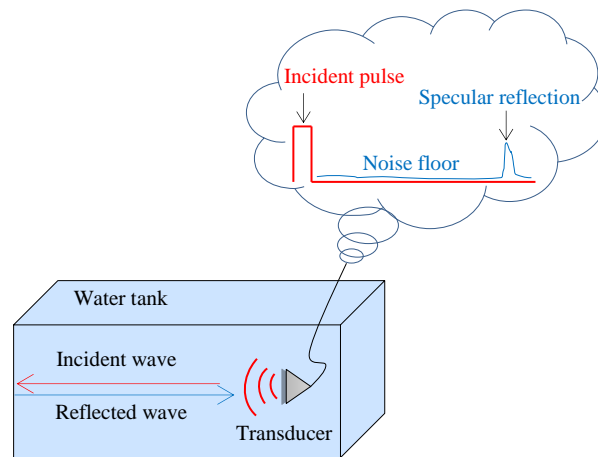


Figure 3. 1 Ultrasound wave experienced through acoustic homogeneous medium.

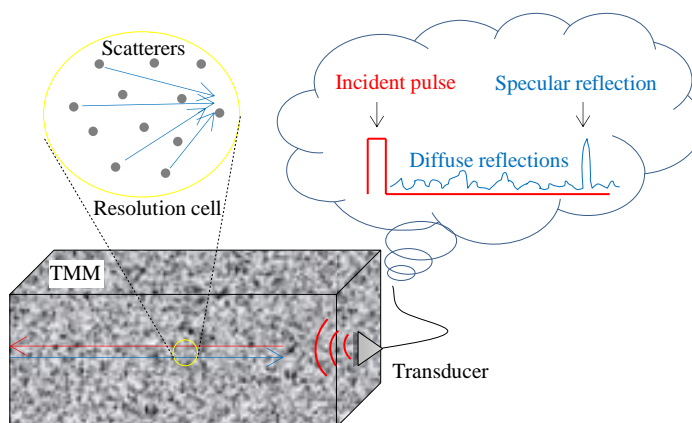


Figure 3. 2 Ultrasound wave travelling through acoustic heterogeneous medium.

3.3 Pulse-Echo Ultrasound Scattering

In ultrasound, scattering phenomena plays a key role in the methods of speckle tracking. Speckle tracking based on the raw data aims to differentiate biological changes in the soft tissue. Understanding the basic physical fundamentals of the scattering theory is necessary to build-up a complete picture for ultrasound simulation and experiment modelling.

Analysis of scattering wave equation is explained in Appendix A and illustrated in Figure 3. 3.

In (3.1), the scatter amplitude $P_s(r, t)$ is a function of scattered wave vector $K = k_s - k_i$ and scattering angle (ψ);

$$P_s(r, t) = \frac{P_0 e^{j(kr - \omega t)}}{4\pi r} k^2 [\beta(K) + \rho(K) \cos(\psi)] \quad (3.1)$$

Where, P_0 is the amplitude of incident wave at radial frequency of ω . ρ is the density, β is the compressibility, k_i is the incident vector, k_s is the scattered vector, and $\cos(\psi) = \frac{k_i \cdot k_s}{|k_i| |k_s|}$.

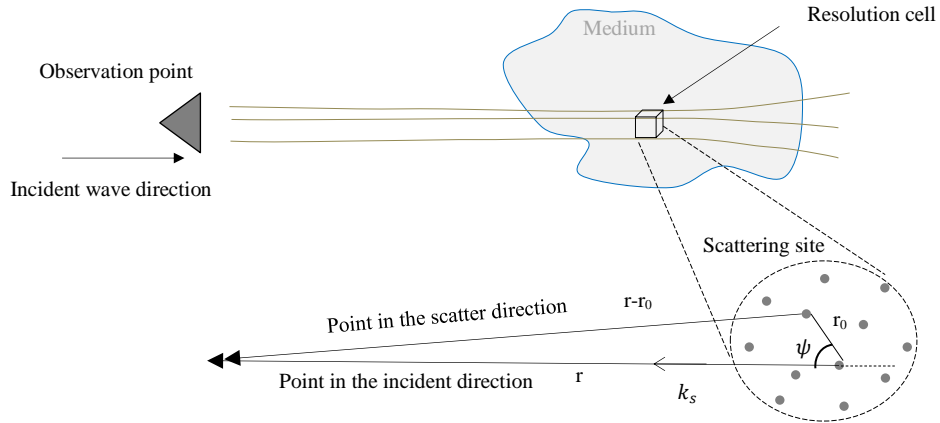


Figure 3. 3 Geometry of wave function far away from scattering center.

In Figure 3. 4, a geometrical representation of incident vector (k_i) and scatter vector (k_s) is shown. In which a coincidence of vector k_i and Cartesian axis of y is convenience to express the geometry of incident and scattered waves in spherical coordinate system. The spherical coordinate angles of elevation θ and azimuth φ are defined. The incident angles θ_i and φ_i are embedded in the scatterer that represents the orientation of k_i relative to the scatterer. The scatter angles θ_s and φ_s verified according to a coincidence in incident vector k_i and the axis of y [65];

$$\cos(\psi) = \sin(\varphi_s) \sin(\theta_s) \quad (3.2)$$

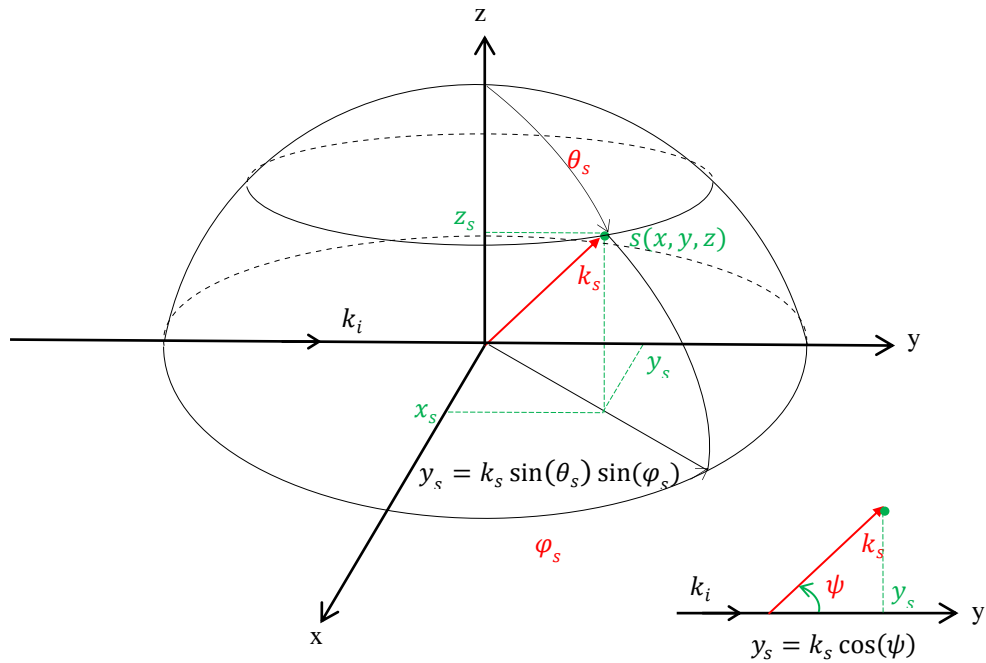


Figure 3. 4 Representation of incident k_i and scatter k_s vectors in spherical coordinates.

Dependency is justified based on amplitude of the scatter parameters, into Rayleigh dependence and angular dependence [69].

- In *Rayleigh dependence*, the scatter amplitude of (3.1) is a function of the square of wave-number (k^2) due to a randomly weak fluctuations of compressibility $|\beta(K)|$ and density $|\rho(K)|$.
- In *angular dependence*, isotropic and dipole scattering are created relative to isotropic spatial fluctuations on compressibility or density respectively.

Generally fluctuations on density are ignored relative to compressibility [69], particularly in medical applications of pulse-echo ultrasound, where a restricted acoustic window of most of the body parts limits the scatter angles by $\varphi_s = \frac{\pi}{2}$ and $\theta_s = \frac{3\pi}{2}$, using (3.2) $\psi = \pi$. Hence, the scatter amplitude of (3.1) represents the difference between compressibility and density fluctuations, $[\beta(K) - \rho(K)]$.

In pulse-echo ultrasound, a received signal of $v(t)$ forming an A-scan is given by the integral of backscattered pressure amplitude of (3.1) over the whole transducer face $S(r)$, [70].

$$v(t) = \int_S P_s(r, t) dS \quad (3.3)$$

3.4 Fundamentals on tissue similarity measurement

Tissue similarity can be measured using cross-correlation of coherent narrow band (RF-echo signal) data in time domain [9, 28], or analytical data in Fourier domain [71-73]. A non-coherent envelope data (B-mode) is also utilized particularly in coarse scale of block based optical flow techniques of using 2D cross-correlation [47, 74], sum absolute difference (SAD) [74, 75] and sum square difference (SSD) [12, 76].

There are two main assumptions for relating the pre-compression and post-compression signals, one assumes that post-compression signal as a time scaled and time shifted replica of the pre-compression signal [77], while the second one assumes only a time scaled replica [78]. Hence to generalize the relationship, a time scaled and time shifted is considered as;

$$r_{pre}(t) = v(t) + n_{pre}(t) \quad (3.4)$$

$$r_{post}(t) = v((1 + \alpha)t + \tau) + n_{post}(t) \quad (3.5)$$

where, r_{pre} and r_{post} are the RF-signals of pre-compression and post-compression states respectively. The echo waveform of v is received by a transducer and contaminated by an independent additive noise of n_{pre} and n_{post} . The received RF-signal after applying compression (r_{post}) comprises τ as a time delay and α as a delay rate.

In this section the theoretical background of similarity measurement methods are considered. Similarity measurement of standard cross-correlation, normalized cross-correlation, sum absolute difference, and sum square difference can be determined by substituting (3.4) and (3.5) into [79];

Standard cross-correlation:

$$R_{SCC}(\tau) = \int_{-\frac{T}{2}}^{\frac{T}{2}} r_{pre}(t) r_{post}(t) dt \quad (3.6)$$

Normalised cross-correlation:

$$R_{NCC}(\tau) = \frac{\int_{-\frac{T}{2}}^{\frac{T}{2}} r_{pre}(t) r_{post}(t) dt}{\sqrt{\int_{-\frac{T}{2}}^{\frac{T}{2}} (r_{pre}(t))^2 dt \int_{-\frac{T}{2}}^{\frac{T}{2}} (r_{post}(t))^2 dt}} \quad (3.7)$$

Sum absolute differences:

$$R_{SAD}(\tau) = \int_{-\frac{T}{2}}^{\frac{T}{2}} |r_{pre}(t) - r_{post}(t)| dt \quad (3.8)$$

Sum squared differences:

$$R_{SSD}(\tau) = \int_{-\frac{T}{2}}^{\frac{T}{2}} (r_{pre}(t) - r_{post}(t))^2 dt \quad (3.9)$$

where T represents window length.

The similarity measurement methods in (3.6-3.9) were originally modelled for jointly stationary signal. So that it produces inaccuracies (jitter errors) and discontinuities in the displacement field [80].

In [79], eight similarity measurement methods were compared relative to Cramér–Rao lower bound (CRLB) to predict the standard deviation of jitter errors. The methods in (3.6-3.9) were recommended in the findings of [79], and particular

recommendation was given to SSD method, where it conducted a lower jitter errors. However, standard cross correlation is the most common tool utilized for delay estimation (displacement), due to its effectiveness in terms of accuracy and capability to measure very small changes [81].

3.4.1 Influence in similarity measurement of strained speckle signals

In practice, biological tissue is an elastic material, which exhibits nearly incompressible property by experiencing a 3D motion of the scatterer in axial, lateral and elevation (out of plane) directions. The nearly incompressible means that when material is compressed in one direction it will expand in other perpendicular directions according to Poisson's law. Poisson's ratio is a measure of incompressibility effect so that it defined as the ratio of fraction of expansion in transverse direction to the fraction of compression in the axial direction, Figure 3. 5;

$$\nu = \frac{\partial \xi_t}{\partial \xi_a} = \frac{\partial \xi_x}{\partial \xi_z} = \frac{\partial \xi_y}{\partial \xi_z} \quad (3.10)$$

where ν is the Poisson's ratio, its value range from 0 to 0.5 for materials classified between totally compressible to totally incompressible [3], $\partial \xi_t$ is a transverse strain, and $\partial \xi_a$ is an axial strain.

For simplicity, a biological soft tissue is considered as homogeneous and isotropic, homogeneous means the material properties are spatially invariant, while isotropic means the mechanical properties are the same in all directions (direction independent). Under these conditions, Hook's law can be given to represent the linear relation between stress (σ) and strain (ξ) as [82];

$$\sigma = E \cdot \xi \quad (3.11)$$

where E is the elastic modulus.

To reduce the effect of the 3D scatterers motion on similarity measurement, a uniform small scale axial compression needs to be applied. Uniform compression can be realized using a wide enough compression surface relative to the object surface and wide enough sonography beamwidth. While gentle freehand compression can also enhance the scatterers motion without a significant change in the scatterer distribution within the sonography resolution.

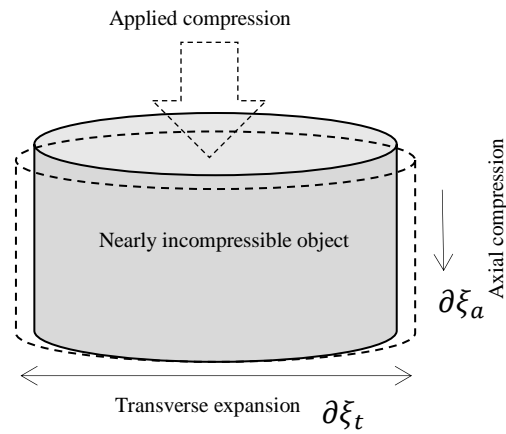


Figure 3. 5 Geometry of nearly incompressible object under axial compression.

3.4.2 Strain estimation techniques

In ultrasound, elasticity imaging (elastography) is represented by strain mapping, strain is measured by two main techniques of direct estimation and gradient based estimation [83, 84]. Direct strain estimation can be categorized into incoherent and coherent estimators, incoherent estimator is based on power spectral density [36, 85, 86] or efficient spectral shift estimation [87] of scattered signals, while coherent estimator is based on iteration of scaling factor for one of the coherent windows in time [88] or Fourier domain [35, 73, 89]. Although, direct strain estimation avoids the need for accurate displacement estimation compared to gradient based strain estimation, it is in an expense of less precise, low strain signal-to-noise ratio at small compression of $\leq 1\%$ [85] and still under development for real time efficiency to cope computational demands [87, 90].

In contrast, gradient based estimation is common for real time processing and is regarded as indirect method due to its mainly dependent on pre-step of displacement estimation. Because of derivative operation of strain estimation (3.12), this dependency subjects to a high frequency noise amplification [30]. The high frequency noise can be regarded as a small fluctuation in displacement estimates (jitter in delay measurements).

Axial strain can be determined by spatial derivative of two sequential displacement measurements in the direction of applied compression [91].

$$\xi_a = \frac{(d_2 - d_1)}{l_o} \quad (3.12)$$

where d_1 and d_2 are sequential measurements in displacement vector, l_o is the length of axial separation distance.

Multi-measurements instead of two sequential measurements were proposed to reduce the variance of strain, which is called *least squares strain estimator* (LSQSE) [30]. An effectiveness of LSQSE on increasing the strain signal-to-noise ratio was

shown to be function of number of displacement measurements. Although, the LSQSE improves the quality of strain mapping, but at the same time reduces strain contrast and the spatial resolution of embedded inclusion. It was shown that an optimal number of displacement estimations depends on the strain high frequency component [30].

A principle of the LSQSE is based on simple linear regression, which uses least square estimator to calculate unknown parameters of gradient (v) and intersection (δ). These two parameters are optimally calculated for each dependent (displacement parameters) and independent (depth parameter) data set of $\{y_i, x_i\}$, $i = 1, 2, \dots, n$ -measurements, as follows;

$$y = \delta + vx \quad (3.13)$$

$$\min_{\delta, v} Q(\delta, v) = \sum_{i=1}^n (y_i - \delta - vx_i)^2 \quad (3.14)$$

In order to minimize the objective quadratic function of Q , optimal values of function parameters are calculated according to the following equations;

$$\hat{v} = \frac{\frac{1}{n} \sum_{i=1}^n x_i y_i - \frac{1}{n} \sum_{i=1}^n x_i \frac{1}{n} \sum_{i=1}^n y_i}{\frac{1}{n} \sum_{i=1}^n x_i^2 - \frac{1}{n} (\sum_{i=1}^n x_i)^2} = \frac{\text{Cov}[x, y]}{\text{Var}[x]} \quad (3.15)$$

$$\hat{\delta} = \bar{y} - \hat{v} \bar{x} \quad (3.16)$$

where in (3.15), Cov and Var are covariance and variance respectively, while in (3.16), an over bar represents the mean value.

In Figure 3. 6, an example of using LSQSE to calculate the strain for four displacement measurements is illustrated. The dots represent displacement

measurements used as inputs to (3.15), to calculate the estimator \hat{v} , and then using (3.16) to calculate estimator $\hat{\delta}$. The straight line represents the linear regression, which is calculated by substitution both optimal estimators of \hat{v} and $\hat{\delta}$ in (3.13).

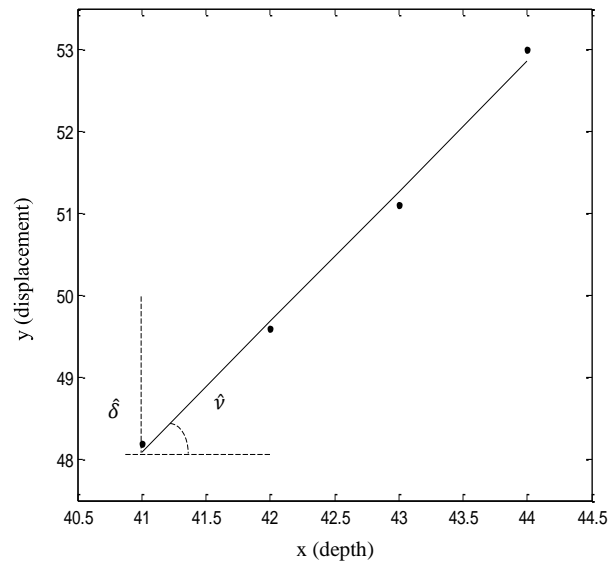


Figure 3. 6 Strain estimation using four displacement measurements.

3.5 Similarity Compensation of Strained Speckle Signals

In signal processing, if two signals are jointly stationary, the delay estimation coincides its actual value, at observation time (correlation window length) reaches infinity. While, if two signals are jointly non-stationary (strained each other), nearly stationary assumption can be considered at finite observation time [92]. In elasticity imaging, the finite observation is function of elastic property of the object of interest, which would be increased when the deformation increases.

Figure 3. 7 shows how the correlation function of strained (pre-compression and post-compression) signals depend on window length. The signals are acquired before and after applying a compression of 3% over a homogeneous TMM. Figure 3. 7(a) shows RF signals of pre-compression and post-compression for window length 7λ . The correspondence correlation function in Figure 3. 7(b) shows a good correlation (correlation coefficient of >0.7), where the peak value is located at actual delay. On the other hand, using longer window length of 25λ Figure 3. 7(c) degrades the correlation function significantly (correlation coefficient of ≤ 0.3) Figure 3. 7(d). The significant loss in correlation gives rise to false peaks (second peak dominance) relative to the actual delay. From that, it can be considered optimal window length is significant for delay measurement of strained signals.

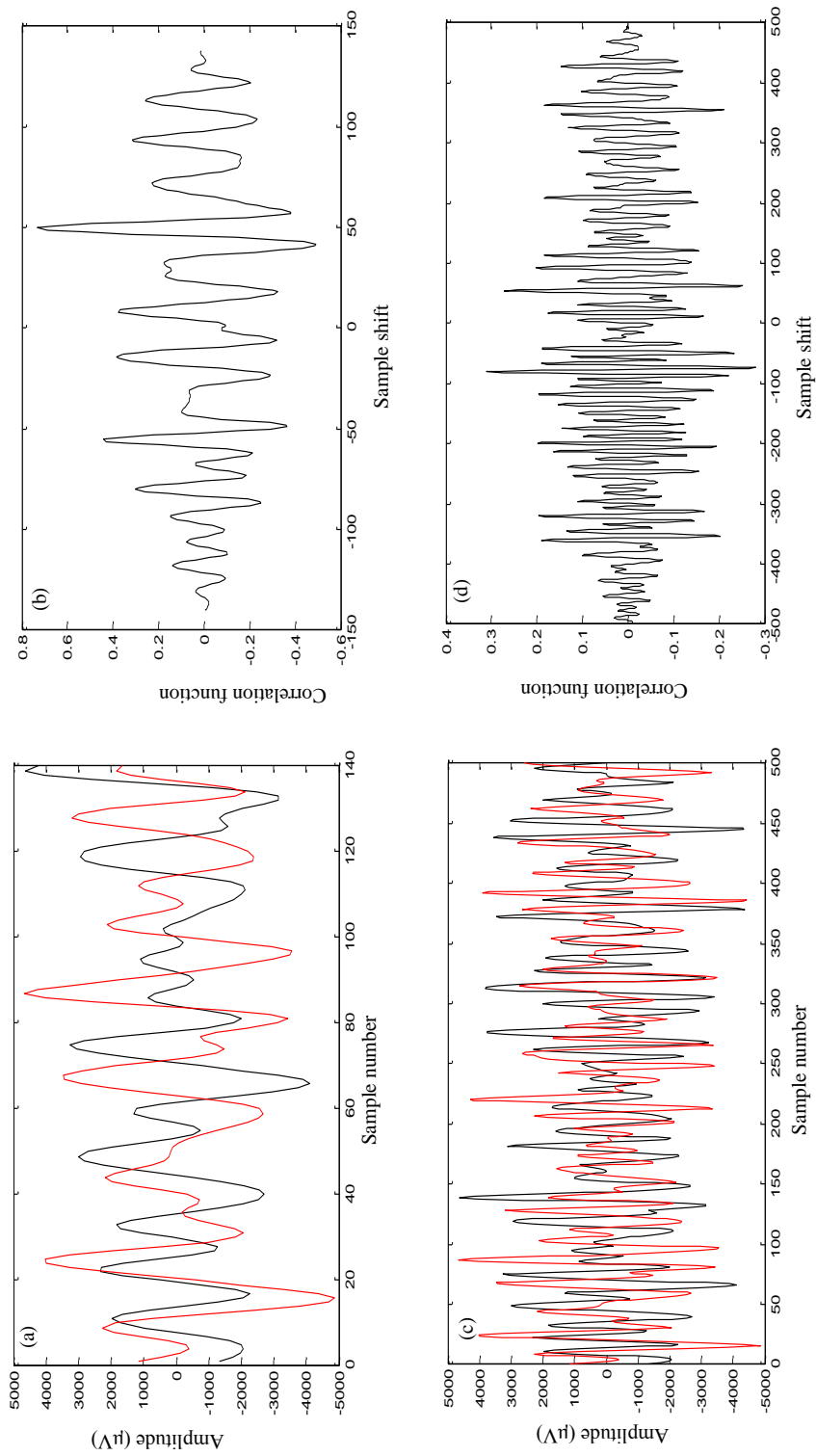


Figure 3. 7 RF signals of pre-compression (black solid line) and post-compression (red solid line) of, (a) window length of 7λ , (b) their corresponding correlation function, (c) window length of 25λ , and (d) their corresponding correlation function.

3.5.1 Axial compensation of strained speckle signals

Cross correlation function is shown to be degraded as a function of applied compression due to echo decorrelation in the axial direction [92], where certain increases in correlation windows length can improve this degradation, at an expense of reduction in measurement spatial resolution. From the early 1990's investigation method was introduced for compensation of correlation loss. A technique of using a small reference (pre-compression) window length in combination with longer comparison (post-compression) window was shown to be improved the correlation [13].

Other investigators [29, 80, 93] use a one dimensional (1D) alignment process that considers correlation windows which are not delayed replicas of each other due to an effect of axial applied compression. A temporal stretching of post-compression window was presented in [80] to deal with compression effect. Appropriate stretching increases the correlation between pre- and post-compression windows, particularly for applied compression of less than 1% [29]. However, temporal stretching is effective for only homogeneous strain mapping [29, 80].

An adaptive stretching method was proposed in [88] uses iterative local stretching for heterogeneous strain field mapping. Adaptive strain estimator in [88] experiences low performance against non-axial scatterer motion because it ignores strain continuity on regularization of estimation outliers, however its performance was improved by involving a regularization concept which is based on a correspondence in neighbours physical property [90]. The iterative process of this estimator is computationally demanding and thus real time elastography imaging is not feasible. In [94], adaptive method of two stretching steps was proposed, in which a global stretching followed by iterative local shift and stretching were performed to reduce the computational demands of adaptive stretching in [88].

Axial applied compression higher than 1% reduces the effectiveness of temporal stretching due to a non-axial (lateral and elevation) motion of the scatterers [88]. A combination of multi-compression averaging and temporal stretching for small compressions was presented in [93] showed to reduce the effect of decorrelation

noise in three dimensions in terms of improvement in a quality of strain map with an increase in strain dynamic range.

3.5.2 Lateral/elevation compensation of strained speckle signals

Compensating the non-axial motion of the scatterers was investigated in [95, 96]. Lateral compensation was involved in addition to temporal stretching, by searching for a best window match of interpolated lateral A-line [40]. Similarly, 2D companding process was suggested in [75], while effectiveness of 2D companding method was investigated for up to 5% axial compression in [97], due to a significant change in scatterers distribution that drastically collapses similarity between 2D windows of pre- and post-compression. A non-proper estimation of companding factor in addition to its action on system PSF particularly at high axial compression was an obstacle against the effectiveness of the 2D companding [98].

Numerical optimization of non-rigid image registration was also suggested to improve the quality of strain map for 2D RF-echo tracking [76, 99], and 3D RF-echo tracking [100]. Although these methods are superior compared to conventional 1D RF-echo tracking of cross-correlation approaches, their significant computational demands is a limiting factor for real time elastography. In coherent direct [90] and also gradient based [101] strain estimation approaches, 2D RF-echo tracking was also considered to improve the strain map. These methods do not outperform 1D tracking that uses lateral expansion (motion) [40, 90, 101, 102], not to mention computational complexity of 2D tracking [90, 101].

In the literature dynamic programming based 2D tracking is employed for real time strain imaging in which an adaptive search region was confined to reduce the computational demands [1, 12, 103, 104]. Further work for real time strain imaging was introduced using 1D tracking in Fourier domain [105] in which a high frame rate imaging was considered to reduce the decorrelation noise for displacement estimation [89].

Although the axial and also lateral compensations of scatterer motion were effectively utilized for 1D and also 2D tracking to produce qualitative strain map. Scatterers are also moved in elevation direction, using recorded narrow band data alone that describes in-plane motion only are not enough for certain range of compression over non-isotropic tissue structure.

3.5.3 Multi-step processing

A multi-step process is also considered to improve the estimation resolution using coherent narrow band data [75, 106] or combination of non-coherent (envelop echo signal) data for coarse scale and coherent (narrow band echo signal) data for fine scale [47, 107]. The estimated lags represent regional displacement map, in which the strain is estimated as displacement gradient for each sequential two points [9] or multi-points [30], the later was commonly used to provide qualitative strain field by reducing an amplification of roughness in displacement steep with an expense of strain resolution [30, 108].

3.6 Conclusion

In this chapter, the fundamentals of scattering wave theory were reviewed wherein some of key parameters that effect scatter wave strength were identified. Acoustic homogeneous and heterogeneous media were considered, water and clear glass represent acoustic homogeneous, while tissue mimicking material (TMM) and body organs represent acoustic heterogeneous media. Finally, raw signal of A-scan were represented by an integral of backscatter at the face of transducer receiver. Similarity measurement methods were presented, and how it influenced as a result of compression effect. Methods of similarity compensation were reviewed. In next chapter, a novel simulation algorithm for dynamic representation of scatterer motion will be presented. The simulation model will be able to provide RF data of pre-compression and post compression, which can be processed to estimate the displacement and strain fields. Speckle tracking algorithm will also be introduced,

which will be shown how effectively estimates displacement and strain fields for small scale applied compression of 0.2%.

Chapter 4

Dynamic Ultrasound Scatterer Simulation Model

4.1 Introduction

The ultrasound imaging system was introduced in Section 2.2, where scanning methods were described in Section 2.2.1. Simulation of ultrasound imaging was reviewed in Section 2.3. The objective of this chapter is to construct a novel simulation framework for a scenario of ultrasonic imaging of biological homogeneous and heterogeneous soft tissue before and after applied compression. The simulation framework will be able to provide RF data of pre-compression and post-compression that can be used for speckle tracking. The proposed method of simulation framework combines both FEM and Field-II programs to provide RF data of pre-compression and post compression. The performance evaluation of the simulation framework is conducted by using speckle tracking algorithm to estimate displacement and strain mapping. Both of displacement and strain are compared favourably with FEM numerical solution.

Pre-compression and post-compression signals are regarded as partially correlated, which are connected in a varying delay [109, 110]. This varying delay leads to inaccuracies and discontinuities in the displacement field [111, 112], which is in turns amplified by gradient operation of strain estimation [30]. The variance of the displacement field in the direction of applied compression is a function of the wavelength, physical characteristics of the object, and the compressing scenario, [3, 28]. So that, in the speckle tracking algorithm correlation window length is optimized for good spatial resolution and lower inaccuracy and discontinuity. The

displacement field is smoothed by moving average window that maximizes the SNR of the displacement field.

The remainder of this chapter is organized as follows; Section 4.2 describes the methodology of simulation framework, and how both of Field II and FEM programmes are combined. Section 4.3 explains the Field II model of scanning scenario and soft tissue object, while section 4.4 explains FEM model of object mechanical characteristics and the axially applied compression. Section 4.5 includes the proposed algorithm of composition between scatterers of Field II model and the nodes of FEM model. Section 4.6 presents the processing of RF data that has been already provided by the simulation framework. The processing includes the displacement estimation and its smoothing process in addition to strain estimation. Results are illustrated and the discussion are presented in section 4.7.

4.2 Methodology

The proposed model of using Field-II program for ultrasonic acquisition to form pre-compression (reference) raw-data and post-compression raw-data (comparison) raw-data is designed [113]. The design model is introduced to represent both of homogeneous and heterogeneous (with hard inclusion) tissue before and after applied compression. In Figure 4. 1, a block diagram of proposed methodology is shown. The Field-II model uses a pre- compression scatterer model to form the reference raw-data, and a post-compression scatterer model to form comparison raw-data. The scatterer positions are moved in pre- compression scatterer model according to the FEM (ANSYS-11) model to create the post- compression scatterer model using our proposed scatterer-nodes composition algorithm. The composition algorithm is designed to associate each scatterer position in the Cartesian space coordinate with the closest four nodes of FEM model based on distance, and then moving it according to weighted displacement information of the FEM model. In the FEM model, the displacement information is created as a result of compression model (applied compression and degree of freedom). Finally, axial displacement field is estimated using speckle tracking technique of 1D cross-

correlation for raw simulation data of pre- compression and post-compression, while a gradient of displacement vector is used to form a strain field as illustrated in Figure 4. 1.

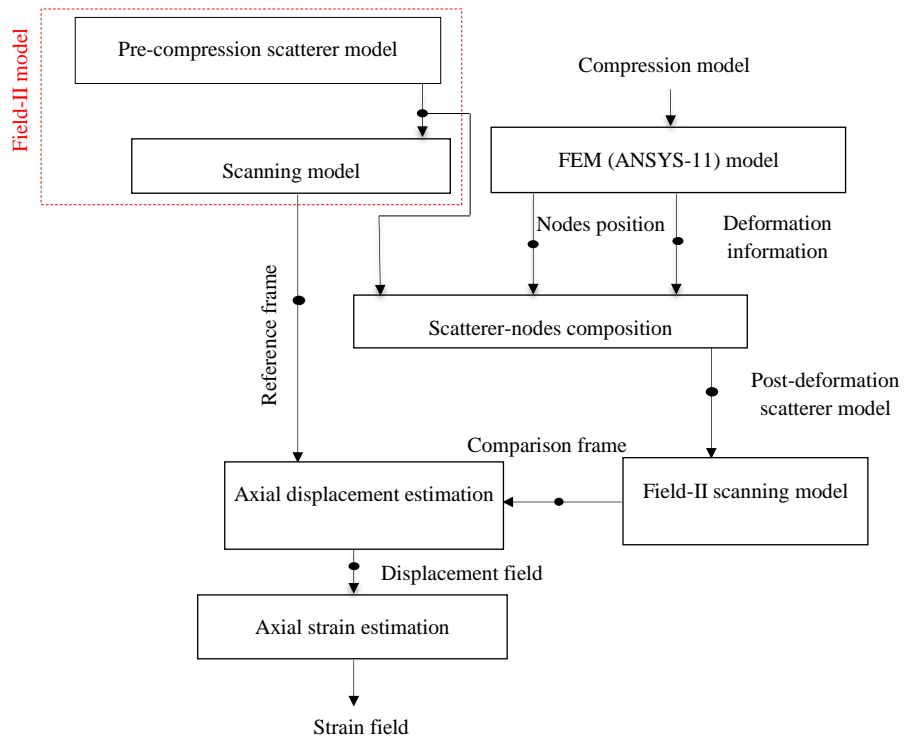


Figure 4. 1 Block diagram of the proposed methodology.

4.3 Field-II Simulation Model

Simulation model of Field-II is constructed by four sub-models of transducer, scatterer object, scanning, and data format. Each model of the four is designed to verify experiment model that would be explained in a next chapter.

In general, Field-II model would be performed in two phases to create pre and post-compression frames. In the first Phase, the model runs to formulate the pre-compression frame by involving the scatterer object pre-positions. In the second phase, the model runs to formulate the post-compression frame after moving the scatterer positions according to FEM deformation information. However, models of the transducer, scanning, and data format retain the same parameters within both Phases of Field-II running.

This situation performs analogues to experiment set-up scenario of using DYNARAY ultrasonic Phased Array Controller and XYZ scanner.

4.3.1 Transducer model

Field-II program provides several models for transducer such as, concave aperture, 1D linear array, 2D array, and convex array. In this work, a linear phased array is modelled for emitting and reception according to the main block diagram of Figure 4. 2. The model parameters comprise 128 elements, 64 active elements, 5 sub-division of each element in y-direction (element structure), 5MHz operating frequency, 50 MHz sampling frequency, 0.3 mm pitch, and 50 mm focal depth were conducted.

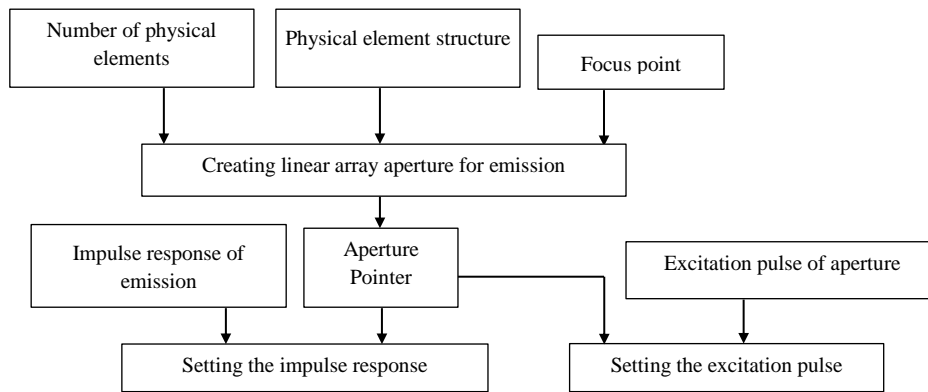


Figure 4. 2 Main flowchart of linear array transducer modelling.

Linear scanning is performed by activation of 16 elements for a focus point of 50mm. Figure 4. 3(a) shows 16 elements transducer aperture of sub-division of each element in y-direction, while Figure 4. 3(b) shows 16 elements transducer pulse echo field focusing at 50mm depth with 1mm beamwidth (-3dB).

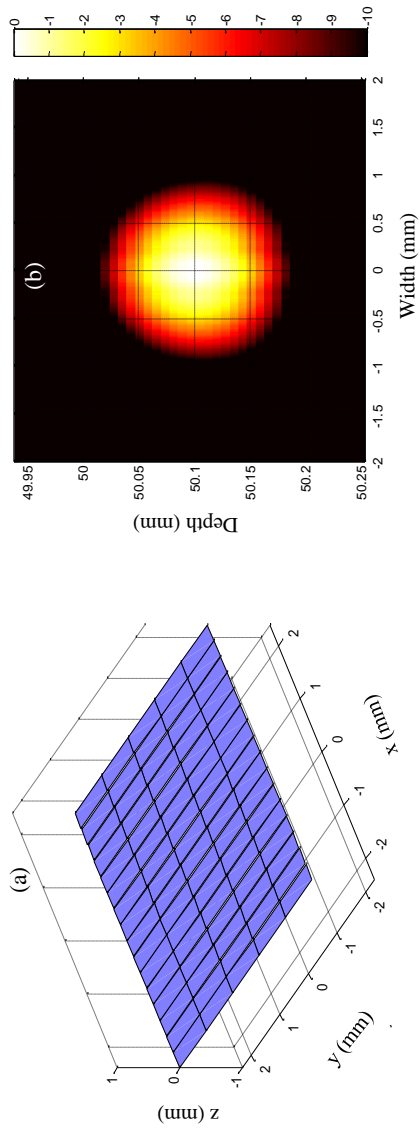


Figure 4. 3 (a) Linear phased array transducer aperture and (b).pulse echo field.

4.3.2 Simulation model of biological tissue

A 3D object is modelled for a cuboid dimension of $L \times B \times H$ where $L=50\text{mm}$ is the length, $B=10\text{mm}$ is the breath, and $H=50\text{mm}$ is the height. 100000 scatterers are located in uniform distribution, while their amplitudes are normally distributed to attain a fully developed speckle [68]. We assume that the scatterer density and regularity are the same for background and inclusion regions. Figure 4. 4 shows a 100 scatterers' positions in Cartesian coordinate. Reflected signals from reference scatterers' position are acquired to form row-data that represents pre-compression frame. For post-compression frame, scatterers' reference positions are going to be moved according to FEM model of compression. This will be demonstrated in later sections of this chapter.

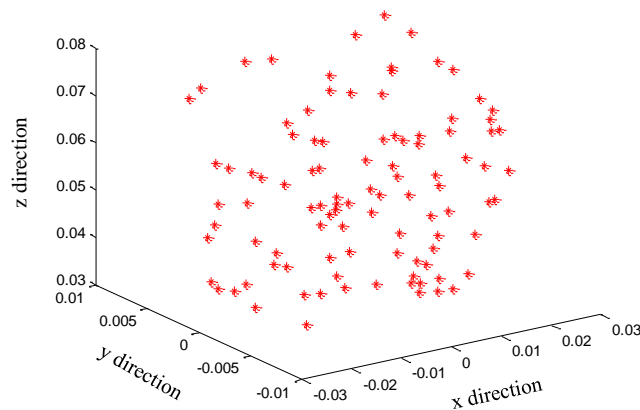


Figure 4. 4 Randomly distributed scatterers position in 3D object.

4.3.3 Linear phased array scanning model

In this scanning model, dynamic focusing is performed by sequential activation of the elements along the array. Main steps of scanning model are shown in Figure 4. 5 and can be explained as follows;

Lines setting for a number of A-lines that represent frame lateral lines. This is equal to the number of total elements - number of active elements + 1.

Setting of focusing centre point is the program step to identify a start point of dynamic focusing that would be considered as a reference point on calculating the focusing delay times.

Creating an aperture focus time is a step toward inserting the focus of transducer aperture.

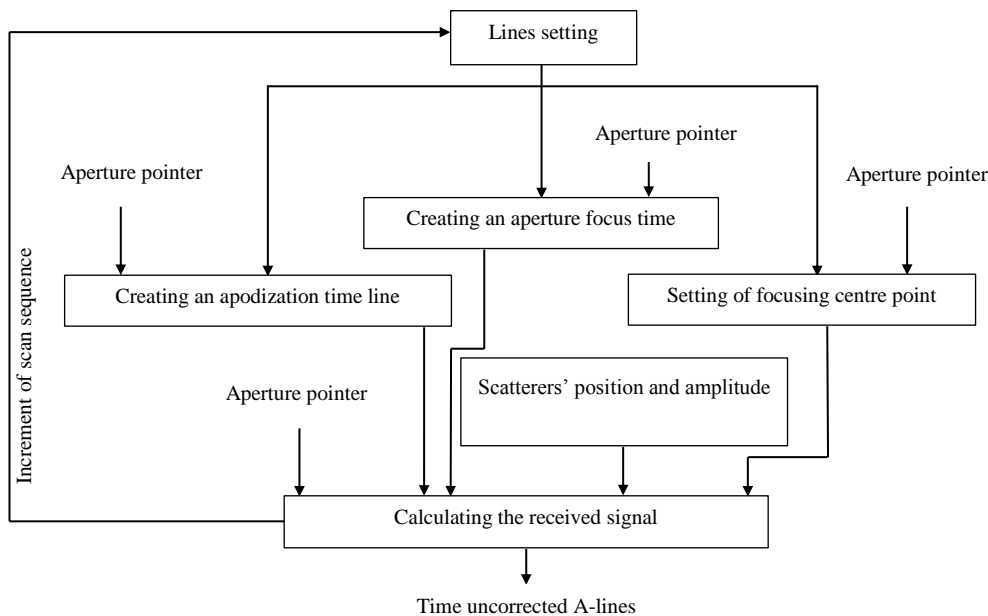


Figure 4. 5 Flowchart of linear phased array scan model.

Creating an apodization time line is a changing in intensity profile of the active elements of transducer aperture, such as Rectangular, Hann, and Cosine-tapered as shown in Figure 4. 6(a, b, c) respectively.

Scatterers' position and amplitude are information that has been created on performing the object under imaging, see section (4.3.2). The scatterers' positions are going to be moved according to displacement information of FEM model to create the post-compression raw data.

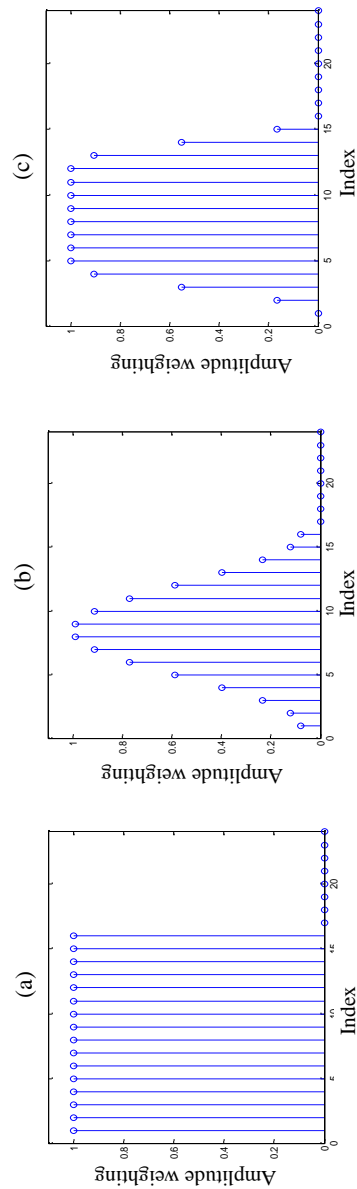


Figure 4. 6 Apodization methods of (a) Rectangular, (b) Hann, and (c) Cosine-tapered.

Calculating the received signal is the program step that performs a spatial convolution of transmitted signal for each step of scanning with a collection of scatterers.

The procedure is repeated sequentially for each step of the scanning over the object region of interest. Figure 4. 7(a) shows RF A-line from single step of scanning model. For processing purposes, the frame of raw-data needs a time correction.

4.3.4 Raw data simulation model

In this model a time correction procedure is considered, which aligns the received backscattered signals in terms of time correction. The time correction process is significant to proceed toward further processing, such as speckle tracking, image processing and image analysis. The time correction model is illustrated in Figure 4. 8 in which, a minimum start time of dynamic focusing is determined, then the start time of each A-line is compared with the determined minimum start time to be shifted then for a purpose of alignment. The procedure is repeated sequentially for whole received A-lines of linear scanning. A candidate time uncorrected RF-data and time corrected RF-data are illustrated in Figure 4. 7(b and c). Figure 4. 7(b) shows how some of time uncorrected A-lines are aligned using time correction process, Figure 4. 7(c). To proceed for image processing and image analysis RF-data can be converted to the analytic data using the Hilbert transform. The Hilbert transform is a linear operation that extends the real data sequence into complex plane. B-mode image of envelope-data and Log-data can also be performed, Figure 4. 9 shows the envelope A-line, envelope raw-data, logarithmic compression A-line, and logarithmic compression raw-data from (a-d) respectively.

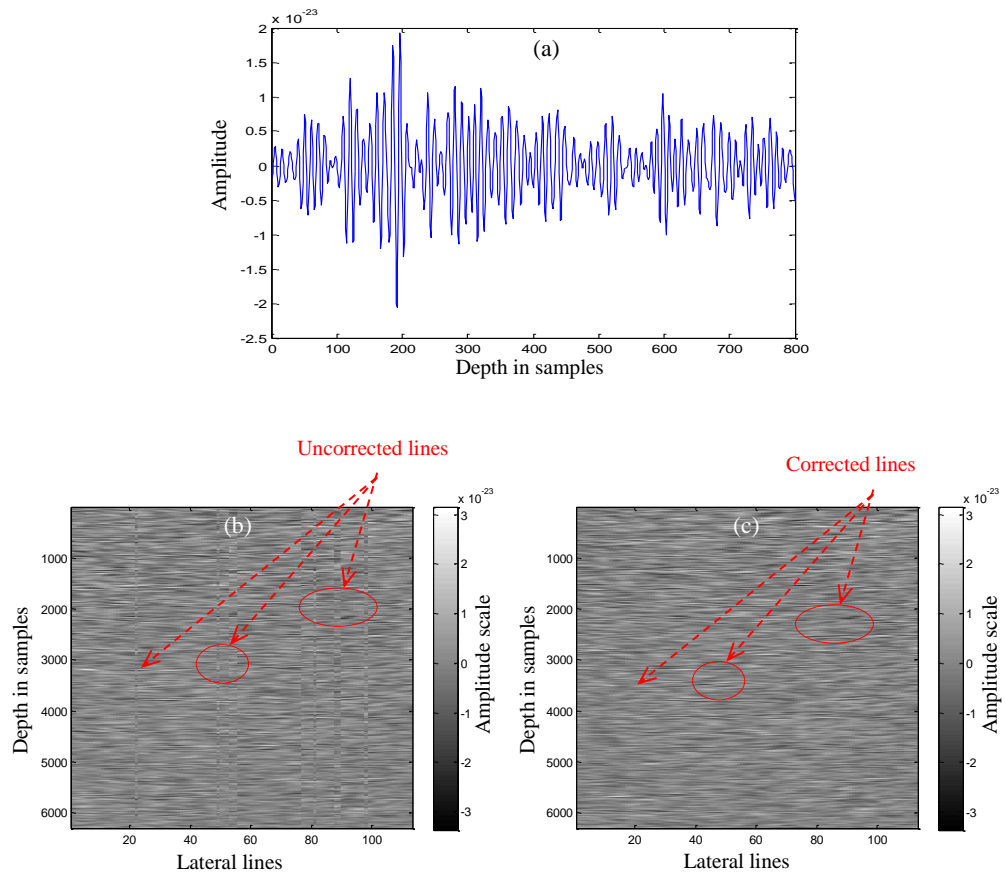


Figure 4.7 Linear phased array scan model of 128 transducer elements and 16 active elements, (a) single RF A-line, (b) image of RF-data with time uncorrected, and (c) image of RF-data with time corrected.

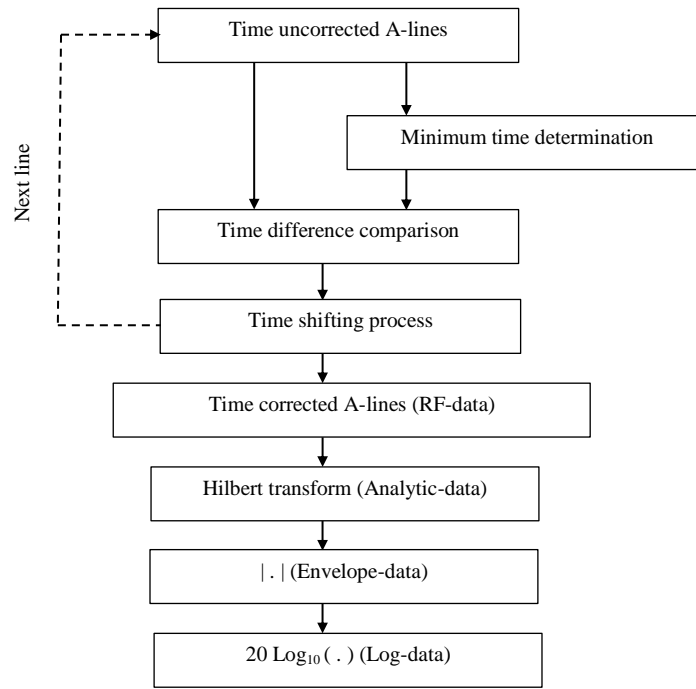


Figure 4. 8 Flowchart of raw data simulation model.

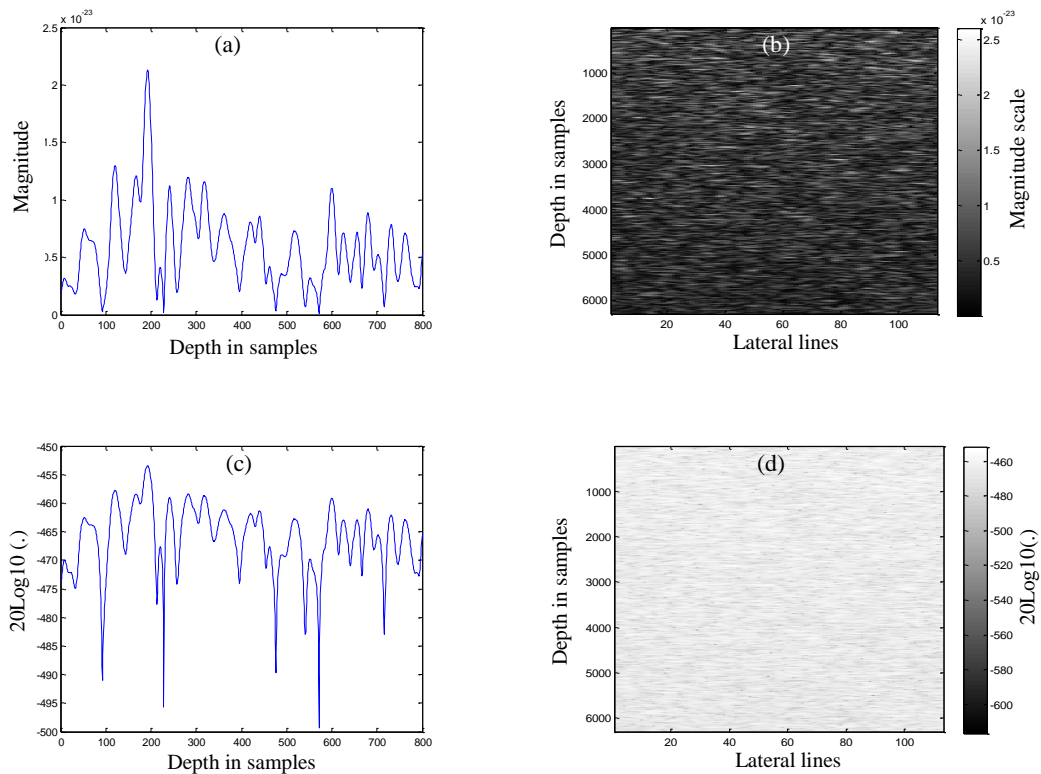


Figure 4. 9 (a) Linear phased array scan model of 128 transducer elements and 16 active elements, envelope raw A-line, (b) image of envelope raw-data , (c) Log envelope A-line, and (d) image of Log envelope -data.

4.4 FEM Simulation Model

In this section, a simulation model of a dynamic object will be developed in terms of two sub-models namely biological tissue model and mechanical compression model. The FEM model is a golden standard program of mechanical representation for project design. In this work, initial understanding of tissue responses to the compression is accomplished using ANSYS-11 program. This program analyses the input parameters by providing the three-dimensional displacement and strain fields that can be used as a reference standard to the proposed methodology based on speckle (RF-data) tracking.

4.4.1 Simulation model of biological tissue

Biological tissues are regarded as homogeneous, isotropic and nearly incompressible material (Poisson's ratio~0.5) [96], properties of this material is introduced in section 3.4.1. FEM program is used to simulate this material for an object under axial compression.

Figure 4. 10 (a) is in the same cuboid dimension and space location of Field-II model that has been given in section 4.3.2, this object has been uniformly compressed in axial direction by 0.2% (0.1mm) of its dimension (H=50mm). The object is deformed axially as well as in the transverse directions. It is clear that low deformation at a bottom of the object, due to a zero degree of freedom at the base. In addition, Figure 4. 10(b) shows a 3D mapping of the displacement vectors that illustrates the nearly incompressible effect.

The body organs composes of different types of tissue layers, such as breast which contains of adipose and glandular as a two dominant tissues. However as mentioned in section 3.4.1, for simplicity the simulation model of biological tissue is considered as homogeneous and isotropic.

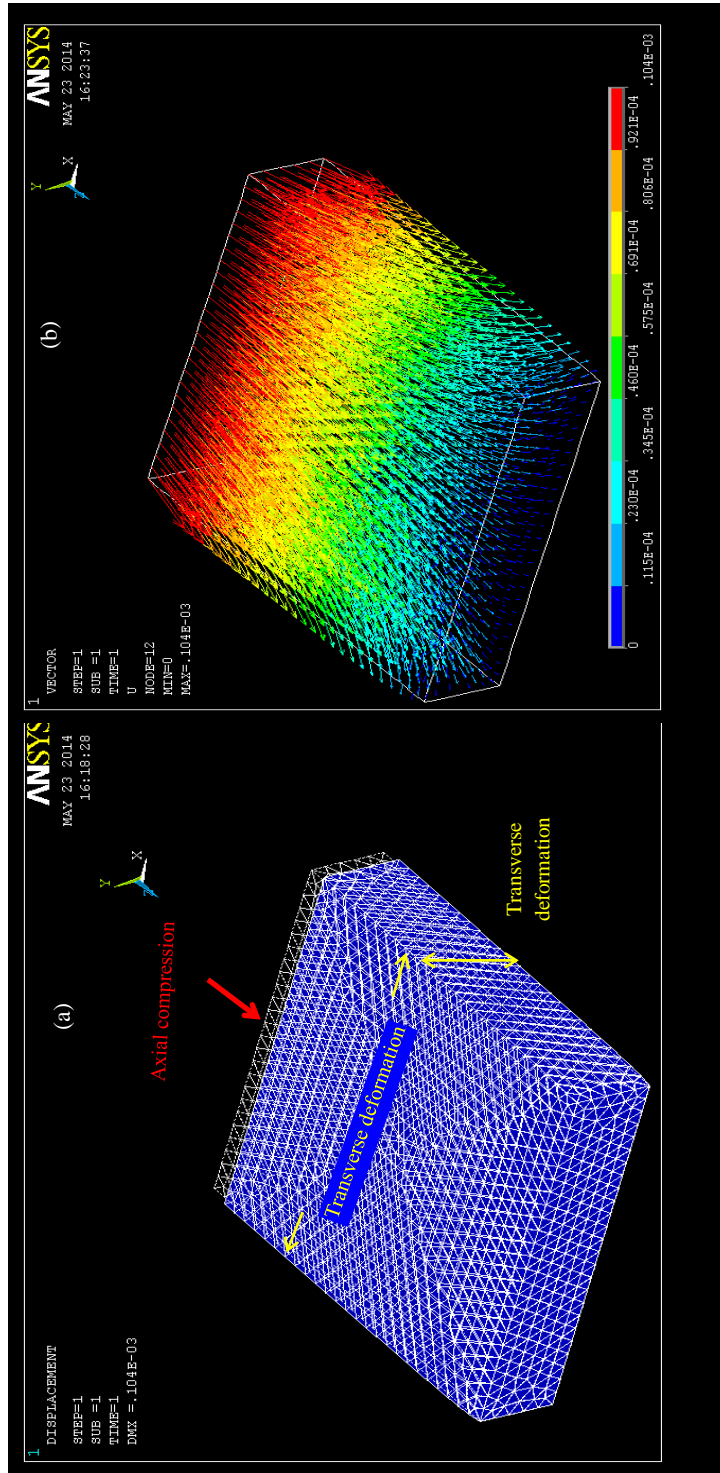


Figure 4. 10 (a) FEM simulation of nearly incompressible model, meshes responding before and after axial uniform compression, and (b) 3D mapping of displacement vectors.

Hence, ANSYS-11 software is employed to form homogeneous and heterogeneous tissues as linearly elastic medium. For homogeneous model, a Young's modulus of 20kPa and Poisson's ratio of 0.495 is used [113] as an isotropic nearly incompressible material with a tetrahedral meshing of 35000 nodes. While for heterogeneous model, a hard inclusion is included at the centre of background. Two different inclusions are considered to investigate the strain distribution, one with cubic shape of 10mm side length Figure 4. 11(a), while the other with cylindrical shape of 15mm diameter and 10mm length Figure 4. 11 (b). The inclusions are imbedded in the background using "add" option of ANSYS-11 program. The inclusion bar laid in horizontal position relative to the applied compression as shown in Figure 4. 11.

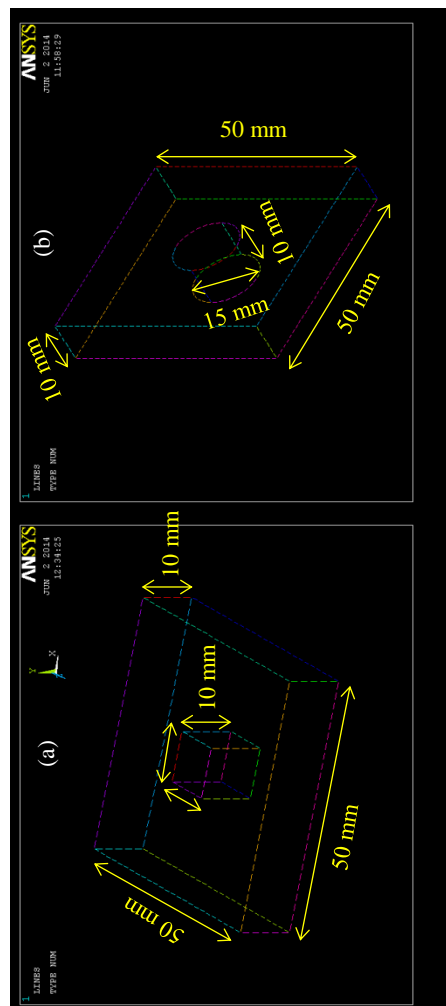


Figure 4. 11 3D simulation of heterogeneous FEM model, (a) cube inclusion, and (b) cylinder inclusion.

4.4.2 Mechanical compression model

Assuming a uniform compression is applied to the (L x B) surface of the background of cuboid described in section 4.3.2 with the base free to move in the (x , y) plane only results in a displacement of H_d mm in the z direction and an ideal strain field of;

$$\xi = \frac{H_d}{H} \quad (4.1)$$

where, H is height of the object.

An upper surface of the background is loaded axially, Figure 4. 10 (a), using displacement on area option of ANSYS-11 analysis process for different values 0.1mm (0.2%) and 0.5mm (1%).

4.5 Composition Model of Field-II and FEM

The main input parameters of the composition algorithm are imported from Field-II and ANSYS-11 simulation models, as illustrated in Figure 4. 12. Field-II provides the scatterers' space location in the pre-deformation state of the 3D object (x_s^r, y_s^r, z_s^r) , while ANSYS-11 exports the nodes space location $(x_{N_n}, y_{N_n}, z_{N_n})$ and displacement information $(disp_n^x, disp_n^y, disp_n^z)$, $n = 1,2,3,4$. The least distant four nodes from each scatterer are localized and defined as a displacement unit represented by tetrahedral structure as shown in Figure 4. 13, where N_n , S , and d_n , represents node, scatterer, and distance respectively.

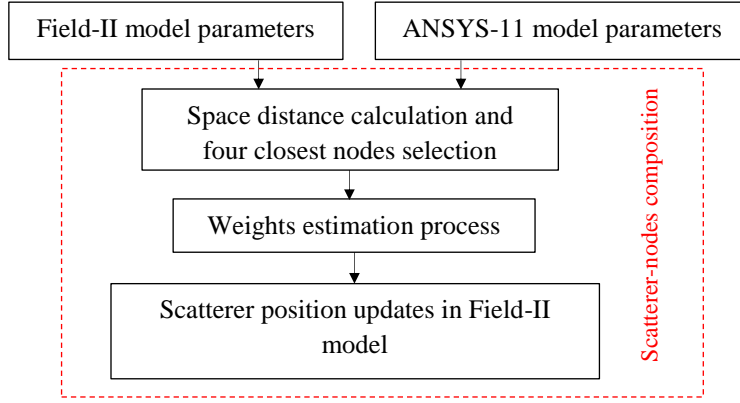


Figure 4. 12 Scatterer-nodes composition algorithm flowchart.

In Figure 4. 13, the displacement information of the nodes are weighted and added to the scatterer space location S . As a consequence, all scatterers will be displaced to represent the 3D object of post-deformation state (x_s^c, y_s^c, z_s^c) in Field-II model, as follows:

$$x_s^c = x_s^r + \sum_{n=1}^4 W_n^a \cdot \text{disp}_n^x \quad (4.2)$$

$$y_s^c = y_s^r + \sum_{n=1}^4 W_n^a \cdot \text{disp}_n^y \quad (4.3)$$

$$z_s^c = z_s^r + \sum_{n=1}^4 W_n^a \cdot \text{disp}_n^z \quad (4.4)$$

where

$$\sum_{n=1}^{n=4} W_n^a = 1 \quad (4.5)$$

and W_n^a is n-th weight.

In the scatterer nodes composition block shown in Figure 4. 12, an actual weight (W_n^a) of each node is estimated based on a distance ratio which is described as follows:

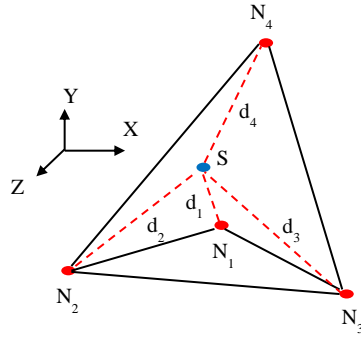


Figure 4. 13 Tetrahedral structure unit.

Firstly, in the Cartesian space, the distance d_n from each node $(x_{N_n}, y_{N_n}, z_{N_n})$ to a certain scatterer (x_s^r, y_s^r, z_s^r) is calculated as:

$$d_n = \sqrt{(x_s^r - x_{N_n})^2 + (y_s^r - y_{N_n})^2 + (z_s^r - z_{N_n})^2} \quad (4.6)$$

The distances are sorted and four closest nodes are selected as input parameters to the weight estimation process as:

$$d_1 < d_2 < d_3 < d_4 \quad (4.7)$$

Secondly, an iterative estimation of the actual weights is performed. For this an initial distance state is assumed as

$$d_1^0 = d_2^0 = d_3^0 = d_4^0 \quad (4.8)$$

producing the following initial estimation of weights

$$W_n^0 = \left(\frac{1}{\text{no.of nodes}} \right) = 0.25, \quad n = 1, 2, 3, \text{ and } 4 \quad (4.9)$$

In the first iteration, d_4 is considered as the most distant node.

$$d_1^0 = d_2^0 = d_3^0 < d_4 \quad (4.10)$$

and the actual weight of node four is computed using a distance ratio as

$$W_4^a = \frac{d_1}{d_4} \cdot W_4^0 \quad (4.11)$$

The difference in weight of W_4^a and W_4^0 will be shared equally to the weights of other equidistant nodes (1, 2, and 3).

$$W_n^1 = W_n^0 + \left(\frac{W_4^0 - W_4^a}{3} \right) > W_n^0, \quad n = 1, 2, \text{ and } 3 \quad (4.12)$$

In the second iteration, d_3 is considered as the second furthest node from the scatterer

$$d_1^0 = d_2^0 < d_3 < d_4 \quad (4.13)$$

The actual weight of third node is estimated as:

$$W_3^a = \frac{d_1}{d_3} \cdot W_3^1 \quad (4.14)$$

The difference in actual and iterative weights is divided equally and added to the weights of both first and second nodes as follows:

$$W_n^2 = W_n^1 + \left(\frac{W_3^1 - W_3^a}{2}\right) > W_n^1, \quad n = 1 \text{ and } 2 \quad (4.15)$$

In the third iteration step, d_2 is considered as the third furthest node from the scatterer

$$d_1^0 < d_2 < d_3 < d_4 \quad (4.16)$$

and the actual weights of both first and second nodes are

$$W_2^a = \frac{d_1}{d_2} \cdot W_2^2 \quad (4.17)$$

$$W_1^a = W_1^2 + (W_2^2 - W_2^a) \quad (4.18)$$

By combining (4.11), (4.14), (4.17) and (4.18) it can be shown that the summation of actual weights is unity as required from (4.5).

4.6 Axial Displacement/Strain Fields Estimation

A block diagram of the axial displacement and strain field estimation algorithm is shown in Figure 4. 14. The deformation of the object under compression is obtained by estimation of displacement and strain in the direction of applied compression. Each A-line in the frame is segmented based on an optimum window that is considered for a range of window lengths as a function of signal-to-noise ratio for a region of interest within the smoothed displacement field. The speckle tracking

approach uses standard cross-correlation between the segmented pre-compression and post-compression windows. A continuous displacement field is assumed and low lateral decorrelation noise is expected due to a small applied compression of 0.1mm (0.2% of object height) is applied using FEM model, while decorrelation noise expected to be developed when compression of $\geq 0.5\text{mm}$ (1% of object height) will be applied. A spline interpolation is employed for subsample displacement estimation of the correlation peak locations [25]. Sequential windows are overlapped by 50% to form less noisy strain estimates [91].

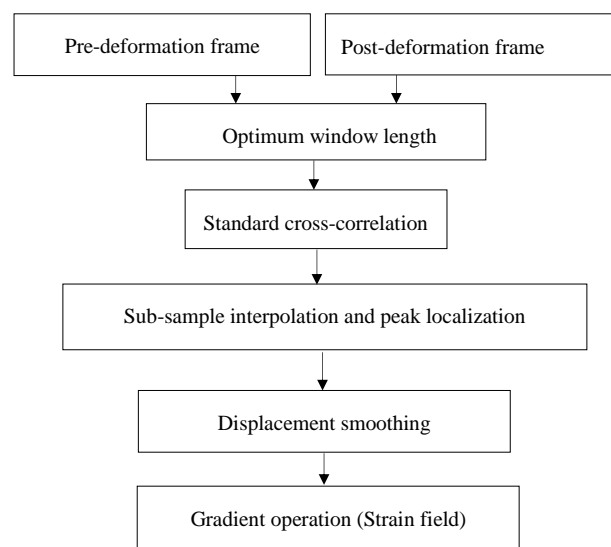


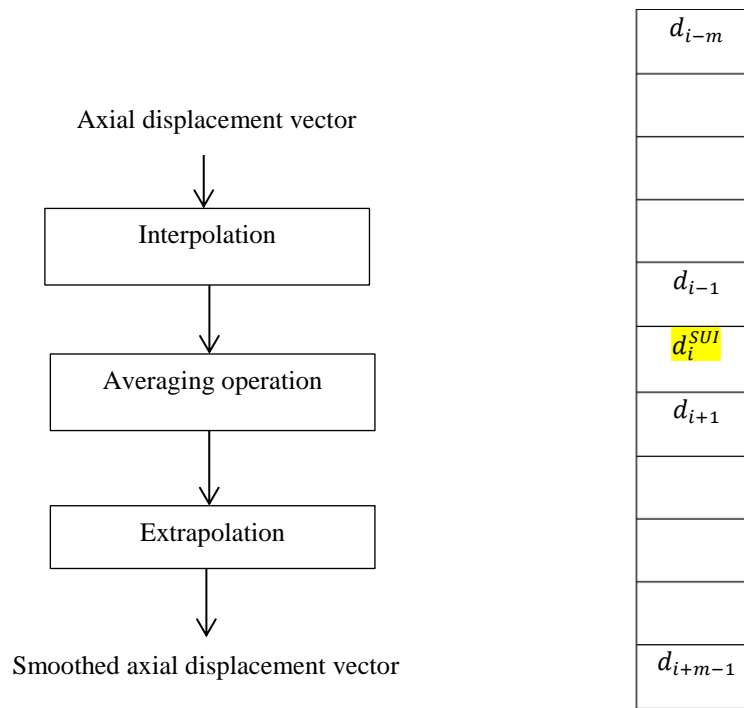
Figure 4. 14 Block diagram of axial displacement and strain estimation.

The variance of estimated displacement is reduced by a smoothing process that is performed in the direction of displacement gradient, using averaging operation as a pre-processing toward noise reduction in strain estimation. The smoothing process of Figure 4. 15(a) is performed for each interpolated axial displacement vector, each vector is linearly interpolated first to increase the number of segments of averaging set, which would reduce fluctuation in average value and at the same time retain displacement spatial resolution. The averaging operation (4.19) considers a *segment*

under interest (SUI) as a middle segment of interpolated set Figure 4. 15(b) that will be exchanged accordingly by the average value.

$$d_i^{SUI} = \frac{1}{M} \sum_{w=i-m}^{w=i+m-1} d_w \quad (4.19)$$

where d_i^{SUI} is the displacement of segment under interest that will be exchanged by average value, d_w is the displacement window set of averaging operation, and M is the length of displacement window set ($M = 2m + 1$), m represents the number of displacement segments in each side of d_i^{SUI} . After applying the averaging operation over a complete vector of interpolation, linear extrapolation performed to retain vector original length Figure 4. 15(a).



(a) Smoothing process

(b) Window set of averaging

Figure 4. 15 (a) Proposed method of smoothing process and (b) displacement window set of averaging operation.

4.7 Results and Discussion

In this section the proposed algorithm will be investigated for three different situations of, small scale compression of 0.2% over homogeneous and heterogenous objects, small correlation window length, and compression of 1% over heterogeneous object. Result of each situation will be discussed.

4.7.1 Small scale applied compression

As described in section 4.4.2, axial compression of 0.1mm is applied to upper surface of a cuboid homogeneous object. Using the simulation parameters described in sections 4.2 - 4.5, pre-compression and post-compression frames are generated. These two frames are then considered as an input data to the algorithm described in section 4.6, to produce a non-interpolated axial displacement field Figure 4. 16(a). The ideal field obtained from FEM is shown in Figure 4. 16(b), which is consistent with the estimated one in Figure 4. 16(a). Figure 4. 16(a) shows the displacement of 0.092mm, while in Figure 4. 16(b) it is measured as 0.1mm resulting in an error in displacement estimation of 8 μm . This error of 8% is accounted by a combination of algorithmic error, randomness of scatterer locations, and meshing structure of FEM object. A 3.5λ correlation window length and 50% window overlap are used.

A Spline interpolation is used for subsample peak location of cross-correlation to provide subsample displacement in terms of gradient differentiation, as shown in Figure 4. 16(c). However, fluctuation in displacement exists due to axial decorrelation (drift in peak location) Figure 4. 16(c). Figure 4. 16(d) shows the displacement field that has been smoothed using the proposed method of Figure 4. 15. In Figure 4. 17 a rough fluctuation in non-smoothed displacement vector is shown. Figure 4. 17 also shows how the smoothing process reduces the fluctuation in displacement vector that would attenuate the expected amplification in gradient operation for strain estimation [30].

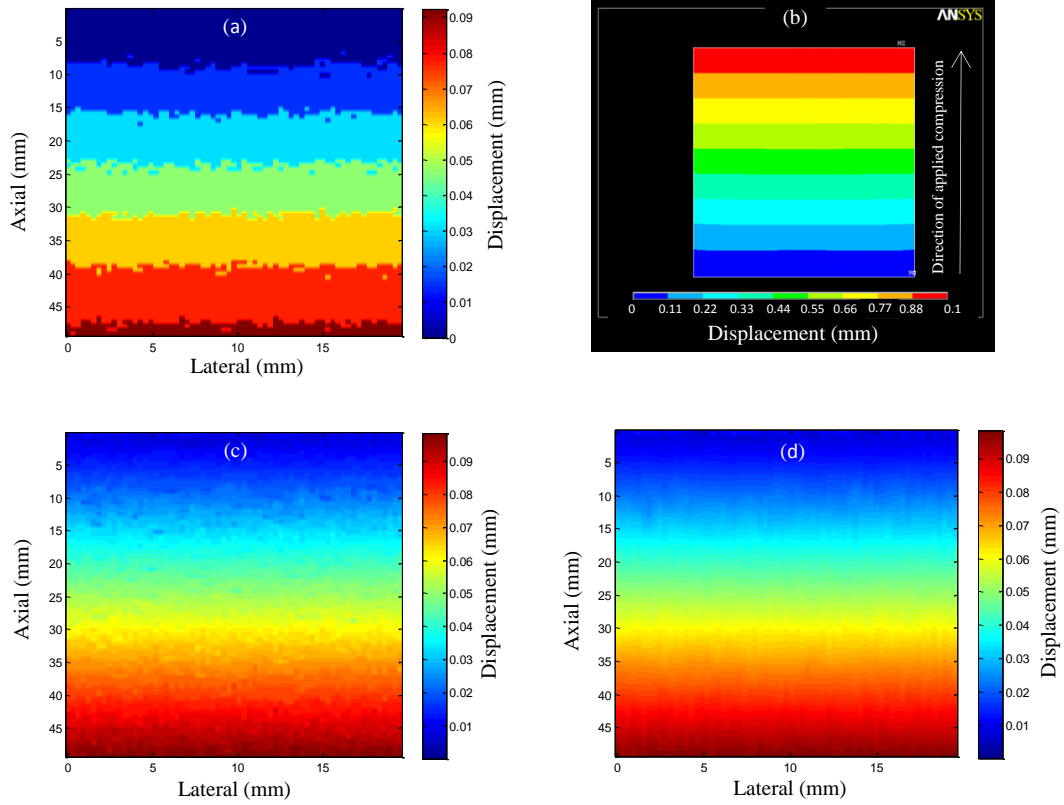


Figure 4. 16 (a) Non-interpolated, (b) FEM, (c) interpolated, (d) smoothing process.

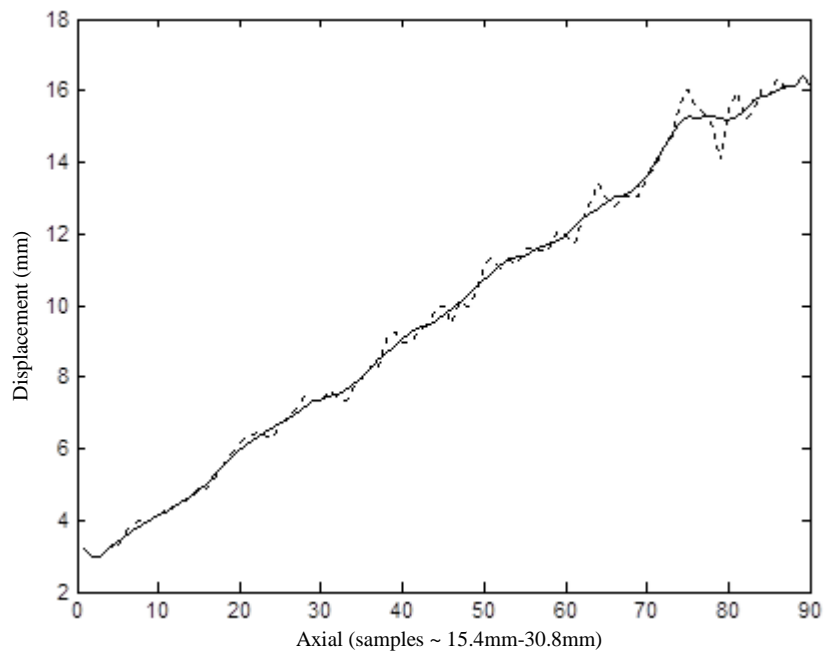


Figure 4. 17 Non-smoothed displacement vector (dotted-line) and smoothed displacement vector (solid-line).

In the strain estimation, gradient operation of (3.25) is performed on smoothed displacement field. Figure 4. 18(a) shows the strain field estimated from displacement without smoothing, while Figure 4. 18(b) shows the strain estimated using smoothed displacement field, it is clear that smoothing process of displacement improves the strain contrast.

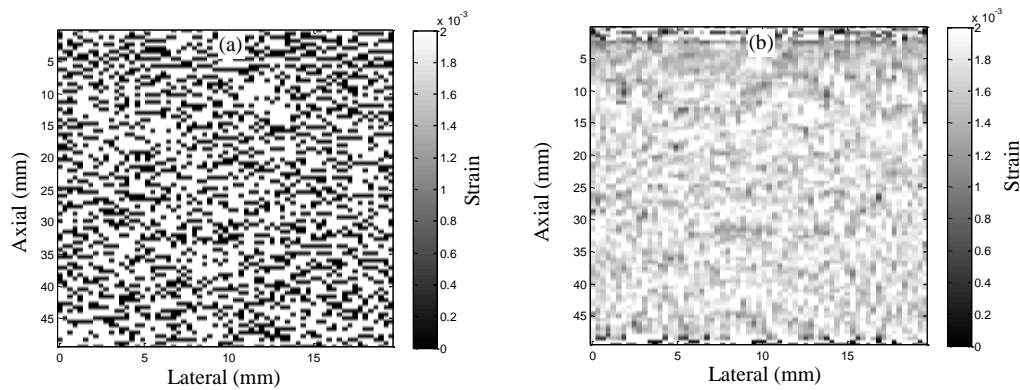


Figure 4. 18 (a) Strain fields without smoothing process and (b) with smoothing process.

On the other hand, the similar smoothing process is performed on heterogeneous model of ANSYS-11 that is shown in Figure 4. 11(a). In the imaging scenario of Field-II program, transducer of 128 elements, 16 active elements, 10MHz operating frequency, 100MHz sampling frequency, 0.3mm pitch, and 100000 scatterers are considered. In ANSYS-11 model, same applied compression of 0.1mm is applied.

In Figure 4. 19, a normalised correlation coefficient, displacement and strain with and without smoothing processes are shown. Figure 4. 19(a) shows the correlation coefficient map of 8λ correlation window length which indicates a reliable correlation between the pre-compression and post-compression frames. The high correlation is obtained due to small compression of 0.1mm (low decorrelation noise) and long enough correlation window length. The correlation is expected to be degraded when smaller correlation window length is performed or higher compression is applied, more details will be illustrated in 4.7.2 and 4.7.3 respectively.

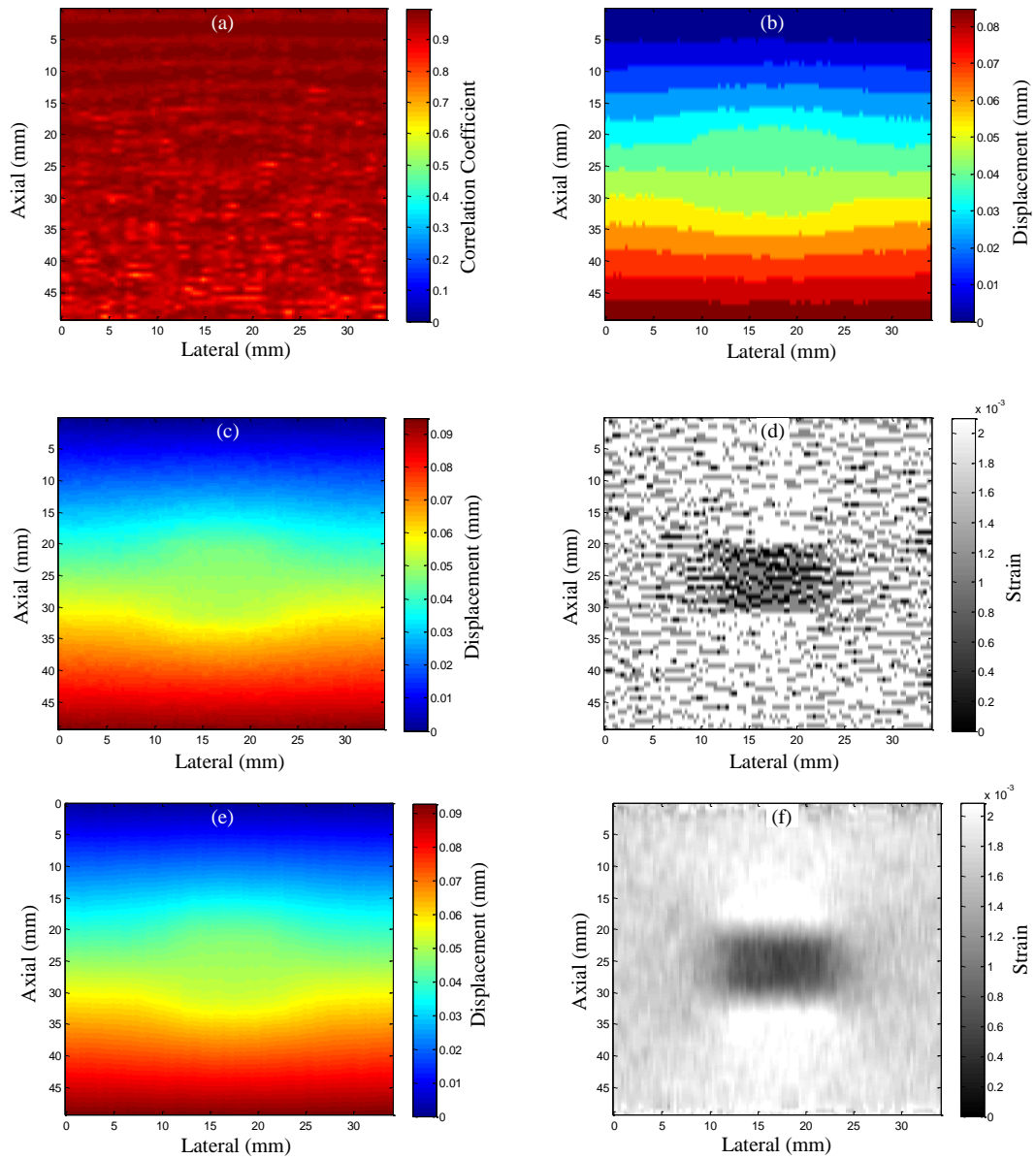


Figure 4. 19 (a) Heterogeneous model mapping of normalized correlation coefficient , (b) non-interpolated displacement , (c) displacement without smoothing , (d) strain without smoothing , (e) displacement with smoothing , and (f) strain with smoothing.

Figure 4. 19(b) shows the non-interpolated displacement where the inclusion region is clearly recognised at the middle of displacement field. Figure 4. 19(c and e) shows the displacement with and without smoothing process. It is clear that the smoothing process produces a reduction in displacement roughness that improves the strain

contrast as shown in Figure 4. 19(d and f). The noise in strain field of Figure 4. 19(d) has significantly reduced in Figure 4. 19(f) and also the edge of hard inclusion region is recognisable. Figure 4. 19(f) shows a coincidence in strain concentration located above and below the hard inclusion relative to the numerical estimation of using FEM analysis as shown in Figure 4. 20.

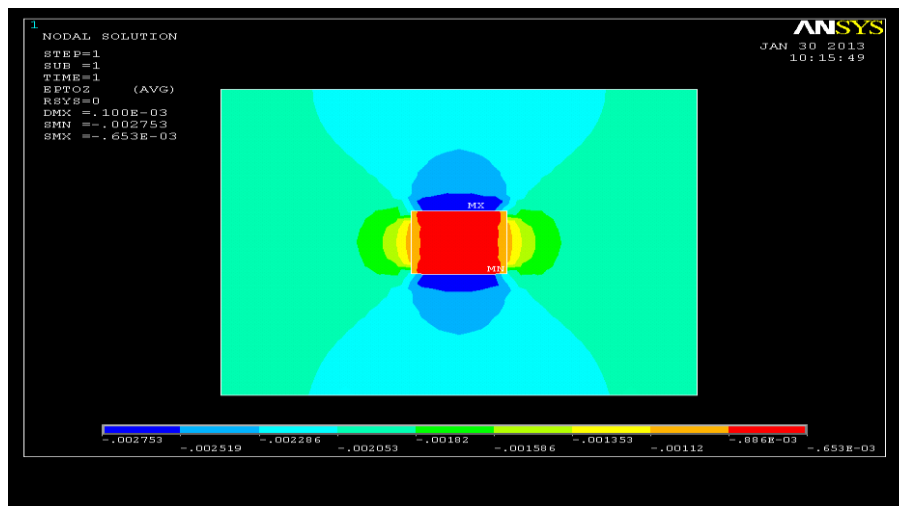


Figure 4. 20 Strain field of FEM heterogeneous model at 0.1mm compression (0.2%).

4.7.2 Small correlation window length

Decorrelation noise in the displacement estimation due to small correlation window length and high window overlap is considered in this section. In strained signals (signals before and after compression), a small correlation window length leads to low correlation due to a low level of similarity.

To show how decorrelation noise increases for small window length, and how it increases further by higher windows overlapping, window length of 4λ and 50% window overlapping are considered. Figure 4. 21(a and b) shows the displacement and strain fields, where the decorrelation noise occurs particularly in deep regions. . Although small window length of 4λ increases the strain spatial resolution compared to the previous estimation of 8λ (Figure 4. 19(f)), occurrence of decorrelation corrupts the smoothness. Additional decorrelation noise is also noticed, when window overlapping is increased to be 80%, Figure 4. 21(c and d). In which, a roughness in the gradient of displacement field (Figure 4. 21(c)) reflects noisy strain field, Figure 4. 21(d). Degradation in the performance of estimation algorithm due to small window length and high window length overlap is addressed to be considered in next chapters.

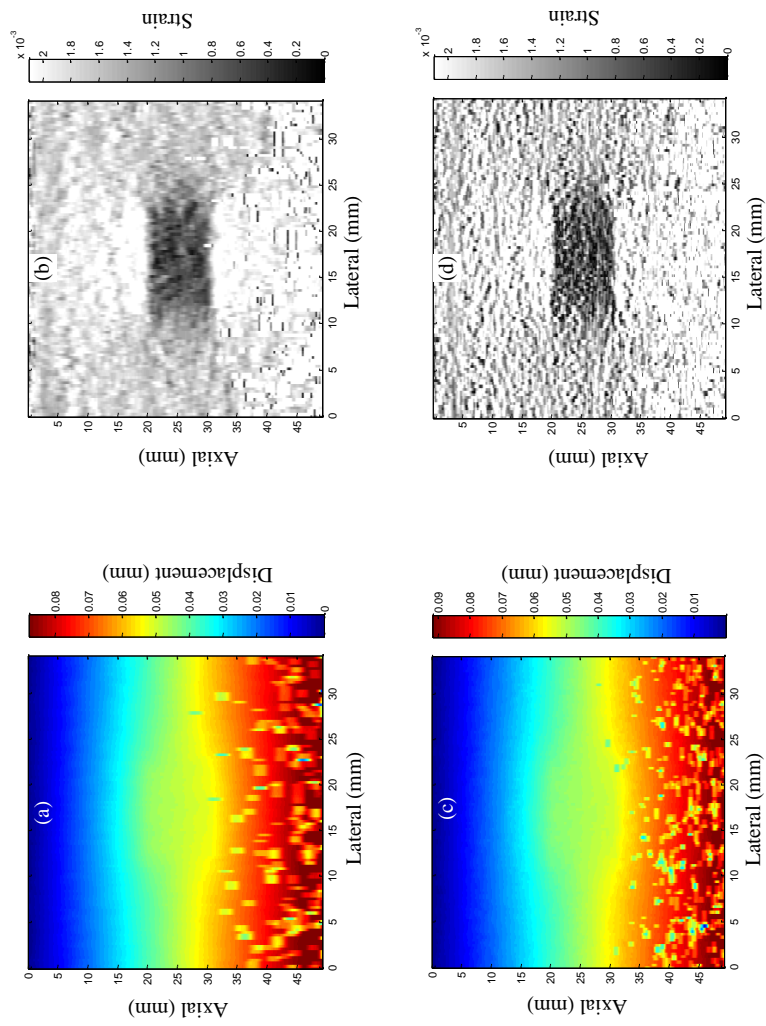


Figure 4. 21 Heterogeneous model of 0.2 % compression, (a) displacement of 4λ and 50% , (b) strain, (c) displacement of 4λ and 80%, (d) strain.

4.7.3 Performance against 1% compression

In applied compression of $\geq 1\%$, the decorrelation noise is expected to be increased. In addition to the axial decorrelation, scatterers can now move in lateral direction and out of plane direction leading to coherency loss particularly when using small window length. Figure 4. 22 shows a heterogeneous model of cylindrical hard inclusion of 15mm diameter with a 1% applied compression. Displacement and strain of 10λ and 5λ window lengths (50% overlapping) are shown in Figure 4. 22(a-d). In 10λ window length, smoothness of the displacement field is degraded at regions located away from the compressor, as shown in Figure 4. 22(a). This is due to the fact that the displacement is higher at bottom where scatterers are expected to be moved out of transducer beamwidth. The strain field of Figure 4. 22(b) shows a low strain region of interest that is corrupted by some noise particularly in lower edge of the region. Although the low strain region is recognizable, degradation in terms of high noise constriction is increased as a function of depth. Where background region located in the bottom of the inclusion is drastically corrupted, which might reduce the ability to recognise any small inclusion and also to visualize the distribution of strain over that region, Figure 4. 22(b).

On the other hand, using a 5λ window length (50% overlapping) degrades the displacement field severally, Figure 4. 22(c). While, Figure 4. 22(d) shows a very noisy strain field where the noise covers the entire region, where the hard region of interest cannot be recognized. The situation of using small window length to increase the spatial resolution of estimation will be considered in the next chapter, particularly when applied compression of $\geq 1\%$.

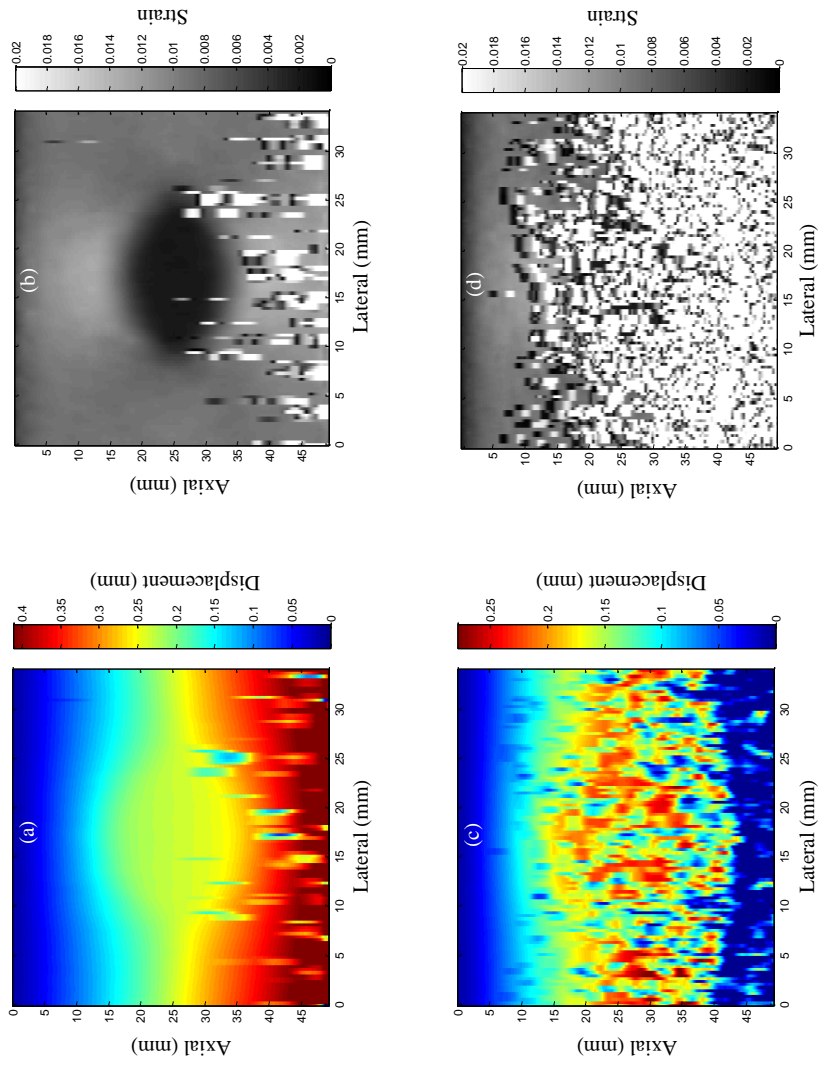


Figure 4. 22 (a) Heterogeneous model at 1% compression, displacement of $10\lambda_s$, (b) strain, (c) displacement of $5\lambda_s$, (d) strain.

4.8 Conclusion

A dynamic ultrasound scatterer simulation model was presented.. This model was a composition of the Field-II and FEM programs. Field-II simulates the imaging scenario, while FEM simulates mechanical compression scenario. The composition algorithm moves the scatterers in Field-II model according to displacement information of the nodes in FEM model. Axial displacement and strain field are estimated, displacement field is estimated using cross-correlation tool while strain field is estimated using gradient operation. Proposed method of smoothing process was shown to be effective on reducing the axial decorrelation noise, which was created as a result of strained signals . Strain field was shown to be in a good agreement with the ideal state of the FEM model. Performance of the algorithm is degraded when increasing the spatial resolution (small correlation window length) due to a loss in correlation (less similarity information). In addition, the estimation failed to alleviate the effect of non-axial decorrelation noise created as a result of using 1% compression. In the next chapter, an experimental validation of the simulation model will be introduced and robustness of the estimation algorithm is going to be verified by including the non-axial scatterer motion.

Chapter 5

Axial Displacement Field Regularization

5.1 Introduction

In section 4.7, a novel speckle tracking algorithm of using appropriate correlation window length and smoothing process of the displacement field was shown to be effective for small scale compression of 0.2%. On the other hand, 1% compression and small correlation window length were presented in section 4.7.2 and 4.7.3. Results indicated degradation in performance in terms of displacement inaccuracies and discontinuities.

Although, literature (section 3.5) was referred to different similarity compensation techniques, their effectiveness was shown to be limited. Recently, new approaches were suggested to regularize the displacement field by incorporating scatterer motion continuity into the displacement estimation process [1, 81, 90, 103, 112, 114].

The main contribution of this chapter is the introduction of a novel displacement regularization approach that provides outlier free estimation and good spatial resolution for up to 1% applied compression. This approach uses a refinement of the initial displacement field in a single statistical based trial resulting in low computational demands. However, unlike a probabilistic method of Bayesian regularization presented in [114] neither the Time Domain cross-correlation with Prior Estimated (TDPE) presented in [112], the refinement process does not involve a similarity metric in making the consistency decision, instead the decision is taken based on comparison with the initially estimated displacement of eight surrounding neighbours using optimal window length.

The results of using the simulation framework in Chapter 4 motivated us to construct an experimental set-up that will be a primary step toward real tissue elasticity imaging. In the experimental scenario, different parameters will be investigated, such as phased array linear scanning model, object model, and model of applied compression.

The rest of this chapter is organized as follows. The refinement algorithm is presented in Section 5.2. Experimental materials and settings are described in section 5.3. Comparative results and discussion are presented in Section 5.4.

5.2 Refinement Process Method

The SCC is considered as the main tool for displacement estimation. In this work SCC is used to estimate the displacement between segments of signals before and after compression (correlation windows). A block diagram of the methodology is shown in Figure 5. 1. Raw data before and after compression are acquired using phased array linear scan and then transferred to personal computer for off-line processing. The RF data set of before compression and after compression are segmented axially and overlapped. An initial displacement field is estimated using subsample localization of SCC peaks. A novel neighbourhood consistency detection process is used to classify the estimated cells as either consistent or not consistent. A refinement to the displacement field is carried out on the non-consistent cells using the neighbourhood information. The strain field map is computed from the refined displacement field using LSQSE [30]. Each part of the overall algorithm will now be described in detail.

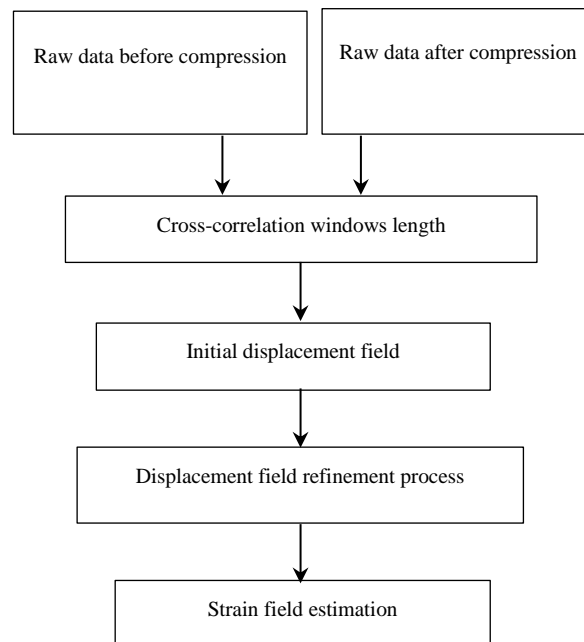


Figure 5. 1 Block diagram of the proposed methodology.

5.2.1 Correlation windows length

To estimate initial displacement field, the SCC is used (3.19). The methodology presented in chapter 4 was used equally windows length of both pre-compression and post-compression, particularly for small-scale compression of 0.2%. In section 4.7.2, the performance was shown to be degraded for 1% compression, where correlation loss appeared as estimation outliers, Figure 4. 22.

To alleviate the effect of correlation loss, similarity compensation is required (section 3.5). Small enough post-compression window length, and at the same time long enough pre-compression window length is considered as axial compensation process. Both of the windows length are investigated in an empirical way based on visual observation of displacement and strain fields. The pre-compression window length is increased by ratio called post-to-pre window length ratio for the range of 1-1.6. The optimal windows length are defined as the length that reduces the number of occurrence of estimation outliers within a certain space of refinement operation (3x3 dimension). The reduction of outlier occurrence will enable the refinement process to regularize the displacement field. Figure 5. 2 shows a representation of segment of initial displacement field, where refinement space of operation (3x3 dimension) is highlighted by green colour. This representation diagram describes how the occurrence of estimation outliers will be changed when using the optimal correlation windows length. In Figure 5. 2(a), the occurrence outliers and correct estimations are in split regions. In the refinement operation space (green colour area), the number of estimation outliers (symbol x) are five. In refinement process, the median value is designed to be a fourth order, so that CUI will be exchanged by the outlier. While in Figure 5. 2(b), the occurrence of outliers and correct estimations are dispersed. In the refinement operation space (green colour area), the number of occurrence of estimation outliers are three, so that CUI will be exchanged by the correct estimation.

o	o	o	o	o	o	o	o	o
o	o	o	o	o	o	o	x	o
o	x	o	x	x	o	o	x	o
o	x	x	o	x	o	x	x	o
x	x	o	x	CUI	o	x	x	o
o	x	x	x	x	x	x	x	o
o	x	x	o	x	x	o	x	x
o	x	o	o	o	o	o	o	o
o	o	o	o	o	o	o	o	o

(a)

o	x	o	o	o	x	o	o	x
o	x	o	o	x	o	o	x	o
o	o	o	o	x	o	o	o	x
o	x	o	o	x	o	o	x	o
x	o	o	o	CUI	o	x	o	o
o	x	o	x	o	x	o	o	x
x	o	o	o	x	o	o	x	o
o	x	o	o	o	o	o	x	o
o	o	x	o	x	o	o	o	x

(b)

Figure 5. 2 A segment of displacement field with certain 3x3 region of interest (highlighted by green colour) at, (a) non-optimal correlation windows length, (b) optimal correlation windows length. Symbol x represents estimation outlier, while symbol o represents correct estimation.

We will now investigate the correlation loss using RF-data acquired by experiment. The RF-data acquired before and after applying compression of 1%. The SCC is performed for two different regions of TMM model using same correlation windows length. Figure 5. 3(a) shows the pre-compression (solid line) and post-compression (dashed line) signals of the first region. Figure 5. 3(b) is the correspondence cross-correlation function. A reliable correlation is conducted by around 0.9 correlation coefficient. On the other hand, similarity is poor between the pre-compression and post-compression signals from the second region, Figure 5. 3(c). Figure 5. 3(d) shows a disappearance for reliable peak in correlation function. The reliable correlation function depicts the correct estimation of the displacement, while dismissing of it depicts estimation outlier.

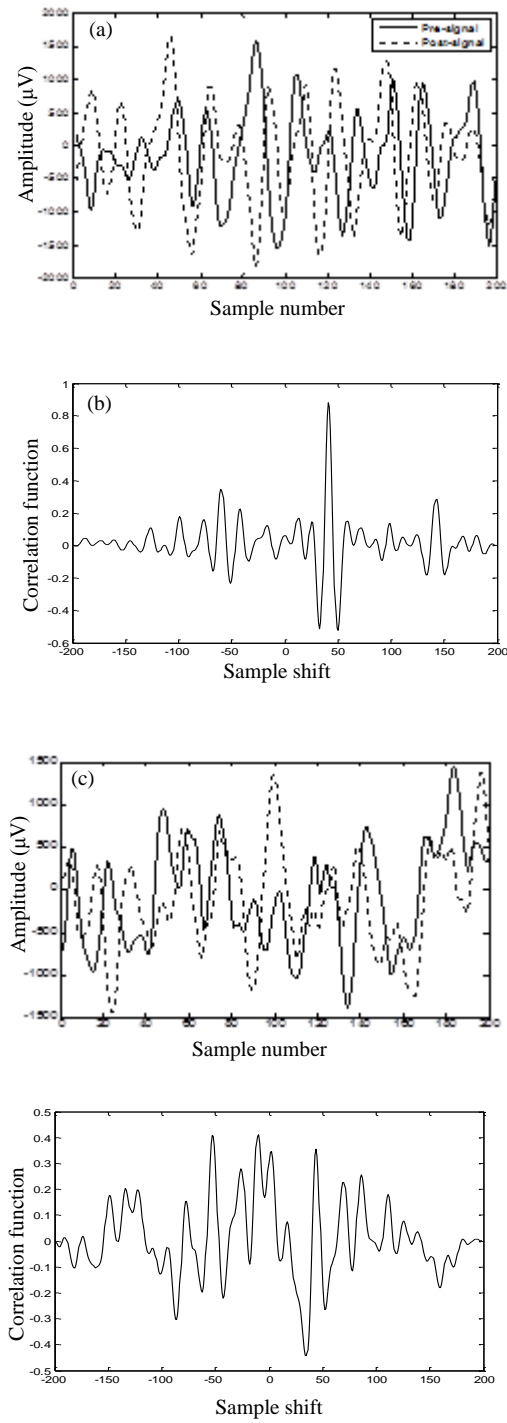


Figure 5. 3 Pre-compression (solid line) and post-compression (dashed line) RF signals of two different regions, (a) for high correlation, (b) correspondent correlation function, (c) low correlation and (d) correspondent correlation function.

5.2.2 Initial displacement field

In each frame before and after compression, sequential correlation windows in axial direction are overlapped by 50% of window length, as shown in Figure 5. 4. L_b and L_a are the windows length before and after compression, L_b is slightly longer than L_a by the post-to-pre ratio (R_L) which means $L_b \geq L_a$, and $L_b = R_L L_a$, where R_L is in the range of 1-1.6. For each step of SCC, quadratic interpolation of spline is performed to localize a subsample peak position. Interpolation provides sub-sample differentiation on displacement field mapping. The initial displacement field is then post processed to remove the estimation outliers based on continuity assumption of surrounding scatterers motion. The procedure to estimate initial displacement field is described in Table 5.1.

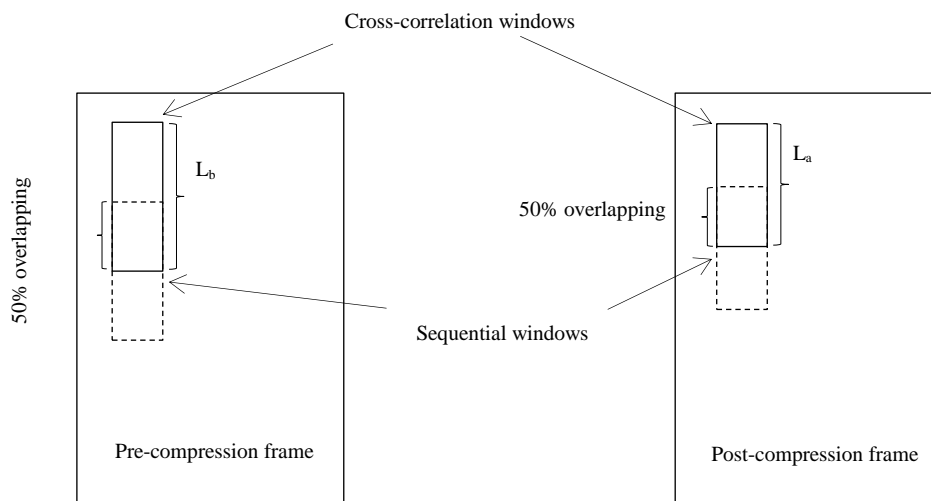


Figure 5. 4 Sequential correlation windows (pre-compression and post-compression windows) are overlapped by 50% in each frame.

Table 5.1 Estimation of initial displacement

1. Load RF data region of interest (2D matrix) of before and after compression.
2. Apply cross-correlation operation (3.6) using post-compression window length of at least 5λ , and pre -to-post window length ratio of at least 1.4.
3. Perform a spline interpolation for the correlation function to differentiate the sub-sample delays.
4. Update the RF-data for next correlation windows and then repeat steps (2 and 3) to generate the initial displacement vector.
5. Update the RF-data for next A-scan to generate initial displacement field.
6. Reduce the correlation windows length in an empirical way (visual observation of initial displacement field) that realizes dispersion of the outliers, Figure 5. 2.

5.2.3 Refinement process

We will now consider how to determine the correct displacement field in the presence of decorrelation noise. Regularization of the initial displacement field can be performed based on neighbours information that have been classified as consistent neighbours. To address this, refinement algorithm step shown in Figure 5. 1 is proposed that aims to correct non-consistent measurements (outliers) in the initial displacement field.

Figure 5. 5 illustrates the refinement process where the initial estimated displacement field is the input to this flowchart. Then, the cells in the initial displacement field are labelled as illustrated in Figure 5. 6. There are three types of Cell Under Interest (CUI): Internal, Edge and Corner CUIs each with eight neighbouring cells.

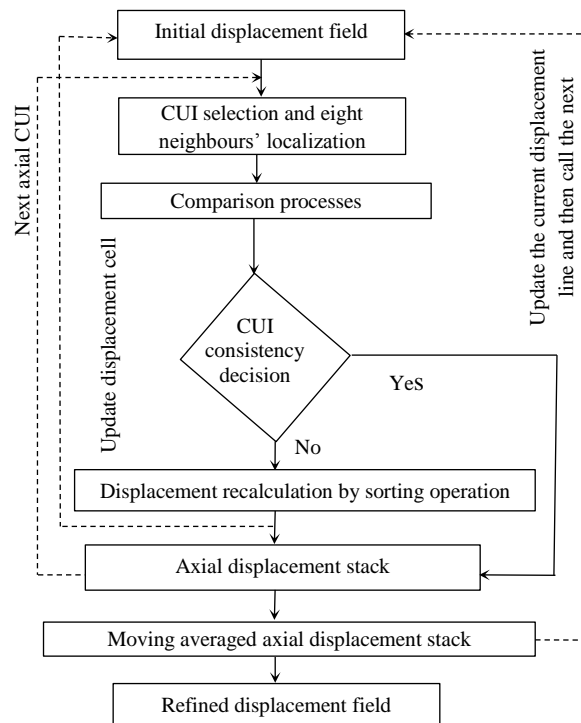


Figure 5. 5 Flowchart of displacement field refinement process.

The consistency of each CUI is determined according to its relative relation to the eight surrounding neighbours using the Bernoulli Trials concept [115]. Bernoulli Trials is an identical repetition process of a random experiment with only two outcomes. Outcomes are encoded as “1 or 0” where the symbols of “1” and “0”

represent success and failure of an occurrence respectively. The relative relation of each CUI to the eight surrounding neighbours is measured, and then marked as “1” or “0”. This measurement is performed by comparison process, which is considered according to a spatial variation of estimated displacement field due to depth dependency as follows

$$NC_i = \frac{|d_{CUI} - d_{N_i}|}{\max(d_{CUI}, d_{N_i})} \quad (5.1)$$

where, NC_i is the normalized comparison vector component, d_{CUI} and d_{N_i} are the initial displacement measurement of CUI and its neighbours ($i = 1, 2, \dots, 8$) respectively. If one of the terms in the numerator of (5.1) is significantly larger than the other, then NC_i approaches unity. If the two terms in the numerator of (5.1) are approximately equal, then NC_i approaches zero. A very small NC_i reflects a highly consistent displacement of CUI, whereas the NC_i close to unity indicates non-consistent initial displacement estimation.

CUI	N ₁	N ₃	...	N ₁	CUI	N ₂	...	N ₃	N ₁	CUI
N ₂	N ₄	N ₆	...	N ₃	N ₄	N ₅	...	N ₆	N ₄	N ₂
N ₅	N ₇	N ₈	...	N ₆	N ₇	N ₈	...	N ₈	N ₇	N ₅
⋮	⋮	⋮		⋮	⋮	⋮		⋮	⋮	⋮
N ₁	N ₃	N ₆	...	N ₁	N ₂	N ₃	...	N ₆	N ₃	N ₁
CUI	N ₄	N ₇	...	N ₄	CUI	N ₅	...	N ₇	N ₄	CUI
N ₂	N ₅	N ₈	...	N ₆	N ₅	N ₈	...	N ₈	N ₅	N ₂
⋮	⋮	⋮		⋮	⋮	⋮		⋮	⋮	⋮
N ₃	N ₆	N ₈	...	N ₆	N ₇	N ₈	...	N ₈	N ₇	N ₃
N ₁	N ₄	N ₇	...	N ₃	N ₄	N ₅	...	N ₆	N ₄	N ₂
CUI	N ₂	N ₅	...	N ₁	CUI	N ₂	...	N ₃	N ₁	CUI

Figure 5. 6 Identification of the eight neighbors for different CUI locations.

The NC_i measures are converted into binary output using the following row dependent threshold process:

For d_{N_i} in the same CUI row

$$\left. \begin{array}{l} NC_i \geq T_{rd} \quad \text{then } B_i = 1 \\ NC_i < T_{rd} \quad \text{then } B_i = 0 \end{array} \right\} \quad (5.2)$$

For d_{N_i} that have single row difference relative to CUI

$$\left. \begin{array}{l} NC_i \geq 2T_{rd} \quad \text{then } B_i = 1 \\ NC_i < 2T_{rd} \quad \text{then } B_i = 0 \end{array} \right\} \quad (5.3)$$

For d_{N_i} that have double row difference relative to CUI (corner CUIs)

$$\left. \begin{array}{l} NC_i \geq 3T_{rd} \quad \text{then } B_i = 1 \\ NC_i < 3T_{rd} \quad \text{then } B_i = 0 \end{array} \right\} \quad (5.4)$$

where T_{rd} is row dependent threshold, which is in the range of $0 < T_{rd} < 1$.

The consistency process (Bernoulli Trials) is achieved by comparing summation of binary output vector (B_i) to a consistency decision threshold T_{cd} :

$$C = \sum_{i=1}^8 B_i \quad (5.5)$$

where C is the summation of the ones in the binary output vector.

As indicated in Figure 5. 5, the CUI consistency decision process compares C to T_{cd} , where T_{cd} is defined as the consistency decision threshold.

$$\left. \begin{array}{l} C \geq T_{cd} \\ C < T_{cd} \end{array} \right\} \begin{array}{l} \text{then CUI is inconsistent} \\ \text{then CUI is consistent} \end{array} \quad (5.6)$$

Accordingly, when the decision is taken for non-consistency, as shown in Figure 5. 5, recalculation process is carried out by sorting the displacement set of eight neighbours. Then the CUI will be changed to a rank four d_{s_4} of sorted displacement set $[d_{s_N}]$ where;

$$d_{CUI} = \text{Rank four } [d_{s_1} \leq d_{s_2} \leq \dots \leq d_{s_8}] \quad (5.7)$$

A new displacement value is updated simultaneously. Resultant displacement cells are stacked for each axial line of estimation, and then interpolated linearly to be averaged using moving average window to smooth the displacement field. Finally, all axial lines are processed in a similar fashion to refine the whole initial displacement field. The procedure to perform the refinement process is tabulated in Table 5.2.

Table 5.2 Refinement process

1. Load 2D matrix of initial displacement field, which is determined based on the procedure illustrated in Table 5.1. Then, label each cell and its surrounding eight neighbours, Figure 5. 6.
2. Perform the comparison process using (5.1), to generate the normalized comparison vector.
3. Convert the normalized comparison vector into binary comparison vector using (5.2-5.4).
4. Perform consistency decision process based Bernoulli Trial using (5.5 and 5.6).
5. If the displacement measurement of CUI is considered as inconsistent, sort the displacement measurements of the eight neighbours.
6. Change the inconsistent displacement measurement of CUI by the rank four of the sorted neighbours' measurements (5.7).
7. Apply smoothing process to each refined vector.
8. Update the new displacement vector, then repeat steps (2-7).
9. Optimize the refinement thresholds of T_{rd} and T_{cd} to regularize any residual displacement estimation outliers. The optimization process is considered in a conjunction of reducing the correlation window length by visual observation of refined displacement field.

5.2.4 SNR and CNR of strain

The strain field is estimated using LSQSE algorithm, which was explained in section 3.4.2. As shown in Figure 5. 1, the refined displacement field is an input of strain estimation. Thus, four displacement measurements is considered for strain estimation. For quantitative comparison, the quality of strain field of homogeneous model is measured using metric of SNR, while heterogeneous model is measured using metric CNR [13, 75].

$$\text{SNR} = \frac{\text{mean}(s)}{\text{std}(s)} \quad (5.8)$$

where, mean and standard deviation (std) are calculated for the strain (s) region of interest.

$$\text{CNR} = \sqrt{\frac{2(\text{mean}(s_i) - \text{mean}(s_b))^2}{(\text{var}(s_i) + \text{var}(s_b))}} \quad (5.9)$$

where, mean and variance (var) are calculated for the strain regions of interest within inclusion (s_i) and background (s_b). The procedure of strain estimation is described in Table 5.3.

Table 5.3 Strain estimation based LSQSE

1. Load 2D matrix of refined displacement field.
2. Set the segment length (n) of displacement estimates for linear regression to calculate the gradient estimator \hat{v} using (3.15).
3. Update the segment estimates by cell-in and cell-out over the displacement vector to generate the strain vector.
4. Calculate the SNR of strain field for homogeneous model using (5.8), and the CNR for heterogeneous model using (5.9).

5.3 Materials

Raw ultrasound data was obtained from a tissue mimicking phantom. The details of data acquisition machine, tissue mimicking models, and experiment scenarios are explained as follows;

5.3.1 Raw data acquisition

A DYNARAY ultrasonic Phased Array Controller (Zetec, Québec, Québec, Canada) is used for raw data acquisition with a sampling frequency of 100MHz, quantization of 12 bit. The 10MHz, 128 element probe (Imasonic, Les Savourots, Voray-sur-l'Ognon, France) was mounted on the arm of an XYZ scanner using a bespoke adaptor. Both the ultrasound transducer and the XYZ scanner are controlled using a main PC as shown in Figure 5. 7. The XYZ scanner is used to apply strain (compression) to the specimen. Sixteen of 128 probe elements are used in linear scan mode, creating 113 A-lines.

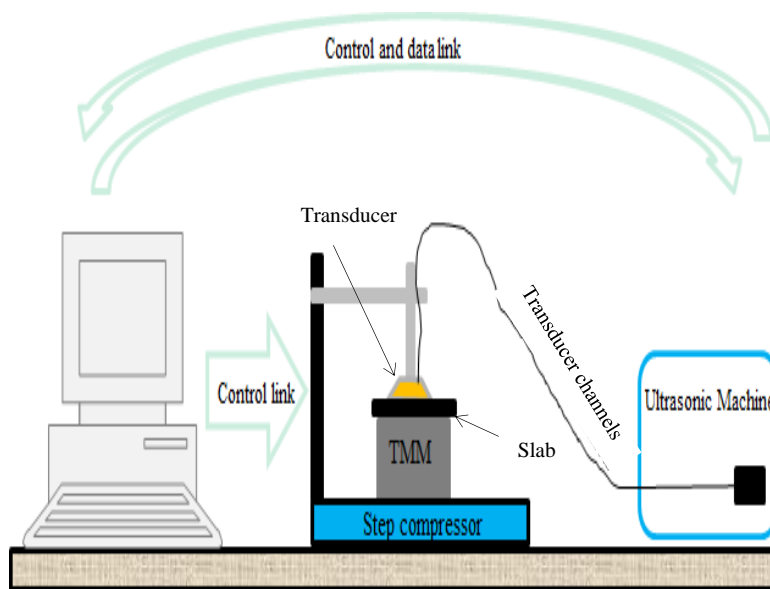


Figure 5. 7 Diagram of experiment set up.

5.3.2 Anthropomorphic phantom

Using the tissue TMM manufacturing process described in [116], it is possible to modify the IEC 61685 agar-based TMM [117, 118] to have a wide range of acoustical properties to mimic different tissues. The TMM composition is detailed in Table 5.4. By altering the concentration of the particles (Aluminium Oxide (3 and 0.3 μ m) or silicon carbide (400 grit)), it was possible to alter the attenuation and backscatter properties. Modifying the concentration of Agar can increase or decrease the elastic properties. For this work, homogeneous phantom model was constructed from the components detailed in Table 5.4. The heterogeneous model was constructed by doubling the concentration of agar to manufacture the embedded objects. With the object suspended within a suitable container, the surrounding space was filled with the same material used in the homogeneous model.

The homogeneous model was manufactured from a cylindrical shape with a 100mm base diameter and 55mm height, while the heterogeneous model includes a cylinder of 15mm diameter placed horizontally and imbedded into the middle of phantom background material. In the heterogeneous model, both the inclusion and the background have the same acoustic properties of the IEC 61685 material. The phantom was characterized using a scanning acoustic microscope (Ultrasonic Sciences Limited, Fleet, UK) to measure the attenuation, and speed of sound at a temperature of 20°C, which was found to be 0.5 ± 0.03 dB/cm.MHz and 1537 ± 1.9 m/s (mean \pm 1 SD) between 5 and 15 MHz respectively [116, 117].

A square Perspex slab was used to equalize the strain around the ultrasonic probe. The transducer was fit through a window in the slab, with dimension of 5mm thickness and 120mm side length, see Figure 5. 8. The phantom was situated under a central point of compression slab, while upper and lower surfaces are oiled using glycerol as an ultrasonic couplant. The couplant is a viscous gel based material, which is used to facilitate the transmission of acoustic energy at contact area by filling the air gap between probe face and testing surface.

Table 5.4. Standard components of the IEC 61685 agar-based tissue mimicking material.

Components	Weight Concentration	Order Code and Manufacturer / Distributor Details
Water	[82.97%],	
Glycerol 99% (PURE)	[11.21%],	(G7757) Sigma-Aldrich Company Ltd. The Old Brickyard, New Road, Gillingham, Dorset, UK.
Merck Agar – Agar Technical (111925)	[3%],	(53648 5K) VWR International Ltd. Hunter Boulevard, Magna Park, Lutterworth, Leics, UK.
3 μ M AL ₂ O ₃ Powder	[0.95%],	Logitech Ltd. Erskine Road, Old Kilpatrick, Glasgow, Scotland.
0.3 μ M AL ₂ O ₃ Powder	[0.88%],	
400 Grain SIC Powder	[0.53%],	
Benzalkoniumchloride	[0.46 %].	(09621) (50% solution, diluted in-house to 10%) Sigma-Aldrich Company Ltd. The Old Brickyard, New Road, Gillingham, Dorset, UK.

5.3.3 Experiment scenario

In the experiments, an initial 2% (1.1mm) axial compression was applied using a mechanical scanner, to ensure a firm contact between transducer and phantom surfaces, Figure 5. 8(a).

Both the homogeneous TMM model and the heterogeneous TMM model were scanned in similar procedure. The scanning procedure was to acquire the pre-compression raw data first using linear phased array scanning, details in section 5.3.1, then applying the compression of 1% (0.55mm) over the upper surface of the TMM model (axial compression) using XYZ scanner. After applying the compression, the post-compression raw data was acquired using the same linear phased array scanning process, Figure 5. 8(b).

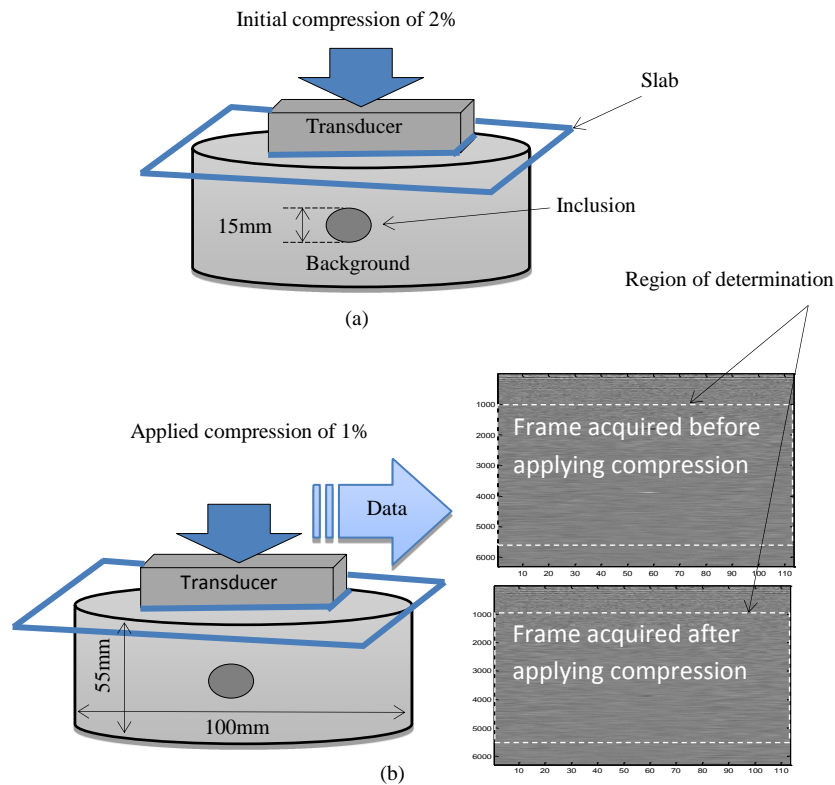


Figure 5. 8 Experiment scenario of, (a) initial and (b) applied compression.

5.4 Results and Discussion

This section compares the relative performance of the refinement and non-refinement algorithms in terms of visual and quantitative comparison. The section also investigates the refinement algorithm threshold parameters of T_{cd} and T_{rd} . Generally, refinement algorithm enhances the displacement field by reducing the standard deviation of displacement gradient that would ultimately reduce the noise over the strain field.

5.4.1 Visual and quantitative comparison

Displacement and strain field of 1% axially applied compression over homogeneous TMM without and with refinement process are shown in Figure 5. 9. Figure 5. 9(a and b) represents the displacement fields, while Figure 5. 9(c and d) represents the strain fields, for algorithm parameters of consistency decision threshold $T_{cd}=4$, row dependent threshold $T_{rd}=0.1$, correlation window length of 5λ , and post-to-pre window length ratio of 1.4.

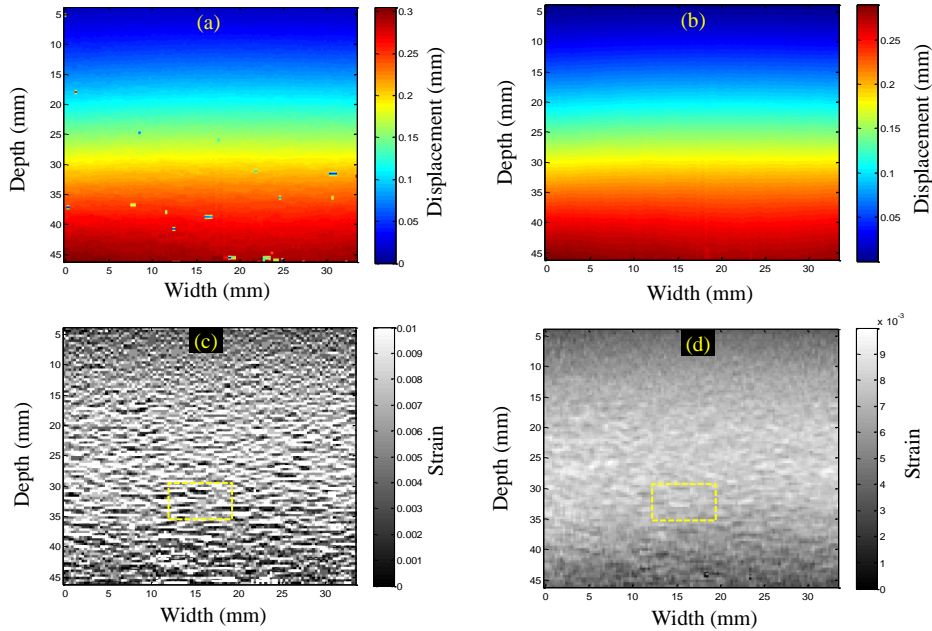


Figure 5. 9 (a and b) Displacement and (c and d) strain (bottom) fields of homogeneous TMM, (a and c) without and (b and d) with refinement process. The yellow dashed triangle represents the region of interest for SNR calculation.

The displacement field without refinement process of Figure 5. 9(a) is corrupted by decorrelation noise that is shown in the form of gradient roughness (displacement estimation outliers and displacement drifts). The roughness in the displacement gradient is smoothed by refinement process that is shown in Figure 5. 9(b). Figure 5. 9(c) shows how the roughness in displacement gradient is amplified in the strain field due to the gradient operation of strain estimation. This amplification is significantly reduced the contrast of the strain field of Figure 5. 9(c). However, an elimination of displacement outliers and smoothing of the displacement gradient are significantly impact into producing a good contrast strain field as shown in Figure 5. 9(d). As a result, refinement process is able to eliminate estimation outliers and at the same time to reduce estimation roughness.

Mean and STD of the strain field in the region of interest indicated in the strain fields of Figure 5. 9(c and d) with and without refinement process are compared in Figure 5. 10, as a function of window length that has been expressed in wavelength. It is clear that the refinement process has kept a constant mean of the strain with a relatively small STD. However without the refinement process, the mean and STD are relatively large for window lengths smaller than 7λ ($\lambda=0.154\text{mm}$). In other words, refinement process reinforces the strain estimation in terms of increases strain dynamic range while keeping constant axial resolution (window length).

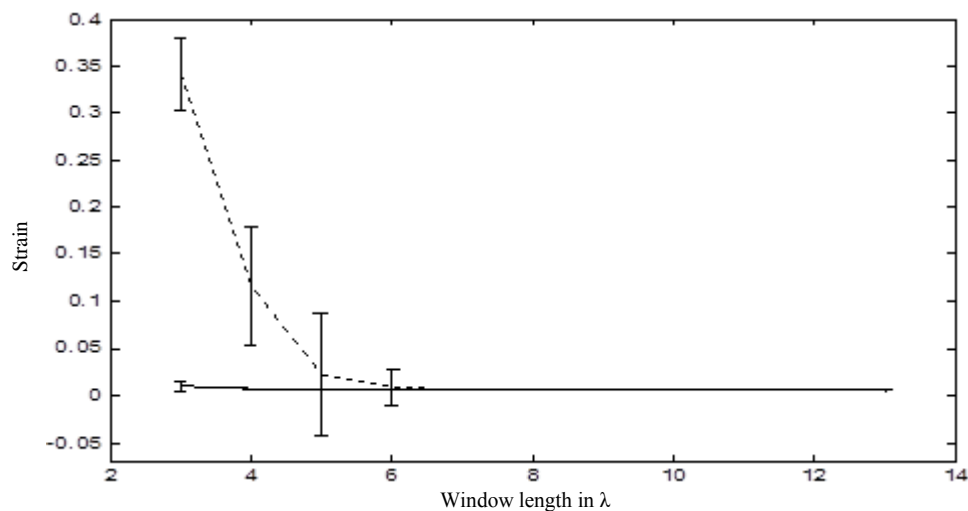


Figure 5. 10 Mean and STD (error bar) of strain region of interest with (solid line) and without (dashed line) refinement process.

Quantitatively, the strain field is established by calculating the amount of noise (SNR) within region of interest using (5.8) for strain without and with refinement process for the range of correlation window length (5λ - 13λ). In Figure 5. 11, the SNR of the strain with refinement process is shown to be higher than the SNR without refinement process. It has been noticed that, SNR of strain without refinement is very poor at correlation window less than 7λ . This drastic decrease in SNR illustrates how rapid changes in strain profile.

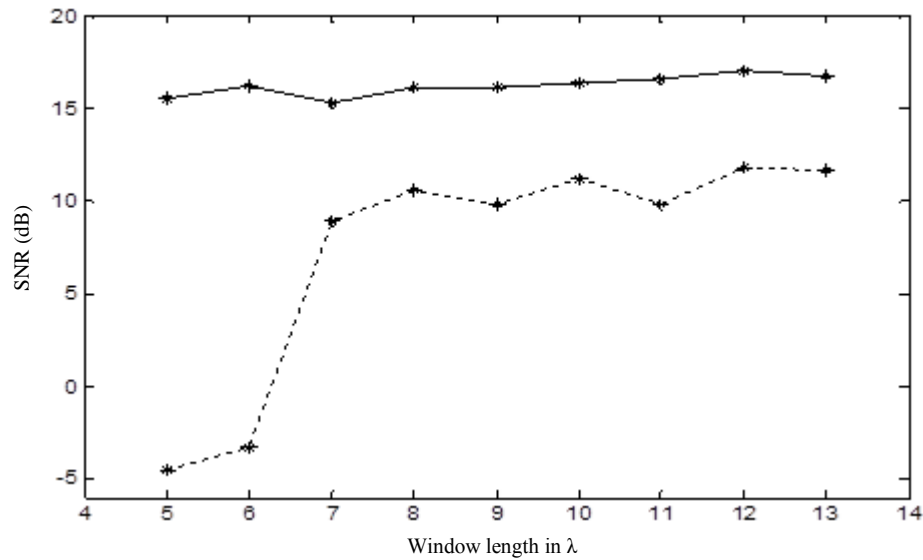


Figure 5. 11 SNR of strain region of interest without (dashed line) and with (solid line) refinement process.

Displacement and strain field of 1% axially applied compression over the heterogeneous TMM without and with refinement process are shown in Figure 5. 12. The correlation window length of 5λ and 1.4 post-to-pre window length ratio are performed to estimate the initial displacement field Figure 5. 12(a). Refinement process is then performed to regularize the displacement field for the parameters of $T_{cd}=4$ and $T_{rd}=0.1$, as shown in Figure 5. 12(b). Strain fields of without and with refinement are also shown in Figure 5. 12(c and d). As expected, strain field using refinement process has the ability to discriminate regional function of tissue under compression. Furthermore, displacement outliers due to non-uniform scatterer motion are eliminated. The resultant strain field is smooth and makes it possible to

identify hard and soft regions, where the heterogeneous TMM is recognized in term of regional low strain.

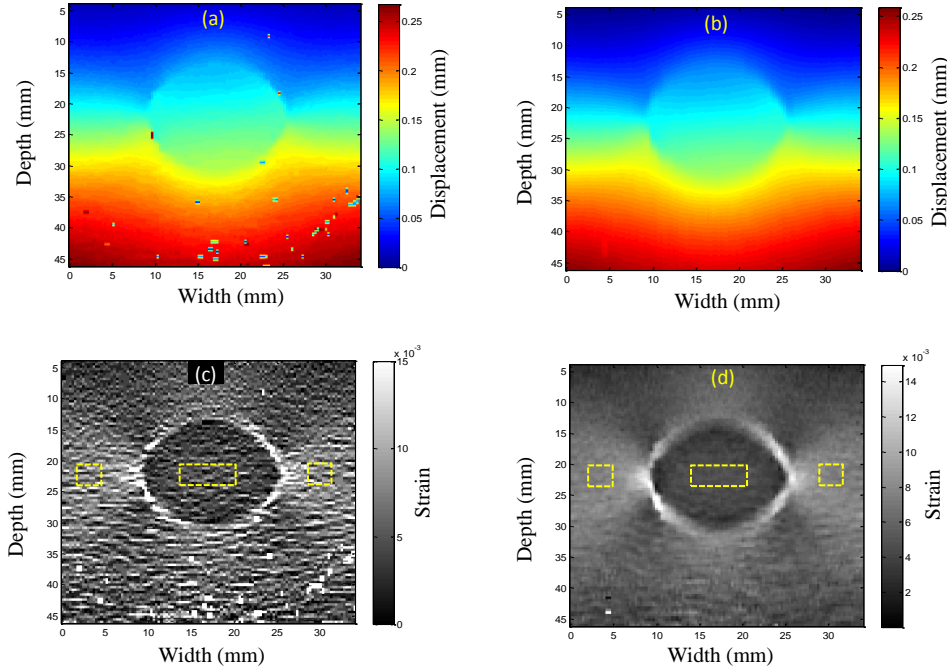


Figure 5. 12 (a and b) Displacement,(c and d) strain fields of heterogeneous TMM, (a and c) without and (b and d) with refinement process.

Quantitatively, CNR of strain regions of interest (highlighted in Figure 5. 12(c and d)) is calculated using (5.13), for the strain without and with refinement process of heterogeneous TMM at $T_{cd}=4$, $T_{rd}=0.1$ and 1.4 post-to-pre window length ratio, as a function of correlation window length for the range of 5λ - 13λ , Figure 5. 13. This figure shows a superiority of strain with refinement in term of higher CNR over the range of correlation window length.

5.4.2 Effectiveness of refinement parameters

This section investigates how the refinement parameters of T_{rd} and T_{cd} can be adjusted optimally to enable of using small correlation window length for higher strain spatial resolution. As shown in section 5.4.1, refinement process is effectively

removed the estimation outliers for homogeneous strain field (Figure 5. 9) and heterogeneous strain field (Figure 5. 12), using correlation window length of 5λ . However, the strain profile of Figure 5. 10 show the effectiveness of using refinement process for small correlation window length of 4λ , and with slightly increase of the standard deviation at 3λ .

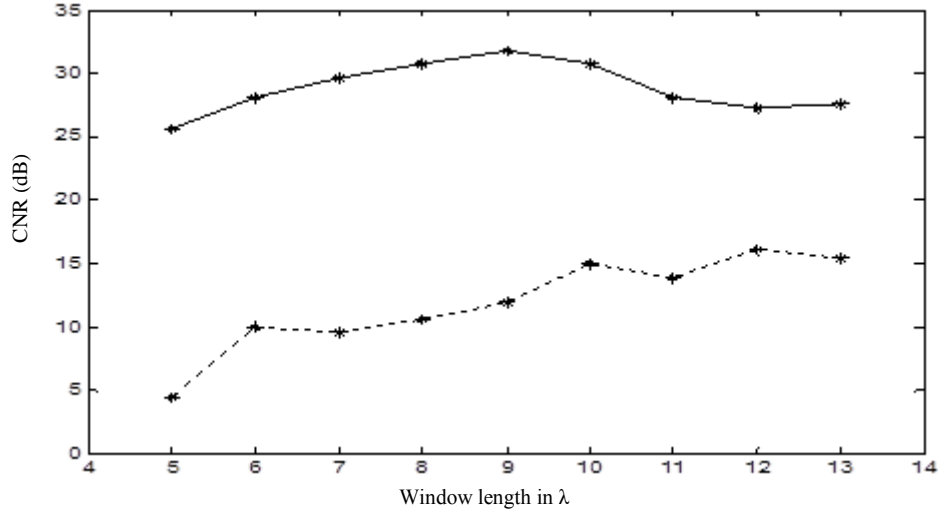


Figure 5. 13 CNR of strain region of interest without (dashed line) and with (solid line) refinement process.

The adjustment of the parameters is started by investigation of homogeneous strain field. A robustness of decreasing the refinement threshold of $T_{cd}=2$ (it was $T_{cd}=4$ in Figure 5. 9) will be investigated first for different correlation window length of 4λ and 5λ . At the same time, keep $T_{rd}=0.1$ and post-to-pre window length ratio of 1.4. Figure 5. 14 shows that the strain field of using window length of 4λ Figure 5. 14(a) includes some of estimation outliers compared to using window length of 5λ Figure 5. 14(b). So that the robustness of T_{cd} is revealed low effectiveness to produce outlier free strain field at smaller correlation window length.

For heterogeneous strain field, the performance of refinement process is investigated for different correlation window lengths of the range 2λ - 5λ , Figure 5. 15. $T_{cd}=4$, $T_{rd}=0.1$ and 1.4 pre-to-post window length ratio are kept same as Figure 5. 12. Figure 5. 15 shows an increase of estimation outliers with decrease of correlation window length. A significant increase of the estimation outliers is at 2λ window length. From the result shown in Figure 5. 15, we can conclude that the possibility of increase the

robustness of refinement process to regularize the estimation particularly for 3λ window length.

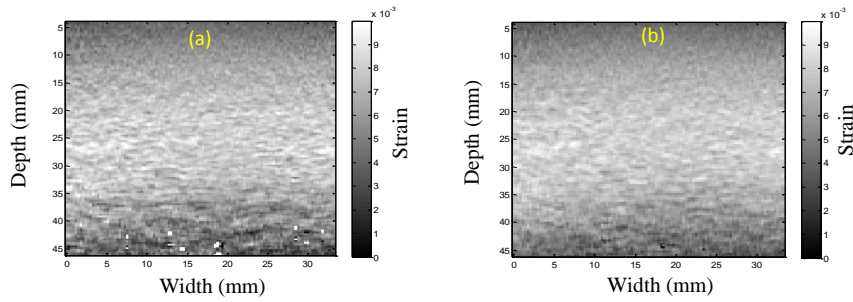


Figure 5. 14 Strain field of homogeneous TMM for $T_{cd}=2$, 1.4 pre-to-post window length ratio and different correlation window length of (a) 4λ and (b) 5λ .

The effectiveness of increase the robustness of refinement process at 3λ correlation window length is now considered. The refinement threshold of T_{rd} is reduced to 0.03, and at the same time the pre-to-post window ratio is increased to 1.6. The threshold of $T_{cd} = 4$ is kept the same as in Figure 5. 15. Figure 5. 16 shows the displacement field and strain field of without and with refinement process. Figure 5. 16(a) shows displacement field of without refinement, which is corrupted by dispersed estimation outliers. Figure 5. 16(b) shows low quality strain field as a result of amplification of high spatial frequency noise (non-consistent) displacement estimations. Figure 5. 16(c and d) shows an improvement in the quality of estimation of displacement and strain fields as a result of refinement process. However, the refinement process at $T_{rd} = 0.1$ still unable to regularize some complex estimation outliers. So that, an increase of the robustness of the refinement by decreasing $T_{rd} = 0.03$ shows an outlier free estimation fields, Figure 5. 16(e and f). This performance of refinement process shows a significant improvement in its effectiveness against estimation outliers, particularly for small correlation window length of 3λ .

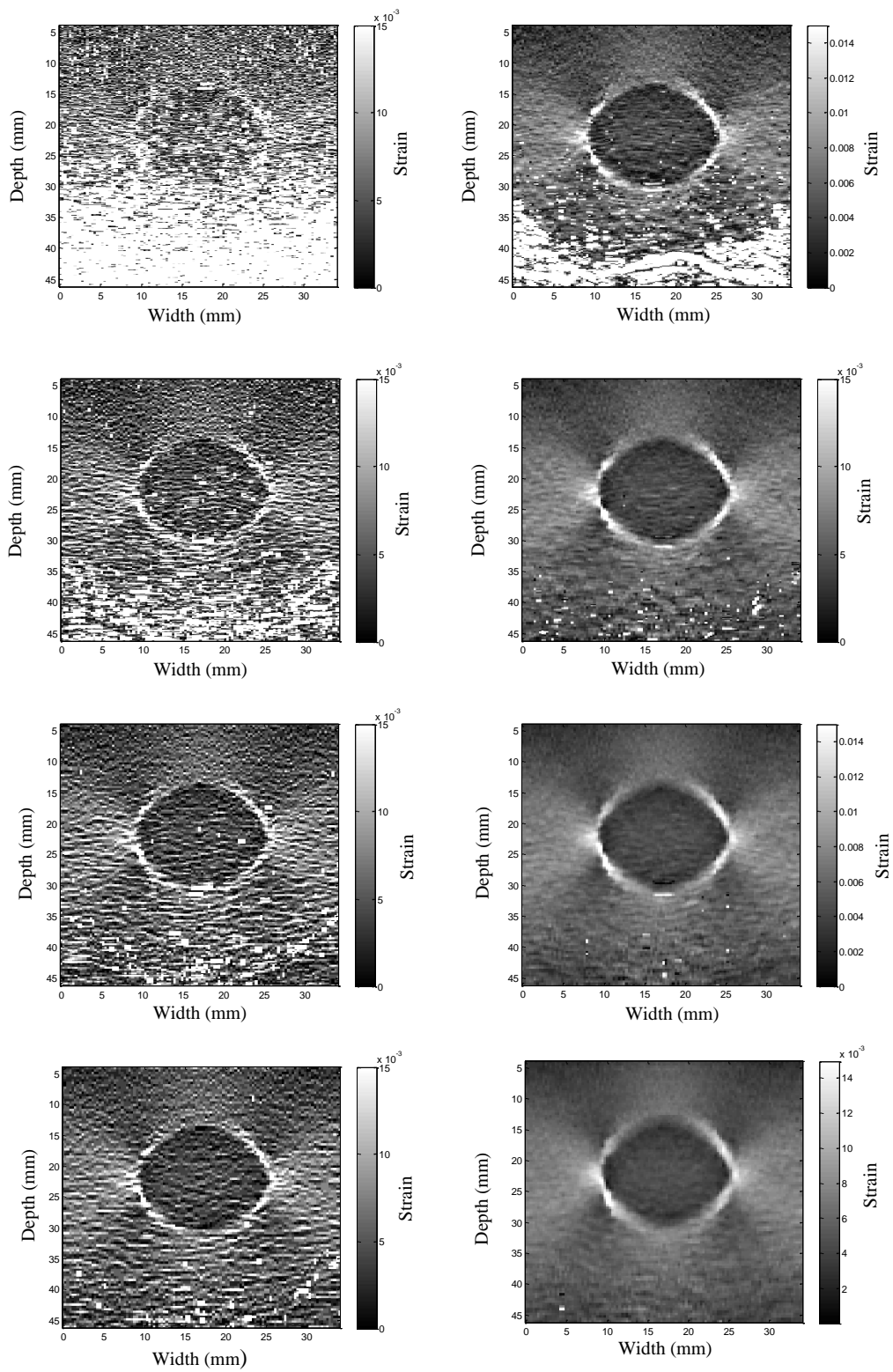


Figure 5.15 Strain field of heterogeneous TMM without (left) and with refinement process (right) of $T_{cd}=4$, 1.4 pre-to-post window length ratio and different correlation window length of 2λ - 5λ from top to bottom.

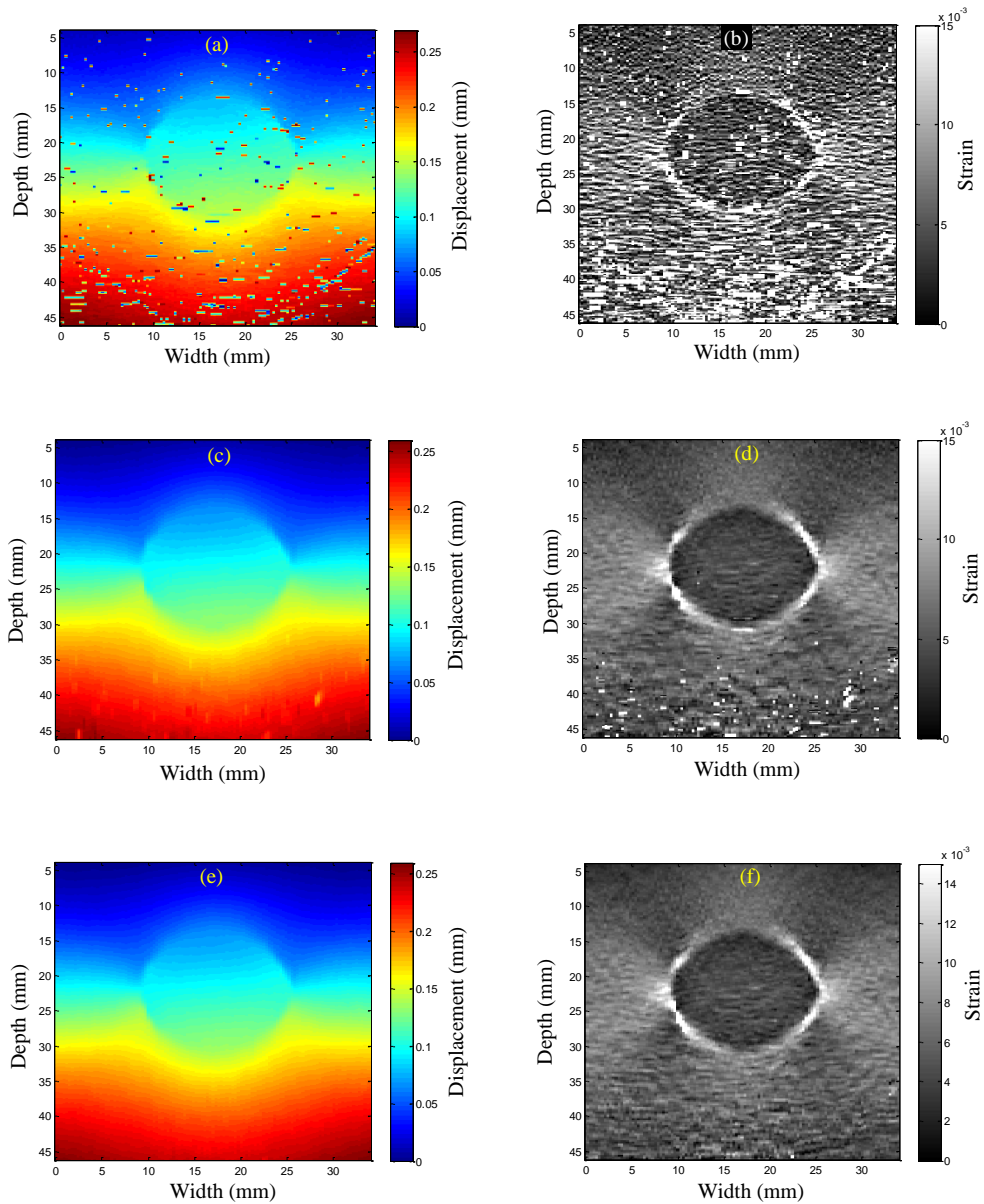


Figure 5.16 (a, c, e) Displacement and (b, d, f) strain fields of heterogeneous TMM for 3λ correlation window length and 1.6 pre-to-post-window length ratio of, (a and b) without refinement process, with refinement process $T_{cd}=4$ (c and d) $T_{rd}=0.1$, and of (e and f) $T_{rd}=0.03$.

5.4.3 Investigation of refinement process for simulation model

In chapter 4, section 4.7.3 the heterogeneous simulation model with applied compression of 1% was presented. Figure 4. 22(a and b) showed that the displacement and strain field were corrupted by estimation outliers at 10λ correlation window length. Figure 4. 22(c and d) was shown a significant increase of estimation outliers at 5λ correlation window length. This section aims to investigate the effectiveness of refinement algorithm to produce qualitative displacement and strain fields at 5λ correlation window length. In addition, the investigation also deals with the ability to reduce the correlation window length to 3λ with acceptable quality of estimation. Figure 5. 17 shows the displacement and strain fields without and with refinement process at 1% compression. The algorithm uses a 5λ correlation window length, 1.4 pre-to-post window length rate, $T_{rd}=0.03$, and $T_{cd}=4$. Figure 5. 17(a and b) shows the displacement and strain fields that corrupted by dispersed estimation outliers. Figure 5. 17(c and d) shows how most of estimation outliers are regularised by refinement process.

For higher spatial resolution of using 3λ correlation window length, the effectiveness refinement algorithm is also tested. Figure 5. 18(a and b) shows the displacement and strain without refinement process for 3λ correlation window length and 1.8 pre-to-post window length ratio. In Figure 5. 18(a), estimation outliers are increased compared to Figure 5. 17(a). Figure 5. 18(b) shows very low quality strain field, which is corrupted by a massive amount of estimation outliers. Figure 5. 18(c and d) shows how the refinement capable to regularize most of the outliers. However, some of outliers exist, particularly at the bottom of the strain field. These some existing estimation outliers can be reduced by slightly increase the pre-to-post window length ratio as shown in Figure 5. 19.

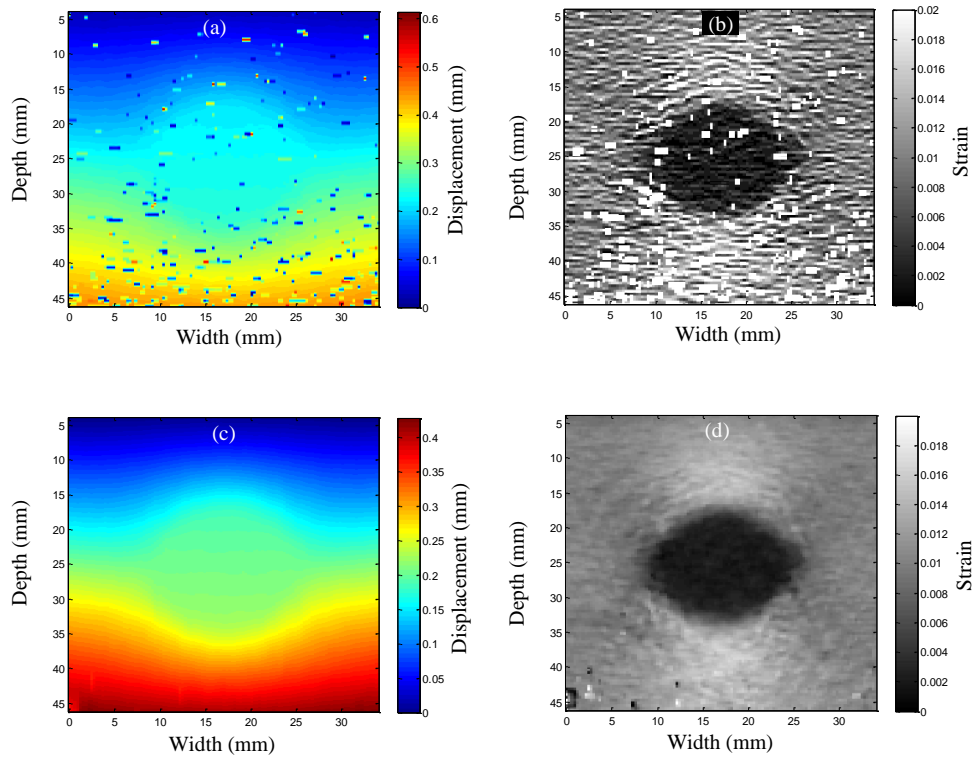


Figure 5. 17 (a, c) Displacement and (b, d) strain fields of heterogeneous simulation model for 1% applied compression, correlation window length, 1.4 pre-to-post window length ratio, (a and b) without refinement process, with refinement process of $T_{rd}=0.03$, $T_{cd}=4$.

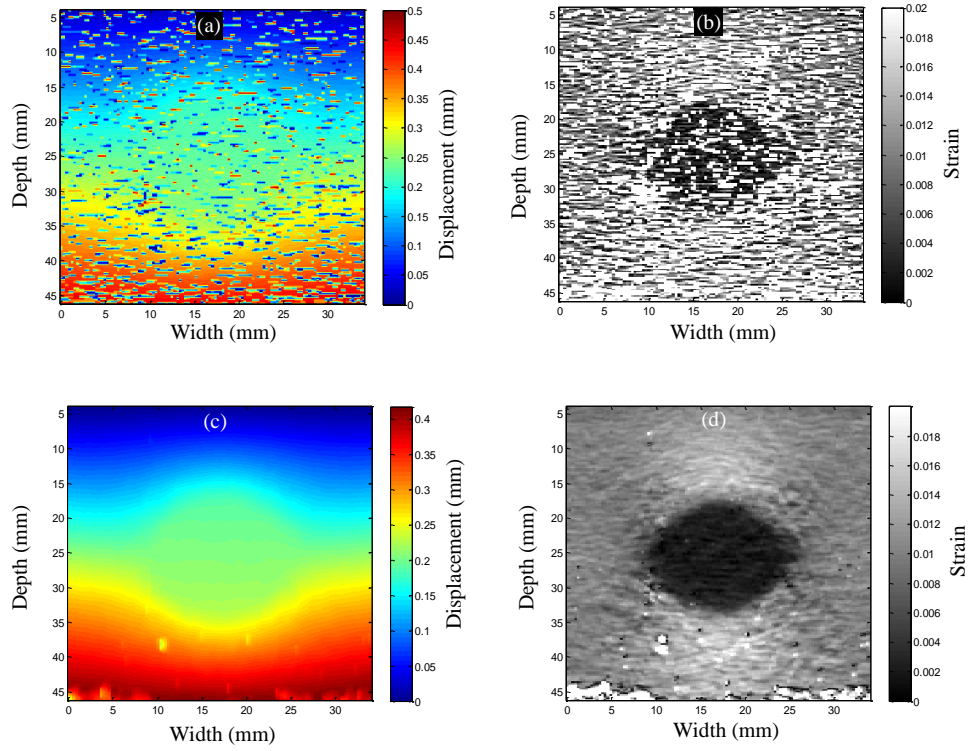


Figure 5. 18 (a and c) Displacement and (b and d) strain fields of heterogeneous simulation model for 1% applied compression, 3λ correlation window length, 1.8 pre-to-post window length ratio, (a and b)without refinement process, with refinement process of $T_{rd}=0.03$, $T_{cd}=4$.

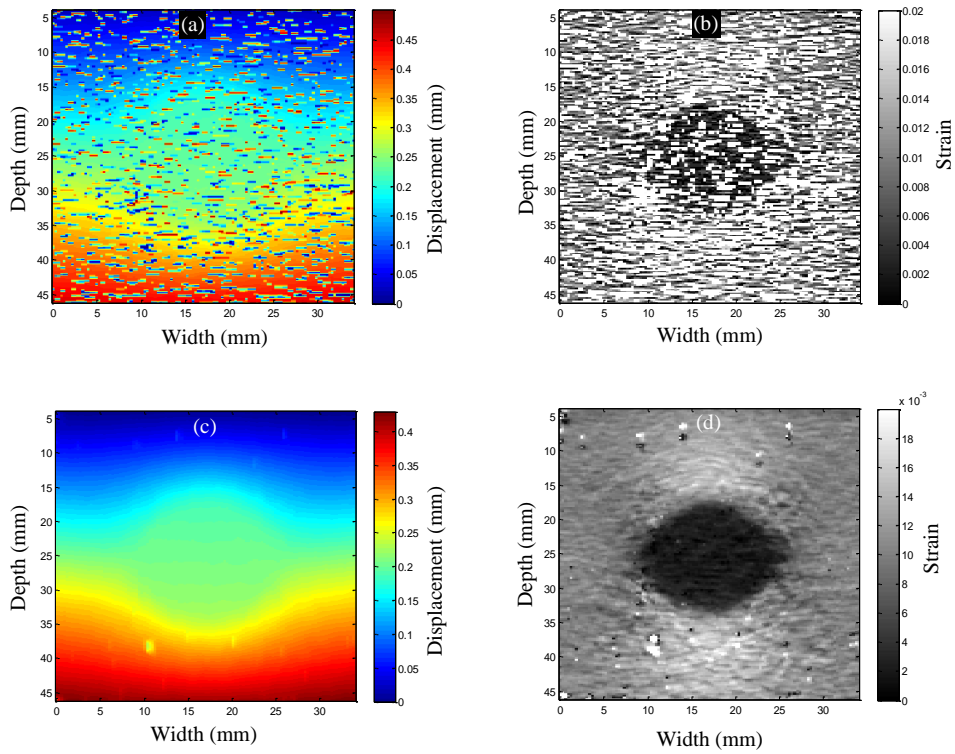


Figure 5. 19 (a and c) Displacement and (b and d) strain fields of heterogeneous simulation model for 1% applied compression. Using 3λ correlation window length, 1.9 pre-to-post window length ratio. (a and b) without refinement process and (c and d) with refinement process of $T_{rd}=0.03$, $T_{cd}=4$.

5.4.4 Performance against 2% compression

In clinic practice, the applied compression cannot be measured, e.g. freehand compression over biological soft tissue, so that it cannot be confined as $\leq 1\%$. Therefore, it is feasible to assess the performance of refinement process in a situation of larger compression than 1%.

Experiment based raw data before compression and after 2% applied compression is acquired. The initial displacement field is estimated using correlation window length of 5λ and pre-to-post window length ratio of 1.4. While, refinement algorithm parameters are $T_{rd}=0.03$ and $T_{cd}=4$.

In Figure 5. 20, the displacement and strain fields of the heterogeneous TMM are shown with and without refinement process. The displacement field of Figure 5. 20(a) shows how the decorrelation noise (estimation outliers) increased at compression of 2% relative to the situation of 1% compression of Figure 5. 12(a), and also at the same time Figure 5. 20(b) shows how the decorrelation noise is amplified due to gradient operation of strain estimation. In above, Figure 5. 16(e and f) showed how the refinement process is successfully used to regularise the estimation outliers, particularly when robust refinement parameters (T_{rd} and T_{cd}) are determined at acceptable spatial resolution (small windows length of 3λ). Here, in the situation of 2% applied compression, Figure 5. 20(c and d) shows an existence of some estimation outliers particularly at the bottom of the object under imaging. The existence of the outliers points out that the refinement process fails to regularise this complex situation. As mentioned earlier in section (3.5), the finite observation would be considered as function of the deformation scale.

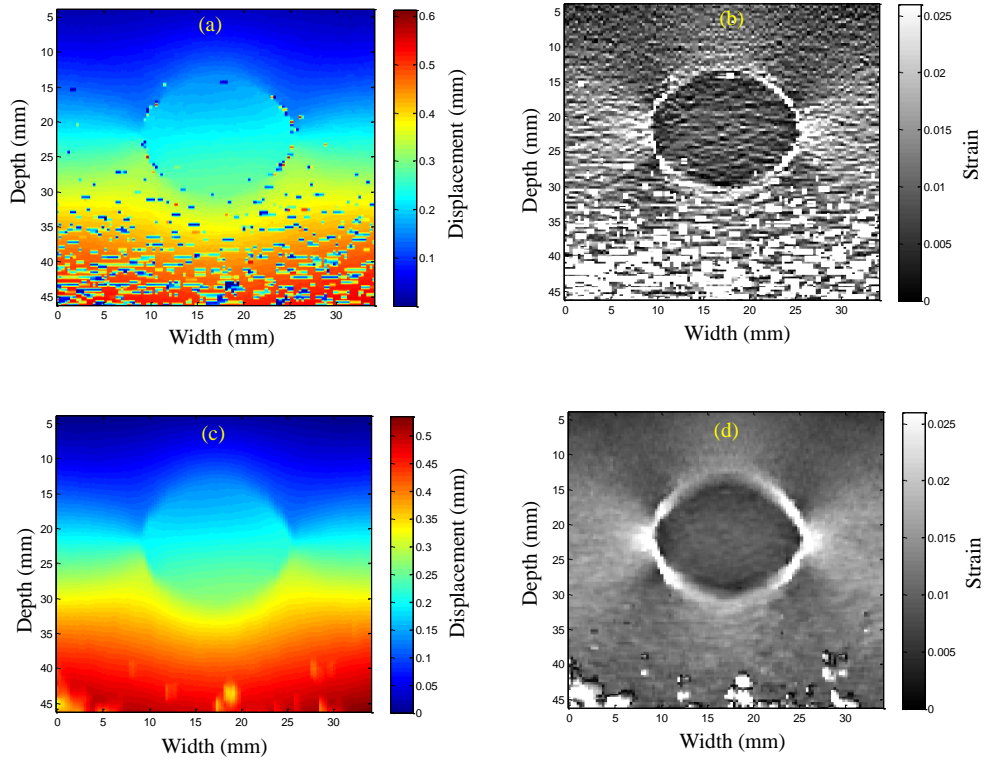


Figure 5. 20 (a, c) Displacement and (b, d) strain fields of heterogeneous TMM for 2% applied compression, 5λ correlation window length, 1.4 pre-to-post window length ratio, (a and b) without refinement process, with refinement process of $T_{rd}=0.03$, $T_{cd}=4$.

In effect, it is possible to enhance the performance of refinement to eliminate the existent estimation outliers by increase the correlation windows length but at the expense of reduction in spatial resolution of strain field. In Figure 5. 21, the correlation window length is increased to 8λ , pre-to-post window length ratio is 1.4. The refinement parameters are $T_{rd}=0.03$ and $T_{cd}=4$, which are similar to the estimation of Figure 5. 20. It is clear that estimation outliers are reduced, Figure 5. 21(a and b). It is also clear, the refinement process improves the displacement and strain fields Figure 5. 21(c and d), but at the same time the strain spatial resolution is decreased, Figure 5. 21(b and d). From that, it is necessarily to upgrade (develop) the algorithm of refinement to be robust enough against increase of estimation outlier due to applying high compression while keeping acceptable spatial resolution.

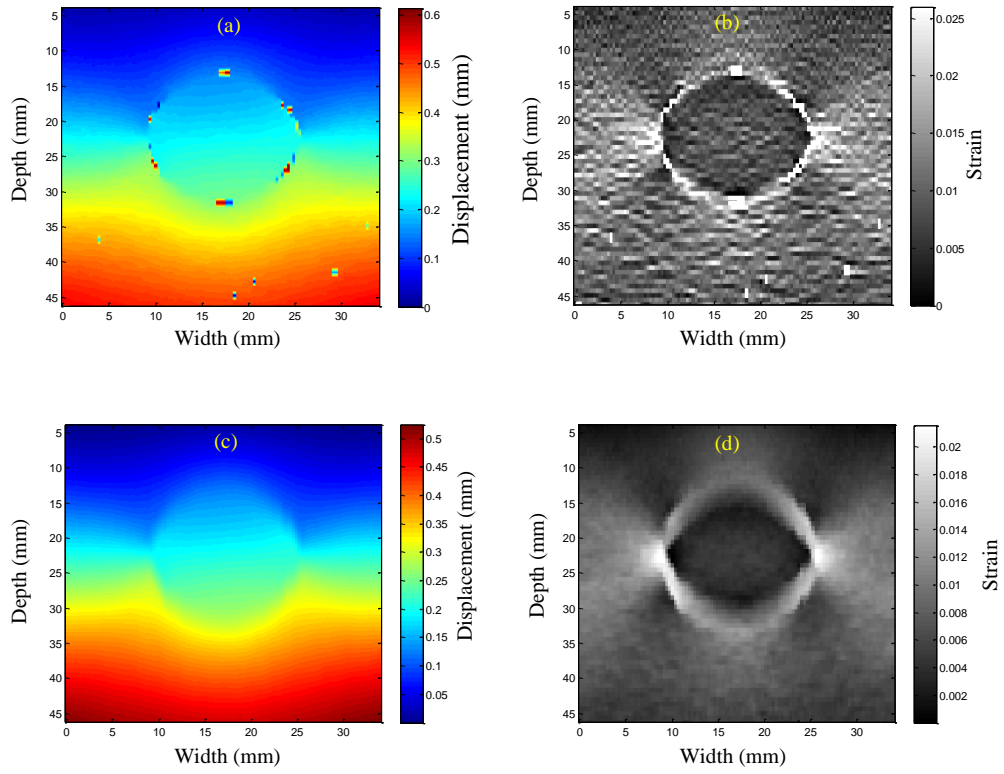


Figure 5. 21 (a, c) Displacement and (b, d) strain fields of heterogeneous TMM for 2% applied compression, 8λ correlation window length, 1.4 pre-to-post window length ratio, (a and b) without refinement process, with refinement process of $T_{rd}=0.03$, $T_{cd}=4$.

5.5 Conclusion

Pre-and post-compression raw data acquired using DYNARAY ultrasonic Phased Array Controller for homogeneous and heterogeneous TMM under uniform compression has been used to test a newly proposed refinement algorithm for strain field mapping. Initial displacement field has been estimated using cross-correlation for a certain small window length. A refinement process has been proposed to eliminate displacement estimation outliers due to non-uniform scatterer motion. The proposed process effectively improves strain quality. Algorithm parameters have been adjusted empirically to produce distinct estimation of displacement and strain fields at small correlation window length. Results compare favourably for estimation process compared to those without the refinement process.

The robustness of refinement process degrades beyond 2% applied compression, particularly at small correlation window length. The robustness of refinement process will be improved in the next chapter for the complex situation of large-scale compression and freehand compression.

Chapter 6

Large Scale Compression and Freehand Compression

6.1 Introduction

The performance of the novel refinement algorithm was investigated in section 5.4.4 for 2% applied compression. The results indicated a degradation when using small correlation window length of order 5λ . However, the investigation indicated that an increase in correlation window length for an order of 8λ improves the performance, at the expense of poorer spatial resolution.

The main contribution of this chapter is to present an advanced version of the refinement algorithm that incorporates an elimination of non-consistent cells from neighbour set before median operation. This advanced refinement algorithm will be able to produce qualitative strain mapping with acceptable spatial resolution for large-scale applied compression (up to 4%) and freehand compression of experiment scenario.

The remainder of the chapter is organized as follows. The refinement algorithm is presented in the form of mathematical and diagrammatic models in Section 6.2. Experimental materials and settings are described in section 6.3. Comparative results and discussion are included in Section 6.4.

6.2 Estimation of Displacement and Strain

The initial displacement field is estimated as described in section 5.2. The proposed adjustment of correlation windows length is different in this chapter to that described in Chapter 5. The correlation window length and the pre-to-post window length ratio (initial displacement estimation parameters) are adjusted optimally based on the histogram of correlation coefficients. The histogram is considered as a reliable indicator, which can measure the reliability of the initial displacement estimation parameters.

The estimation method in Figure 5. 1 is considered in this chapter, where initial displacement field is determined as described in Table 6.1. Then, strain field is estimated using LSQSE (section 3.4.2). A quantitative comparison is determined for non-refined, median filtered and refined strain estimations, using SNR for homogeneous strain field and CNR for heterogeneous strain field.

Table 6.1 Estimation of initial displacement

1. Load RF data region of interest (2D matrix) of before and after compression.
2. Apply cross-correlation operation (3.6) using post-compression window length of at least 5λ , and pre -to-post window length ratio of at least 1.4.
3. Perform a spline interpolation for the correlation function to differentiate the sub-sample delays.
4. Update the RF-data for next correlation windows and then repeat steps (2 and 3) to generate the initial displacement vector.
5. Update the RF-data for next A-scan to generate initial displacement field.
6. Plot the histogram of correlation coefficients. Change the correlation windows length in an empirical way (visual observation of the histogram) until it become Gaussian or nearly Gaussian.

6.2.1 Difficulties into refinement operation

A 2D median filter was used to remove impulsive noise (salt and paper), while relatively preserves the image spatial content [115]. The 2D median filter was also used to eliminate noise that occupies a block of pixels once the noise block size is less than a half of the filter dimension [119], Figure 6. 1(a-d). However, the 2D median filter operates in an unsupervised way without taking into consideration whether its needed or not Figure 6. 1(d). Hence, to regularize the displacement estimation outliers, the refinement process described in section 5.2.3 was developed to regularize the initially estimated displacement. In this approach a 2D regularization operation was used in an adaptive way. The benefit of the proposed method over the standard 2D median filter is accomplished by performing the process for only the inconsistent measurements, which will reduce the number of sorting operation (reduces time consumption) and also at the same time preserves the spatial content.

Figure 6. 1 describes how both of 3x3 median filter and refinement process are performed on noise block. In Figure 6. 1(a-b) median filter shows an effective operation to regularize the non-consistent CUI estimation. While it fails to regularize non-consistent CUI estimation Figure 6. 1(c), and to keep consistent CUI estimation Figure 6. 1(d) at complex noise block situation. In Figure 6. 1(e-g) refinement process shows an ability to regularize non-consistent CUI estimation and keep consistent CUI estimation at different complex noise block situations. However, the regularization of refinement process fails at some specific setting parameters, Figure 6. 1(h). This situation is similar to what has been shown before in Figure 5. 20, where refinement performance degraded at compression more than 1%.

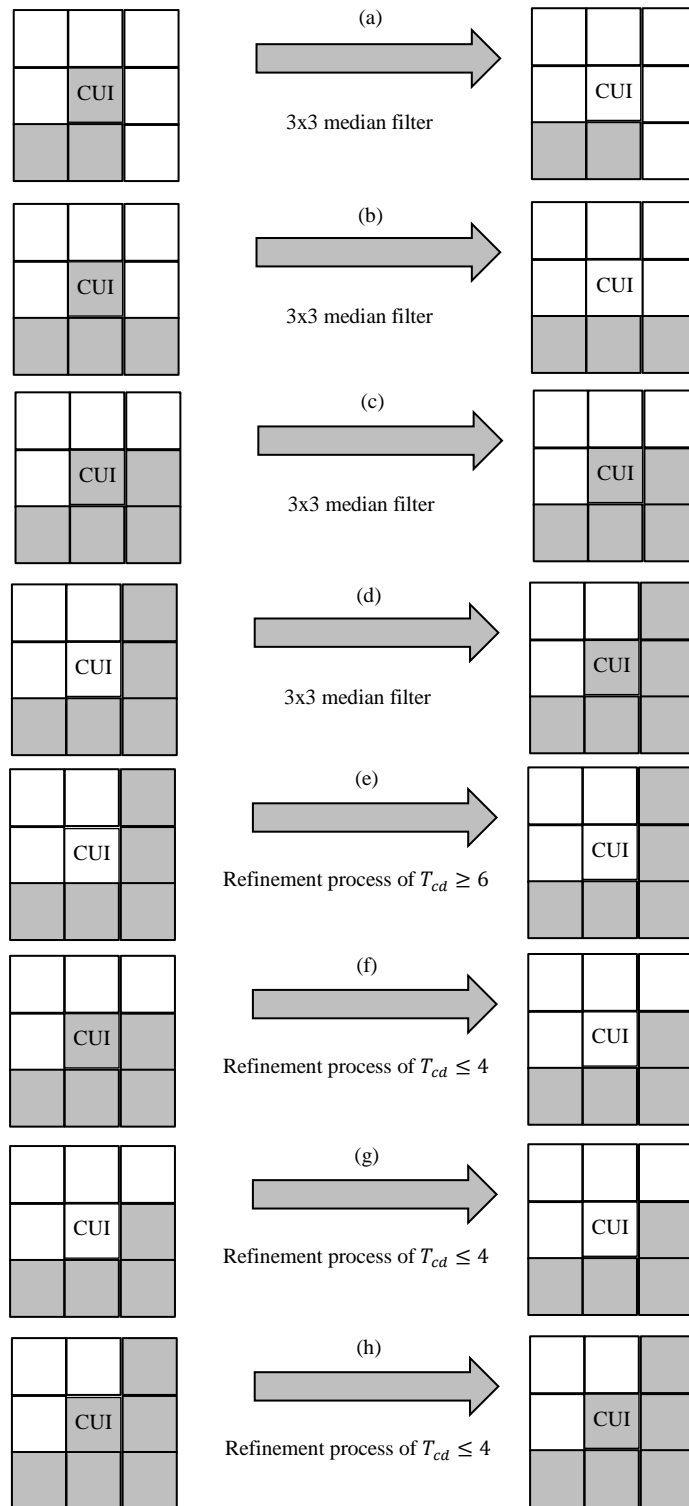


Figure 6. 1 Noise block occupations and, (a-d) median filter operation for 3x3 dimensions, (e-h) refinement operation.

6.2.2 Exclusion of Estimation Outliers

An advance refinement process is achieved by increasing the robustness of the recalculation of inconsistent estimation. The eight neighbours' measurements are reconstructed by exclusion of estimation outliers. The exclusion is performed based on comparison operation shown in Figure 6. 2.

The recalculation process begins by sorting the eight neighbours' measurements as in (6.1). A normalized comparison vector of lower and upper rank is computed as in (6.2) and (6.3) respectively.

$$d_{SN_1} \leq d_{SN_2} \leq \dots \leq d_{SN_8} \quad (6.1)$$

$$NLC_j = \frac{|d_{SN_j} - d_{SN_{j-1}}|}{\max(d_{SN_j}, d_{SN_{j-1}})} \quad (6.2)$$

$$NUC_j = \frac{|d_{SN_j} - d_{SN_{j+1}}|}{\max(d_{SN_j}, d_{SN_{j+1}})} \quad (6.3)$$

where, NLC_j and NUC_j are the normalized lower comparison vector and upper comparison vector, d_{SN_j} is a sorted displacement neighbour of rank j ($j = 2, 3 \dots 7$).

A comparison process is carried out by comparing the normalized comparison vectors of NLC_j and NUC_j to a certain threshold of T_{cc} (6.4) to produce a consistency classifier Figure 6. 2.

$$\left. \begin{array}{l} NLC_j > T_{cc} \quad \text{then } CLP = 1 \\ NLC_j \leq T_{cc} \quad \text{then } CLP = 0 \end{array} \right\} \quad (6.4)$$

$$\left. \begin{array}{l} NUC_j > T_{cc} \quad \text{then } CUP = 1 \\ NUC_j \leq T_{cc} \quad \text{then } CUP = 0 \end{array} \right\}$$

$$d_{SN_{j+1}} = \emptyset \quad \left. \begin{array}{l} \text{if } j = 7 \text{ and either } CLP = 1 \text{ and } CUP = 1 \\ \text{, or } CLP = 0 \text{ and } CUP = 1 \end{array} \right\} \quad (6.7)$$

where \emptyset is a symbol of empty set that refers to the exclusion.

Every surviving d_{SN_j} is re-grouped into a vector of d_{NS} which is then utilized to recalculate the d_{CUI} by median operation.

$$d_{CUI} = \text{median} [d_{NS}] \quad (6.8)$$

where d_{NS} is the vector of neighbours that have been survived.

Each axial refined displacement line is interpolated linearly and then averaged using moving average window to smooth out any drift in estimation that would be a source of noise in strain field [3]. Finally, all axial lines are processed in a similar fashion to refine the whole initial displacement field. The procedure to regularize the estimation outliers is described in Table 6.2.

Table 6.2 Refinement process with recalculation of inconsistent estimation

1. Load 2D matrix of initial displacement field, which is determined based on the procedure illustrated in Table 6.1. Then, label each cell and its surrounding eight neighbours, Figure 5. 6.
2. Perform the comparison process using (5.1), to generate the normalized comparison vector.
3. Convert the normalized comparison vector into binary comparison vector using (5.2-5.4).
4. Perform consistency decision process based Bernoulli Trail using (5.5 and 5.6).
5. If the displacement measurement of CUI is considered as inconsistent, sort the displacement measurements of the eight neighbours (6.1).
6. Determine the NLC_j and NUC_j using (6.2) and (6.3) respectively.
7. Classify the neighbour estimates using (6.4).
8. Exclude the inconsistent measurements using (6.5-6.7).
9. Change the inconsistent displacement measurement of CUI by the median value of the survival neighbours' measurements (6.8).
10. Apply smoothing process for each refined vector.
11. Update the new displacement vector, then repeat steps (2-10).
12. Optimize the refinement parameters of T_{rd} , T_{cd} and T_{cc} to regularize any residual displacement estimation outliers. The optimization process is considered in a conjunction of reducing the correlation window length by visual observation of refined displacement field.

6.3 Materials

Ultrasound raw data is acquired using the same ultrasound system used in Section 5.3. In this experiment, two different scenarios of compression are performed. One is similar to compression method in Section 5.3.3 with increasing the compression scale of 2%, 3%, and 4%, as shown in Figure 6. 3(a). While the other is freehand compression that uses compression plate Figure 6. 3(b) and transducer physical surface Figure 6. 3(c).

For uniform compression the XYZ scanner arm holds the transducer-plate adaptor while applying compression Figure 6. 3(a). Whereas for the freehand compression, an operator holds the transducer-plate adaptor/transducer itself by his hand while applying compression Figure 6. 3(b-c). The phased array linear scanning is performed for both transducer probes of 10MHz and 5MHz where the setting parameters are illustrated in Table 6.3. Tens frames are acquired sequentially during the freehand compression, some of them are processed in this research, while others are stored for further investigations.

Table 6.3 Setting parameters of DYNARY imaging system

Operating frequency (MHz)	Number of total elements	Number of active elements	Sampling frequency (MHz)	Pitch (mm)	Frame rate (Frame/sec)
10	128	16	100	0.3	-
5	128	16	100	0.7	2

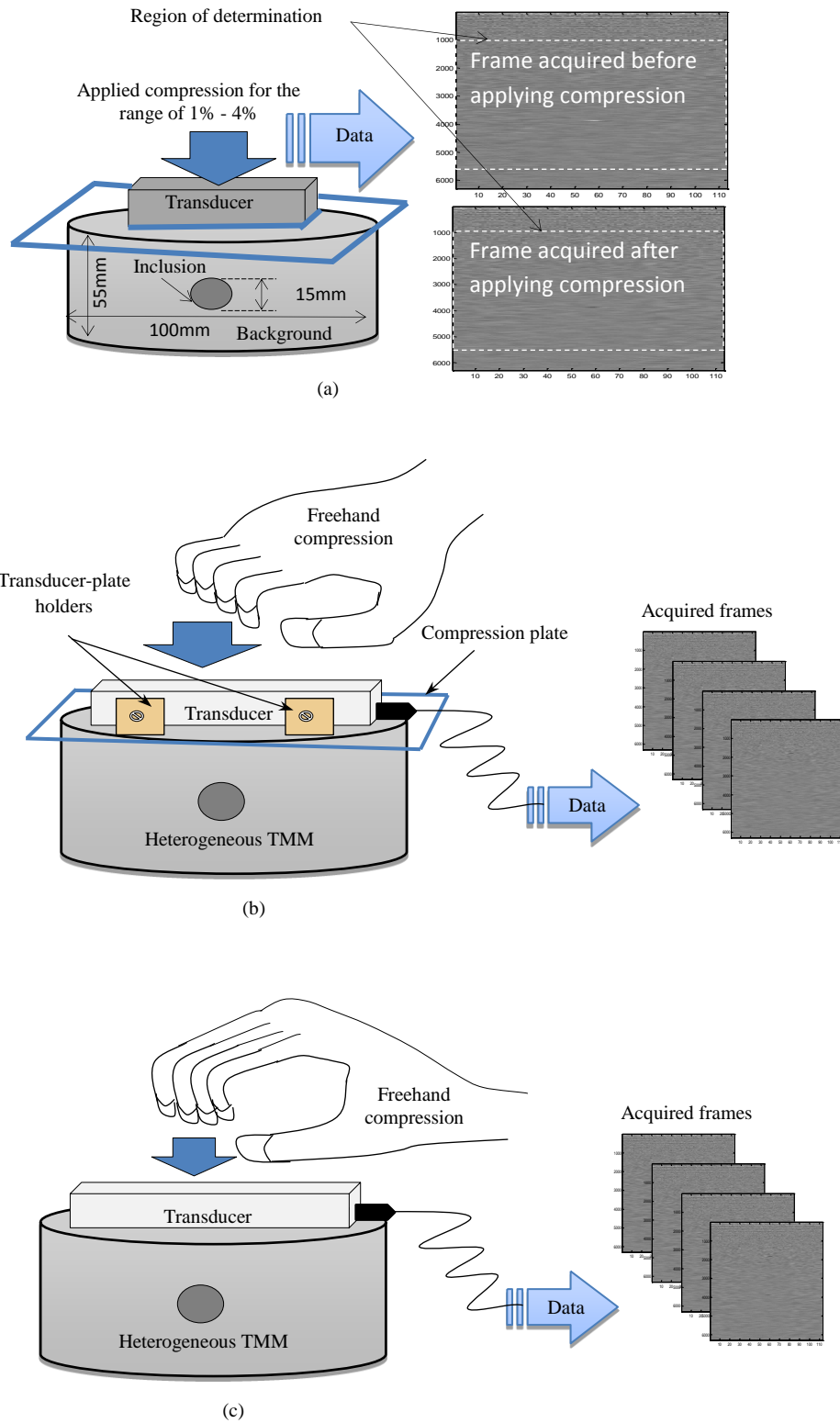


Figure 6. 3 Heterogeneous TMM under compression scenarios are performed using (a) uniform compressions, (b) freehand with transducer-plate adaptor and (c) freehand with transducer only.

6.4 Results and Discussion

This section investigates the relative performance of the refinement in comparison to median filter (applied to the initial displacement field) in terms of visual and quantitative measures. The investigation aims to assess refinement process by addressing its robustness against complex situations of large-scale of uniform compression for up to 4% and freehand compression. The median filter used is 3x3 dimension that is applied to regularize the initial displacement field. The investigation also includes, initial displacement estimation parameters of correlation window length and window overlap, and refinement process parameters of T_{rd} , T_{cd} , and T_{cc} . The optimal parameters are considered to illustrate the effectiveness of refinement process. Generally, the refinement process enhances the displacement field by reducing the standard deviation that would ultimately reduce the noise over the strain field.

6.4.1 Visual and quantitative comparison

For 1% axially applied compression, both homogeneous and heterogeneous TMM models are utilized for the comparison of non-refinement, 3x3 median filter, and refinement processes. In visual comparison, displacement and strain fields are illustrated. While in quantitative comparison, SNR is determined for homogeneous model, and CNR is determined for heterogeneous model.

A. Visual comparison for homogeneous model:

In Figure 6. 4, the images in the left column are the displacement fields and on the right column are the strain fields. The initial displacement field parameters are 3λ correlation window length, 1.6 pre-to-post window length ratio, and 50% sequential windows overlap. Refinement parameters are $T_{cd}=4$, $T_{rd}=0.003$, and $T_{cc}=0.04$. The first row of Figure 6. 4(a-b) represents non-refinement estimation, while the second row Figure 6. 4(c-d) represents 3x3 median filter estimation, and the last row Figure 6.

4(e-f) represents refinement estimation. The yellow squares regions in the images will be used for SNR estimation.

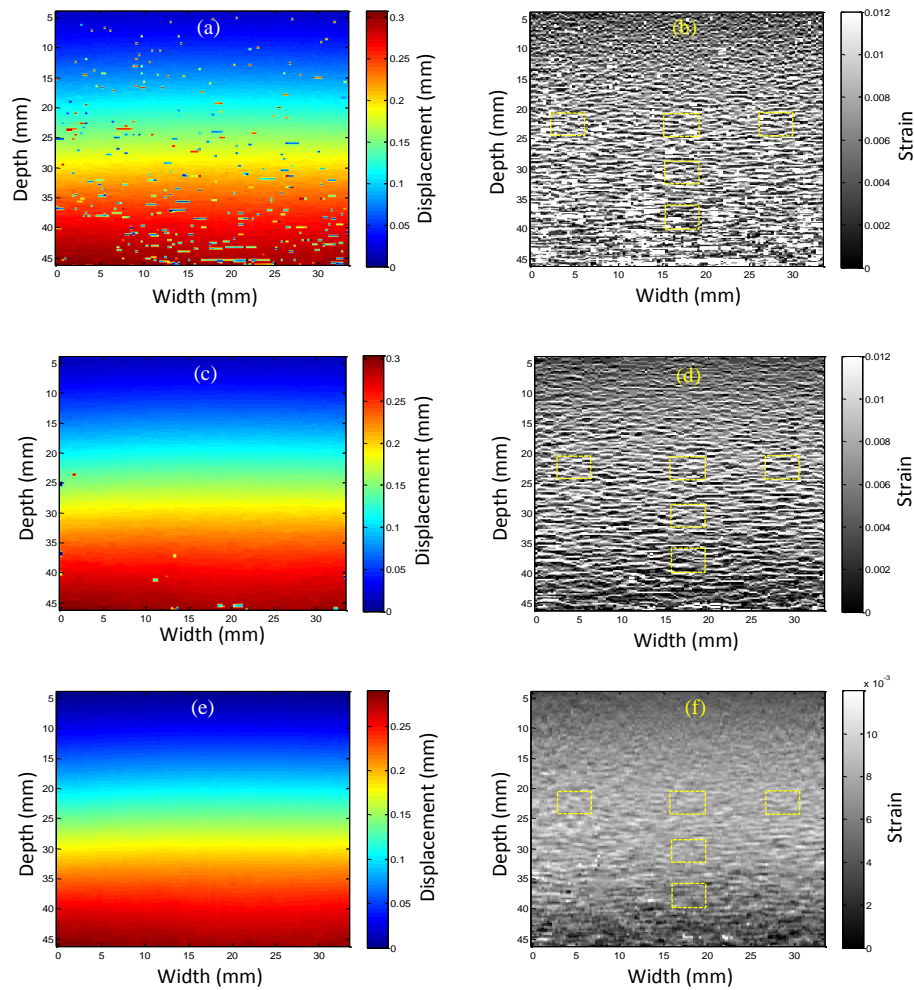


Figure 6. 4 (a,c,e) Displacement and (b,d,f) strain (right column) fields of homogeneous TMM (a and b) without refinement, (c and d) median filter and (e and f) with refinement processes.

Figure 6. 4(a) shows the initial displacement field that contains displacement estimation outliers. These outliers depict an incorrect estimation of displacement due to losses in correlation between pre-compression and post-compression windows. It is also clear how these estimation outliers have a significant impact in producing a low qualitative strain field as shown in Figure 6. 4(b). In Figure 6. 4(c), it is seen that the 3x3 median filter process is able to remove these outliers, but the displacement field is not well aligned and includes some outliers. The correspondent strain field is

shown in Figure 6. 4(d) where the strain field is noisy (mixed of outliers and warm noise). Figure 6. 4(e) shows a superiority of refinement process to produce outliers free displacement field, which is well aligned in terms of smooth gradient displacement. The smooth gradient displacement field significantly enhances the strain estimation as shown in Figure 6. 4(f).

The robustness of the refinement process against estimation outliers is reinforced with optimal cross-correlation parameters. The effectiveness of optimal correlation windows length and refinement process is achieved by providing acceptable spatial resolution and outlier free estimation, as shown in Figure 6. 5. Figure 6. 5(a and b) represents the histogram of correlation coefficients, while Figure 6. 5(c and d) represents the correlation coefficients map, and also Figure 6. 5(e and f) represents the initial displacement field. Figure 6. 5(a,c,e) results for equally correlation windows length of 3λ , while Figure 6. 5(b,d,f) are determined for correlation window length of 3λ and pre-to-post window length ratio of 1.6. Figure 6. 5(a and b) shows how the histogram moves from non-Gaussian Figure 6. 5(a) to Gaussian histogram Figure 6. 5(b). The correlation is improved in some area of the histogram particularly those are with coefficients less than 0.7. Comparing Figure 6. 5(a) and Figure 6. 5(b), it is noticed that the number of occurrences of correlation coefficients of less than 0.7 are significantly reduced. This is clearly seen in correlation coefficient map of Figure 6. 5(c and d), where correlation coefficients are increased particularly for those are located at half bottom (depth of 25mm to 46mm). The improvement in correlation is effectively reduces the rate of outlier occurrence at the mentioned depth range, Figure 6. 5(e and f). On the other hand, the histogram indicates a reduction in the area of coefficients of greater than 0.9, Figure 6. 5(a and b). Particularly for estimates located in the depth range 4mm to 15 mm, Figure 6. 5(c and d). This reduction slightly increases the rate of estimation outlier in that depth range , Figure 6. 5(e and f).

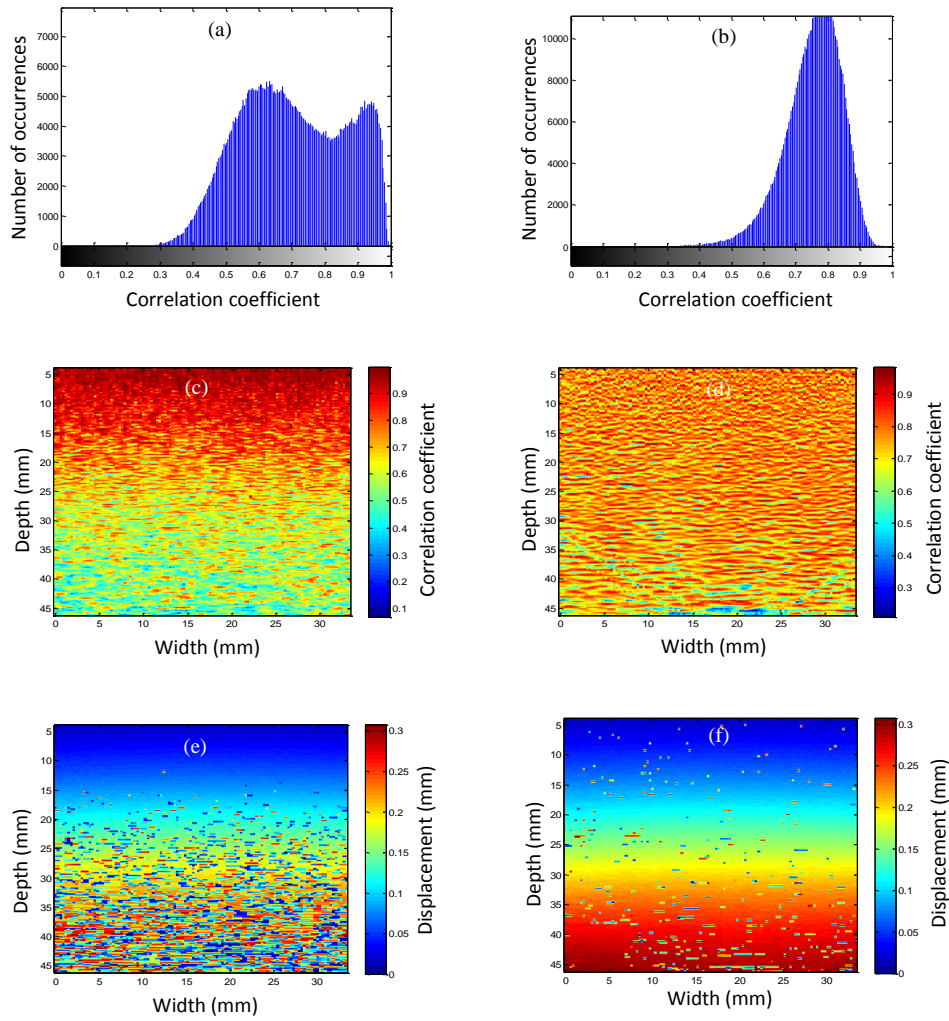


Figure 6. 5 Histogram of correlation coefficients (a) at 3λ of equal correlation windows length and (b) at 3λ correlation window length and 1.6 pre-to-post window length ratio (c and d) correlation coefficient map, and (e and f) displacement field.

B. Quantitative comparison for homogeneous model:

The SNR is a common figure of merit for noise quantitative measurement, which is determined for the strain regions of interest using (5.8). Three regions of interest are located horizontally in the strain fields of Figure 6. 4(b, d, and f). The dimension of each region is 400 axial pixels and 10 lateral lines, and the SNR is determined for nine independent measurements. In Figure 6. 6, the measurements are determined as for the range correlation window length 3λ - 10λ . The pre-to-post window length ratio is considered as 1.2 in Figure 6. 6(a,b,c), 1.4 in Figure 6. 6(d,e,f), and 1.6 in Figure 6. 6(g,h,i).

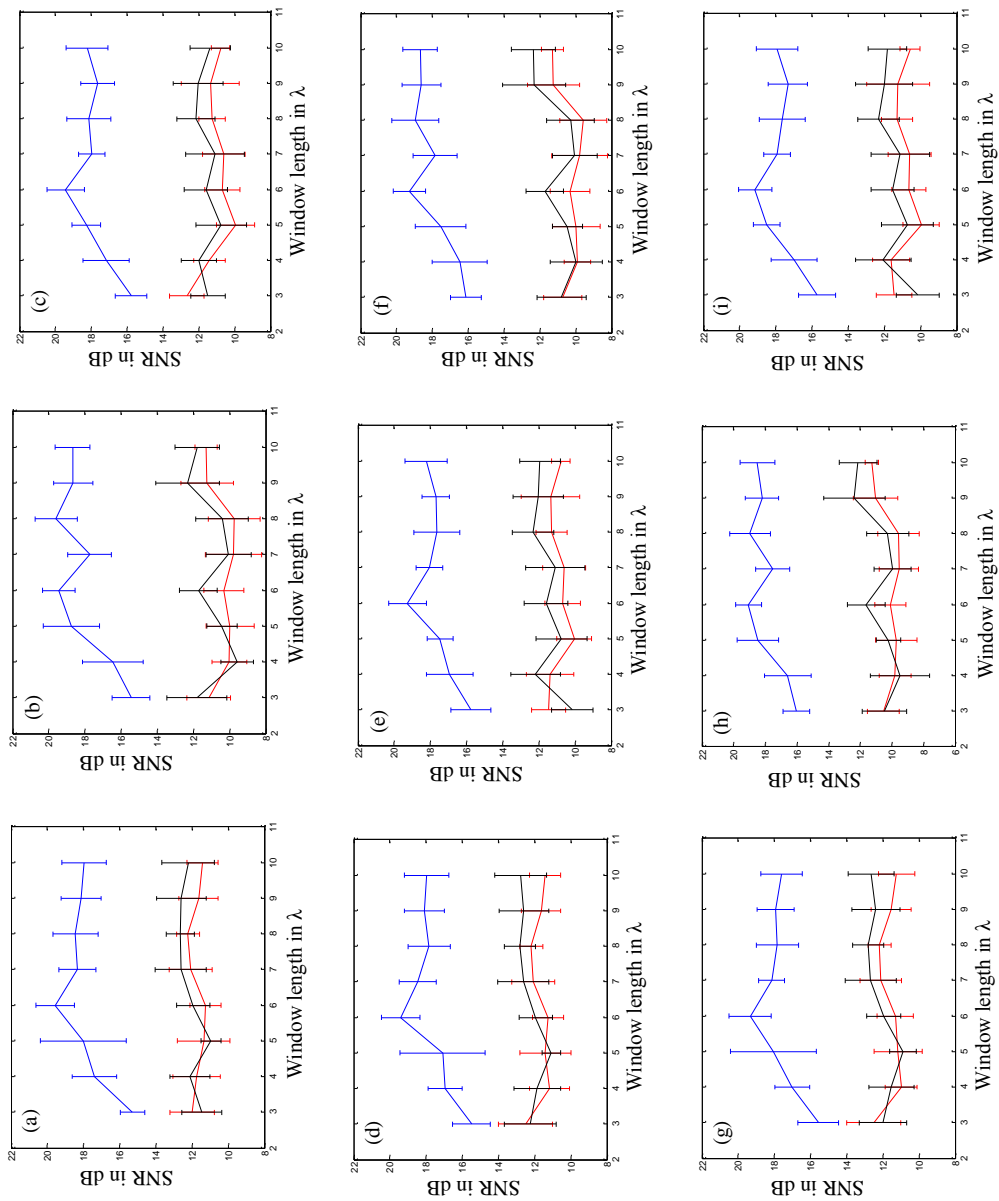


Figure 6. 6 SNR as a function of correlation window length for non-refinement (red line), median filter (black line), and refinement (blue line) processes.

The measurements of SNR in Figure 6. 6 reveal the effectiveness of refinement process over the median filter and non-refinement. The effectiveness is noticed from the distinctive SNR that is higher for the range of 3dB-7dB. It is clear that long enough correlation window length is effective in the improvement of SNR.

Although Figure 6. 4(c) shows the ability of the median filter process to remove the outliers in some regions, but SNR measurements show slightly improvement relative to non-refinement process. This is due to the lack of smoothing in median filter process and at the same time incapability to regularize some complex outliers.

Further measurements of SNR are determined to assess the effectiveness of refinement process in terms of different depth regions of interest. The SNR is measured for other three regions located vertically as highlighted in Figure 6. 4(b, d, and f). In Figure 6. 7, the SNR is determined in the same way as in Figure 6. 6.

As expected, the refinement process is superior compared to the other two processes in terms of higher SNR. In particular, the refinement performance yields lower SNR for deeper region of interest, Figure 6. 7(c, f, and i). In these figures, the SNR collapses at 3λ correlation window length and length rate of 1.2, Figure 6. 7(c). The collapse is restored as far as correlation window length increased for greater than 3λ Figure 6. 7(c), and also as far as length rate increased to 1.4 and 1.6 Figure 6. 7(f and i). In Figure 6. 7, it is noticed that the median filter process exhibits low performance, where the SNR is slightly improved relative to non-refinement process even when window length/length rate are increased.

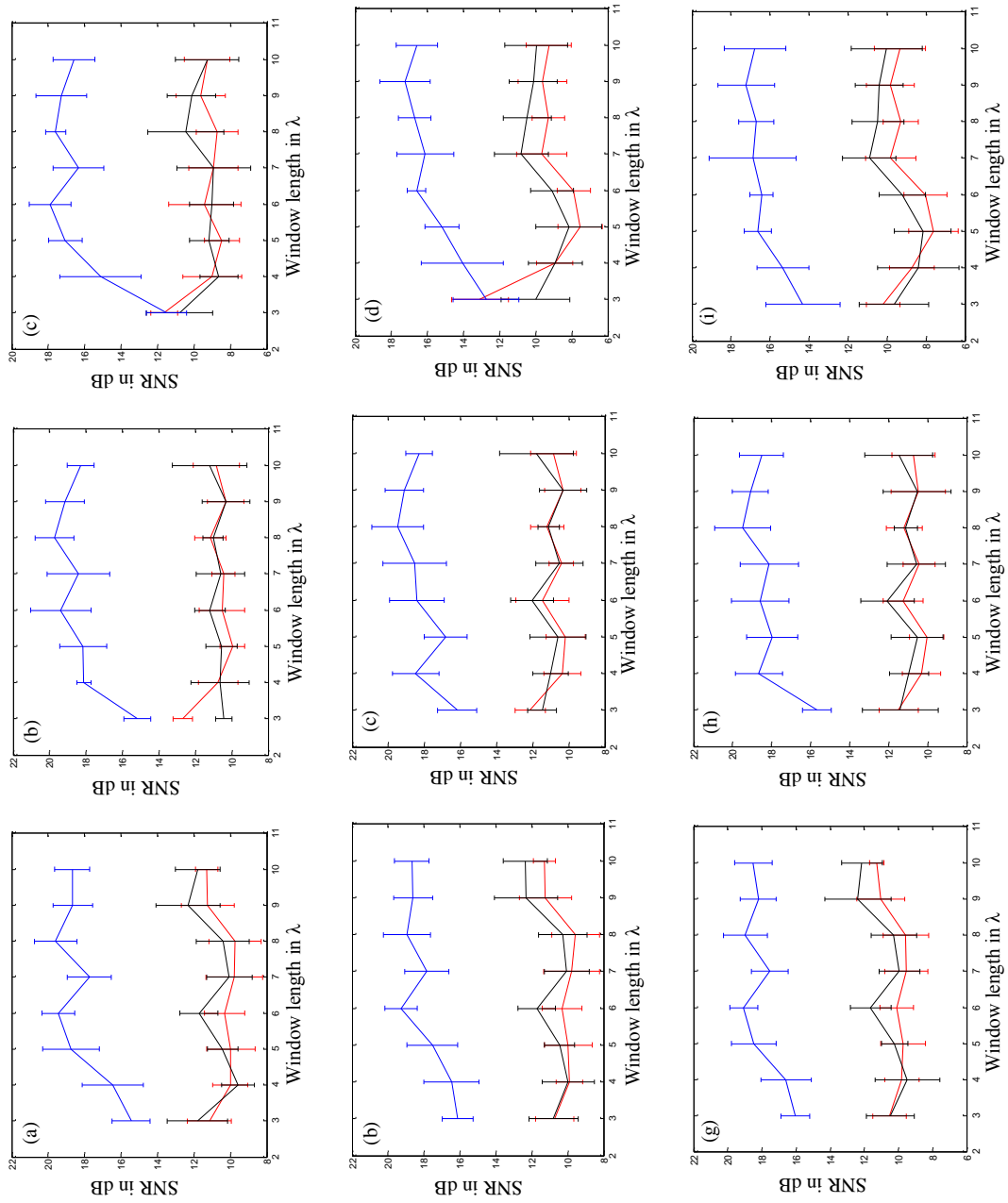


Figure 6.7 SNR as a function of correlation window length for non-refinement (red line), median filter (black line), and refinement (blue line) processes.

C. Visual comparison for heterogeneous model:

In Figure 6. 8, the images in the left column are the displacement fields and on the right column are the strain fields. Displacement and strain fields in the first row are produced by non-refinement process, while in the second row by 3x3 median filter process, and in the last column by refinement process. The initial displacement field (non-refinement process) is estimated for 3λ correlation window length, 1.4 window length ratio, and sequential windows are in overlap of 50%. The refinement process parameters are $T_{cd}=4$, $T_{rd}=0.03$, and $T_{cc}=0.04$.

In non-refinement process, estimation outliers are clearly seen to be dispersed over displacement field Figure 6. 8(a), particularly at deep regions. These displacement outliers significantly corrupt the strain field Figure 6. 8(b), due to a large disparity in displacement values within the regression space. Figure 6. 8(c) shows how the median filter process removes the estimation outliers except complex ones, so that the strain field Figure 6. 8(d) corrupted by estimation outliers and worm noise. The worm noise in the strain field appears as a result of disparity within the operation of regression space. The disparity needs to be aligned by including a smoothing operation within the outlier regulation process.

This need is already addressed in the design of refinement process and its effectiveness has shown on producing a smooth displacement field of Figure 6. 8(e). The effectiveness is accomplished by producing a low noise strain field shown Figure 6. 8(f).

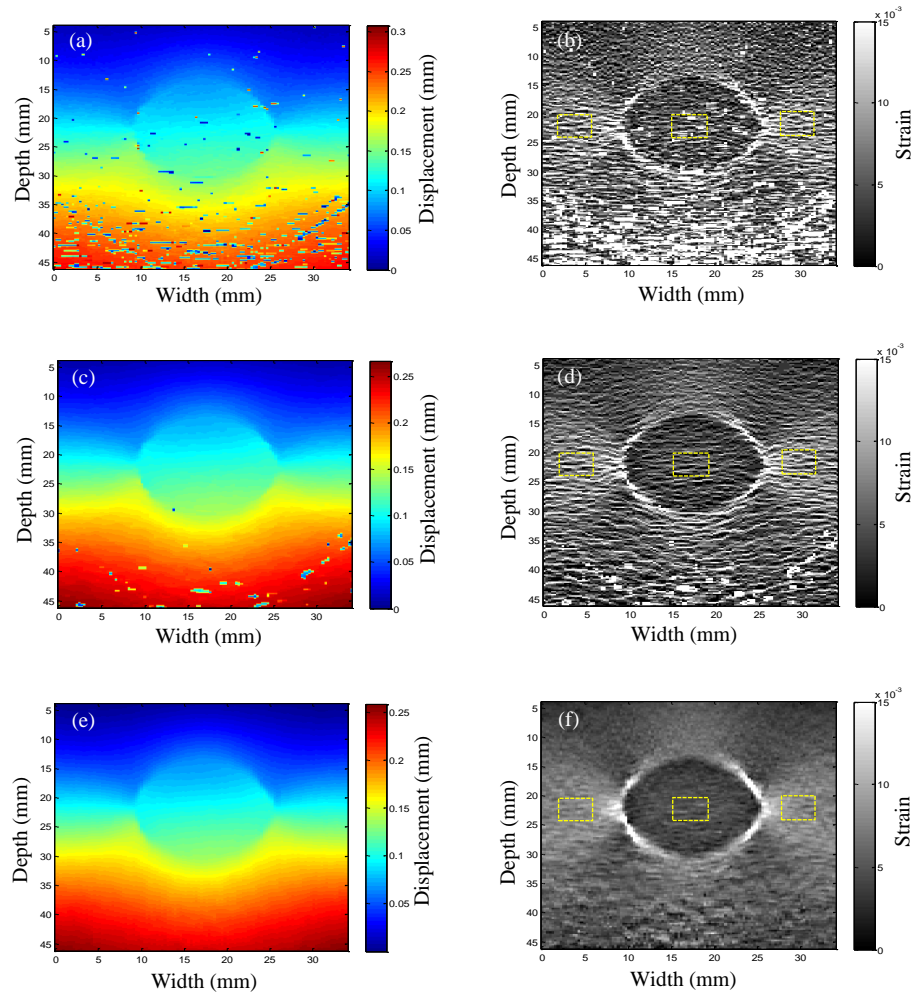


Figure 6. 8 (a,c,e) Displacement and (b,d,f) strain fields of heterogeneous TMM, (a and b) without refinement, (c and d) median filter and (e and f) with refinement processes.

D. Quantitative comparison for heterogeneous model:

A quantitative measurement of heterogeneous TMM is determined in terms of CNR figure of merit. The effectiveness of the refinement process is determined relative to the non-refinement and 3x3 median filter processes based on CNR improvement. The CNR is determined for two strain regions of interest that have been highlighted in Figure 6. 8(b,d,f), the inclusion region of interest is considered relative to each of the two regions in the background (left and right).

The CNR is determined as a function of correlation window length of the range 3λ - 10λ . Different pre-to-post window length ratios are considered as, 1.2 in Figure 6. 9(a and b), 1.4 in Figure 6. 9(c and d), and 1.6 in Figure 6. 9(e and f). The refinement process parameters are $T_{cd}=4$, $T_{rd}=0.03$ and $T_{cc}=0.04$. The CNR illustrates a good correlation between the two regions of interest of in the left and on the right of the inclusion, as shown in Figure 6. 9(a, c, and e) and Figure 6. 9(b, d, and f) respectively.

A coincidence in the CNR of the two regions of interest (left and right) exhibits a statistical significance. Figure 6. 9 shows a superiority of strain CNR of refinement process relative to the other two processes. The difference in CNR of refinement process relative to the non-refinement process is approximately 8dB. The same difference is established relative to median filter process, except for correlation window length of 3λ where the difference is up to 4dB. At the same time, CNR of median filter process does not show a significantly improvement relative to the non-refinement except at 3λ and 4λ window length for up to 4dB.

Generally, the CNRs of refinement process are increased for range of 3dB-5dB, while of non-refinement process are increased for range of 2dB-4dB at window lengths $\geq 5\lambda$. The change in length rate from 1.2-1.6 does not show significant improvement in CNR Figure 6. 9, this is exactly the same as in SNR of Figure 6. 6, which was determined for similar background region of interest. This situation points out that the increase in length rate (1.2-1.6) is effective for refinement process, particularly at deep region of interest when small correlation window length of 3λ is considered, Figure 6. 7(i).

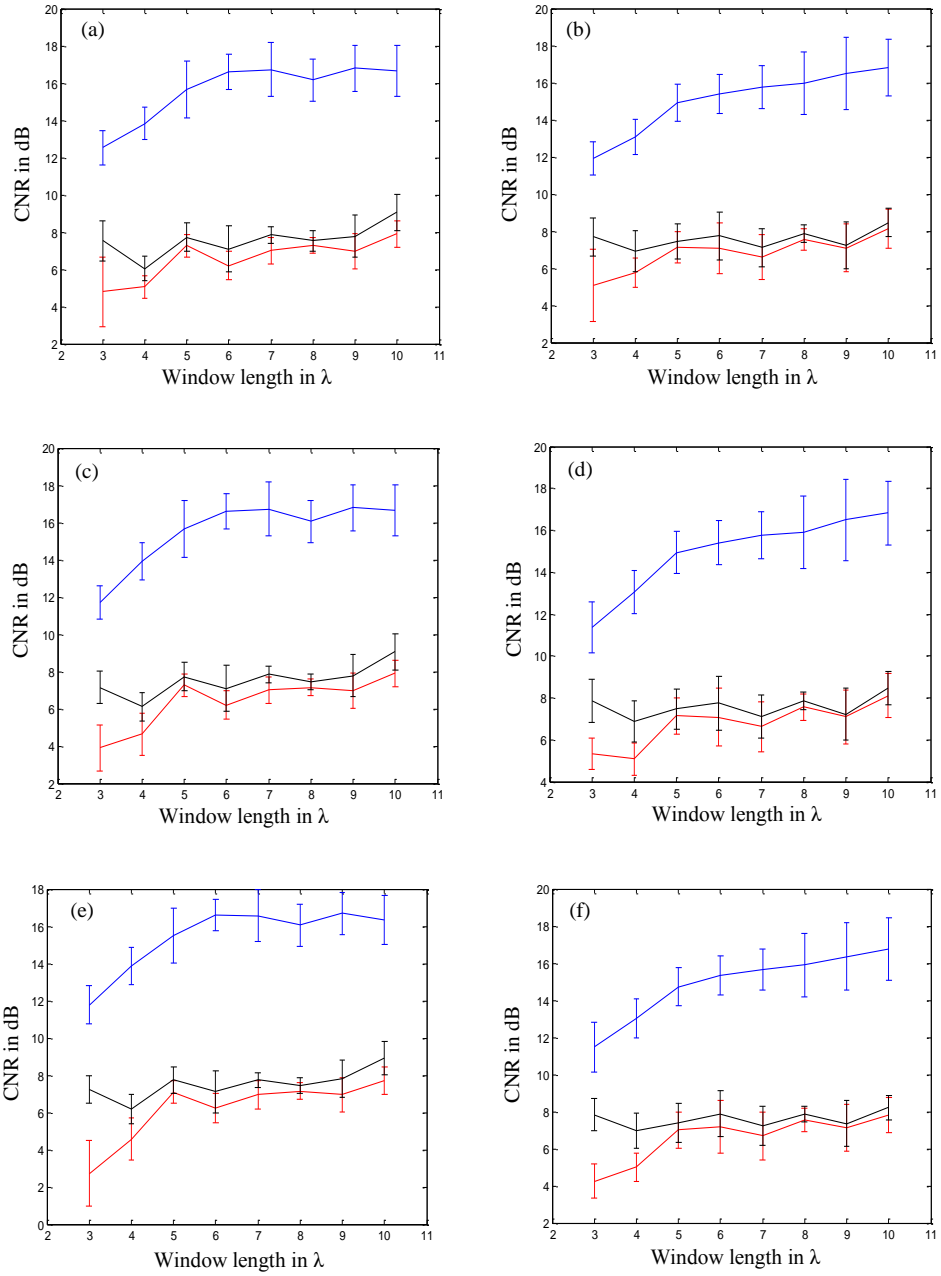


Figure 6. 9 CNR as a function of cross window length for non-refinement (red line), median filter (black line), and refinement (blue line) processes.

6.4.2 Consistency robustness

This section investigates the influences of the refinement process parameters of T_{rd} , T_{cd} , and T_{cc} on strain profile. The initial displacement field is estimated for 3λ correlation window length and 1.4 pre-to-post window length ratio. Figure 6. 10(a,b,c) shows the strain profile for T_{rd} at 0.03, 0.1, 0.2, and 0.3, while $T_{cd}=4$ and $T_{cc}=0.04$. The strain profile at T_{rd} of 0.03 shows superiority in terms of low strain fluctuation, while strain fluctuation increases as T_{rd} increased.

Figure 6. 11(a and b) shows the strain profile for T_{cd} at 0, 2, 4, 6, and 8, while $T_{rd}=0.03$ and $T_{cc}=0.04$. It is clear from Figure 6. 11(a) that strain profiles of T_{cd} at 0, 2, and 4 are in similar performance. At the same time, Figure 6. 11(b) shows how the performance is degraded when T_{cd} increased more than 4. The $T_{cd}=4$ is a maximum number of non-consistency declarations to initiate the process of refinement which represents a probability of 0.5 (relative to eight neighbours) between consistent and non-consistent declaration.

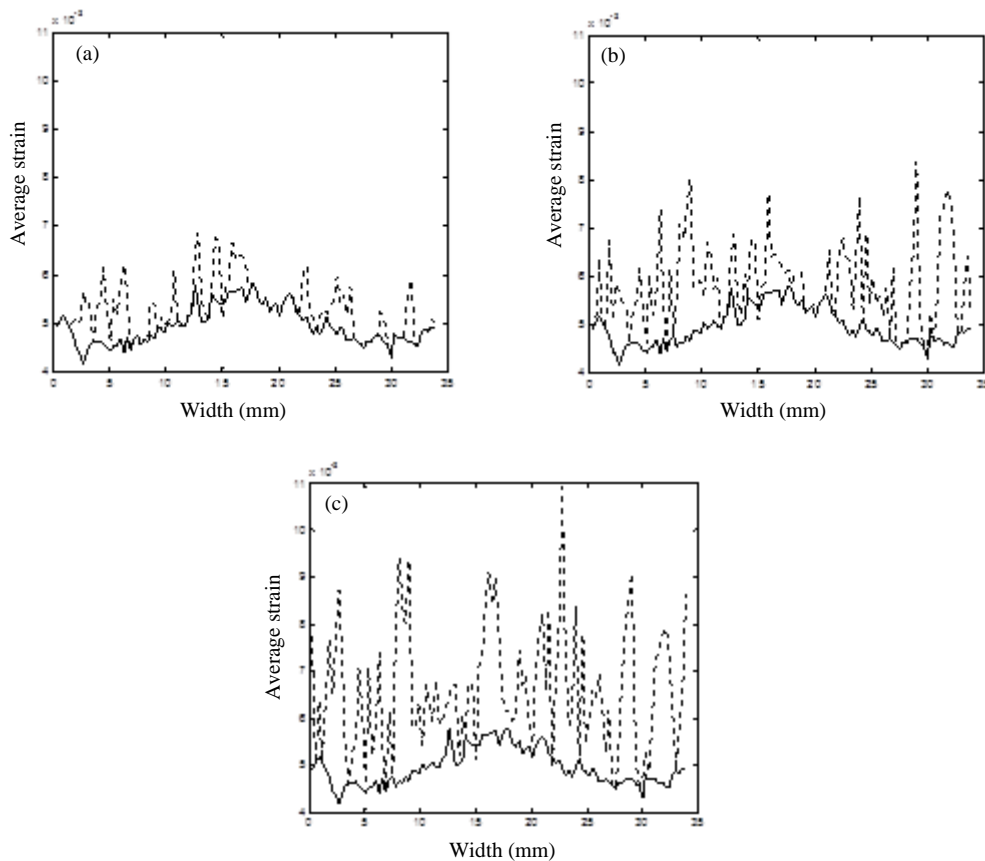


Figure 6. 10 Refined strain profile of (a) $T_{rd}=0.03$ solid line and $T_{rd}=0.1$ dotted line, (b) $T_{rd}=0.03$ solid line and $T_{rd}=0.2$ dotted line, (c) $T_{rd}=0.03$ solid line $T_{rd}=0.3$ and dotted line.

Figure 6. 12(a, b, c) shows the strain profile for T_{cc} of 0.04, 0.1, 0.2, and 0.3, while $T_{rd}=0.03$ and $T_{cd}=4$. It is clear that T_{cc} is less effective than T_{rd} and T_{cd} , but the performance of strain profile is decreased slightly for T_{cc} higher than 0.1. The threshold value of $T_{cc}\leq 0.1$ can be considered as optimal value that prevents any deviation in median value from its actual. The deviation in median value could be happen for any transition (prompt change) due to an increase in the number of inconsistent neighbours, Figure 6. 1(h).

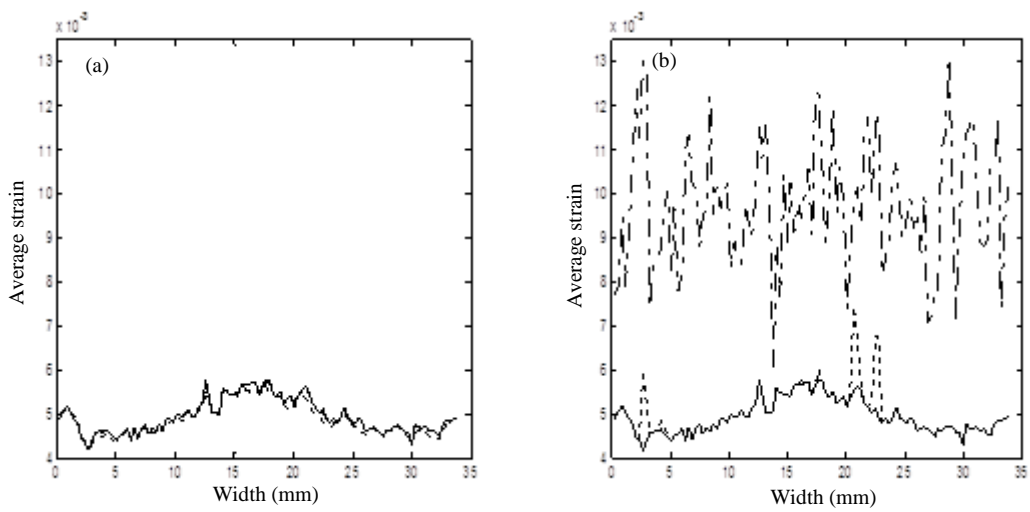


Figure 6. 11 Refined strain profile of (a) $T_{cd}=0$ dotted line, $T_{cd}=2$ dash-dot line and $T_{cd}=4$ solid line, (b) $T_{cd}=4$ solid line, $T_{cd}=6$ dotted line and $T_{cd}=8$ dash-dot line.

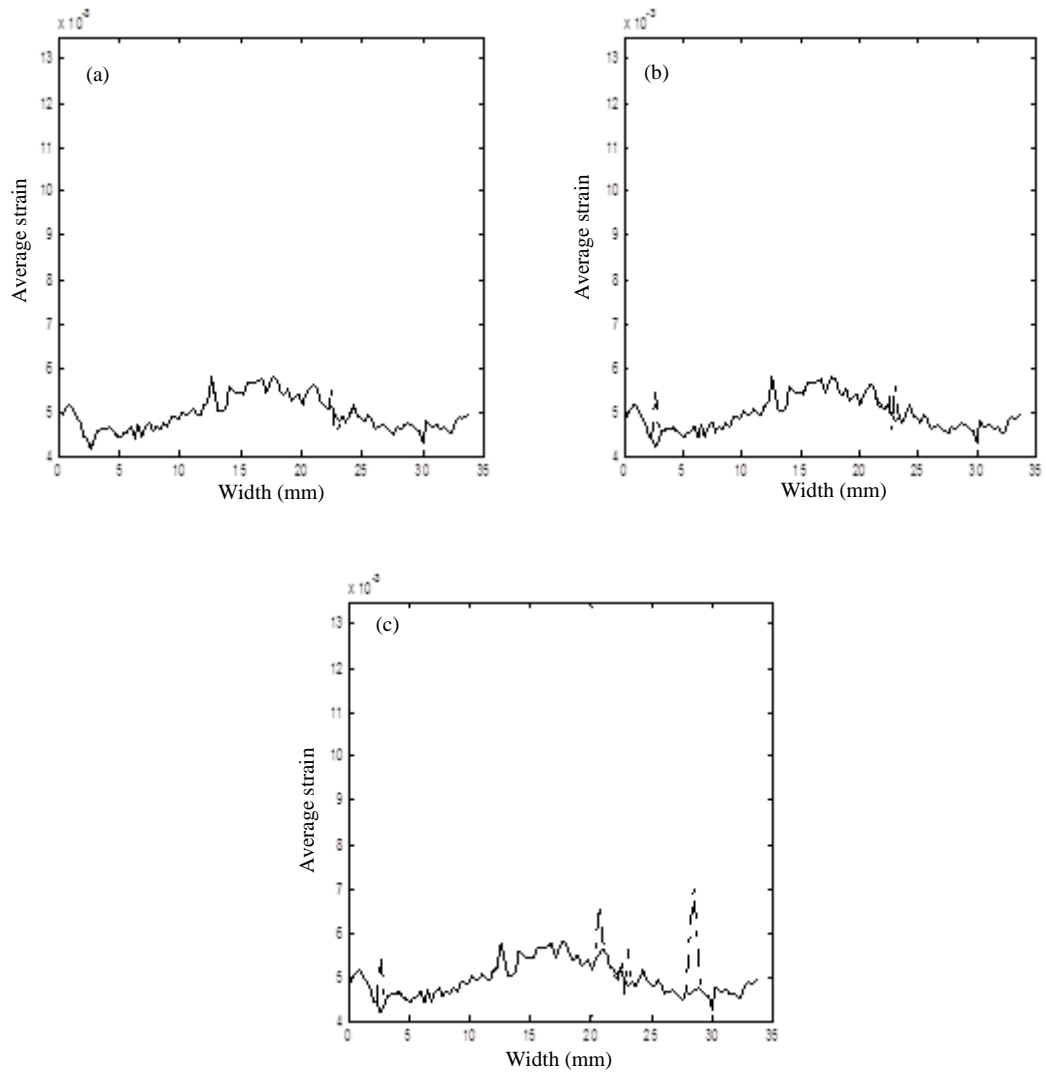


Figure 6. 12 Refined strain profile of (a) $T_{cc}=0.04$ solid line and $T_{cc}=0.1$ dash-dot line. (b) $T_{cc}=0.04$ solid line and $T_{cc}=0.2$ dash-dot line. (c) $T_{cc}=0.04$ solid line and $T_{cc}=0.3$ dash-dot line.

6.4.3 Investigation of large-scale compression

Ultimately, it is feasible to illustrate the effectiveness of the refinement process for applied compression of $>1\%$ based on optimal algorithm parameters. Raw data of before compression and after axial compression of 2%, 3% and 4% are processed to estimate displacement and strain fields, as follows;

A. 2% applied compression:

The initial displacement field is estimated using correlation window length of 4λ , pre-to-post window length ratio of 1.6, and 50% sequential window overlap. While, refined displacement field is estimated using $T_{cd}=4$, $T_{rd}=0.03$, and $T_{cc}=0.08$. Figure 6. 13 shows in (a, c, and e) displacement and in (b, d, and f) strain fields for three processes of non-refinement in (a and b), 3x3 median filter in (c and d), and refinement in (e and f) at 2% compression. Figure 6. 13(a) shows initial displacement with estimation outliers that have been developed severely at region of depth $>30\text{mm}$. Figure 6. 13(b) shows how these outliers reduce the effectiveness of strain in terms of regional contrast and warm noise. At the same time, even 3x3 median filter process removes most of the outliers see Figure 6. 13(c), but strain field of Figure 6. 13(d) is noisy with low regional contrast. In Figure 6. 13(e and f), refinement process produces outlier free displacement field and smooth enough strain field.

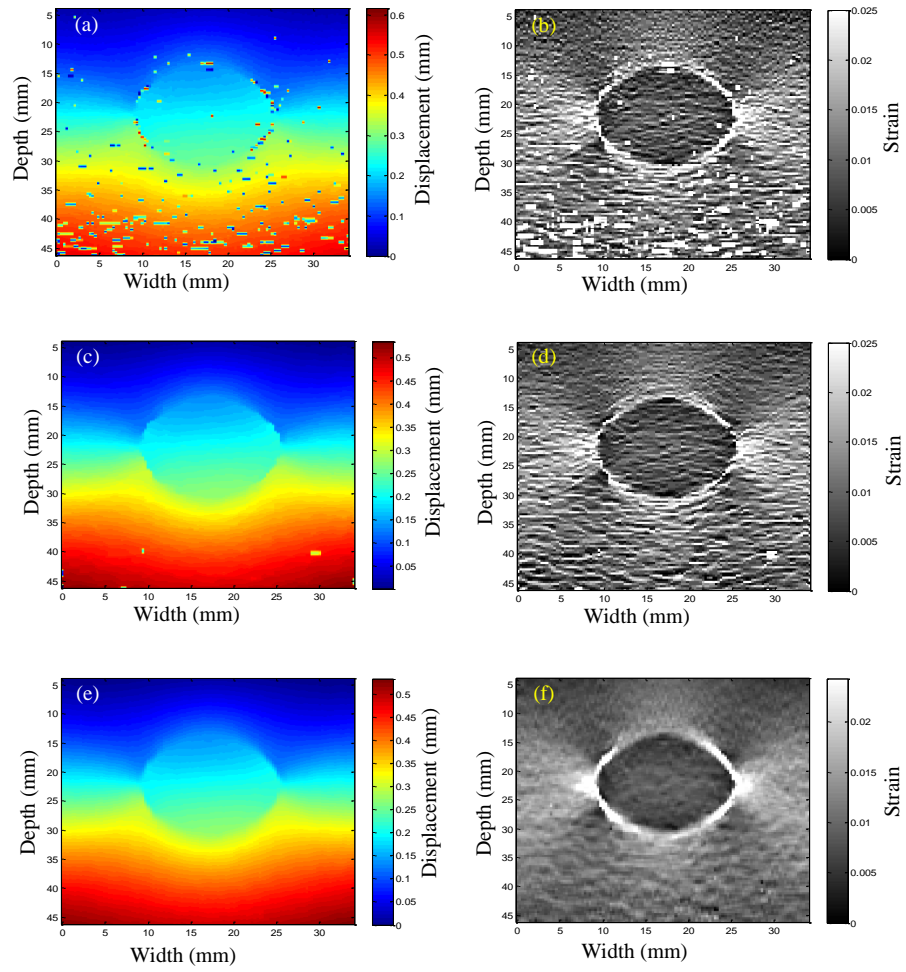


Figure 6. 13 (a,c,e) Displacement and (b,d, f) strain fields of heterogeneous TMM (a and b) without refinement, (c and d) median filter and (e and f) with refinement processes at 2% applied compression.

B. 3% applied compression:

The initial displacement field is estimated using correlation window length of 6.5λ , pre-to-post window length ratio of 1.6, and 50% sequential window overlap. While, refined displacement field is estimated using $T_{cd}=4$, $T_{rd}=0.03$, and $T_{cc}=0.1$. Figure 6. 14 shows in (a, c, and e) displacement and in (b, d, and f) strain fields for three processes of non-refinement in (a and b), 3x3 median filter in (c and d), and refinement in (e and f) at 3% compression. Figure 6. 14(a) shows initial displacement with estimation outliers that have kept in a similar rate of occurrence as in 2% compression by empirical optimization of correlation windows length. Figure 6. 14(b) shows how these outliers reduce the effectiveness of strain in terms of regional contrast and worm noise. However, 3x3 median filter process is failed to remove some complex outliers as shown Figure 6. 14(c) that reduces the contrast of strain field Figure 6. 14(d). As expected, the refinement process is able to remove these complex outliers and produces smooth strain field, Figure 6. 14(e and f).

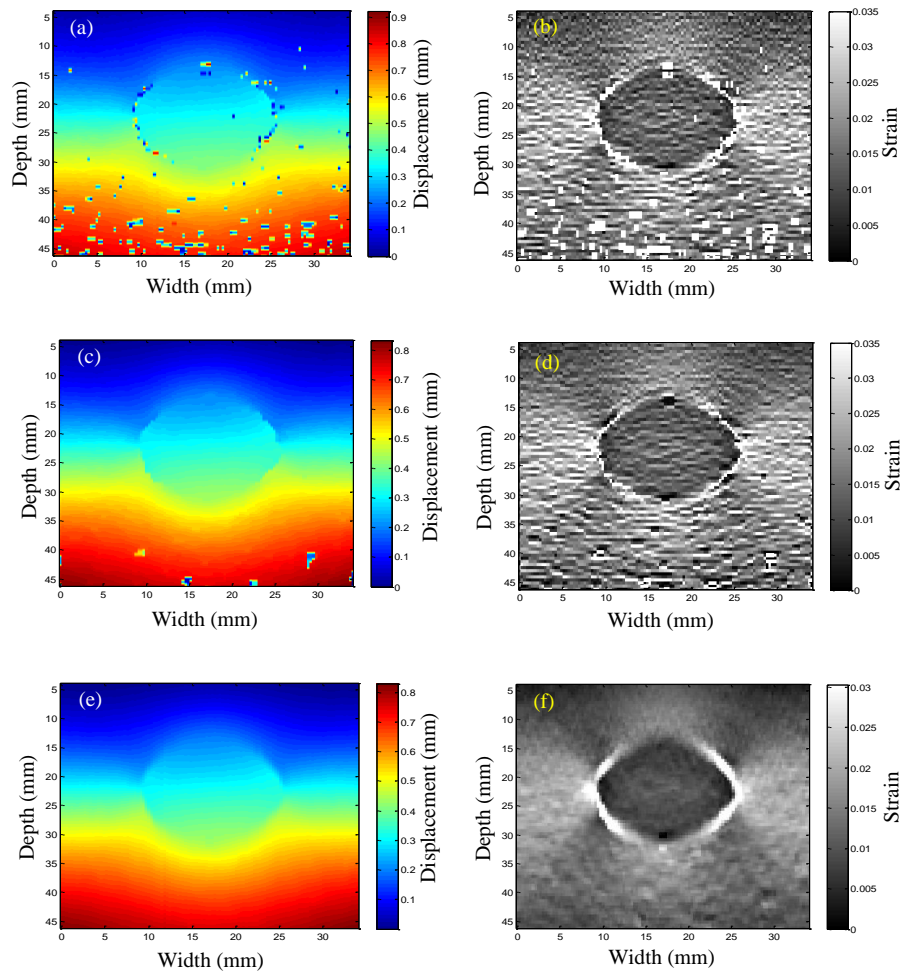


Figure 6. 14 (a, c, e) Displacement and (b, d, f) strain fields of heterogeneous TMM (a and b) without refinement, (c and d) median filter and (e and f) with refinement processes at 3% applied compression.

C. 4% applied compression:

The initial displacement field is estimated using correlation window length of 8λ , pre-to-post window length ratio of 1.8, and 50% sequential window overlap. While, refined displacement field is estimated using $T_{cd}=4$, $T_{rd}=0.03$, and $T_{cc}=0.1$. Figure 6. 15 shows in (a, c, and e) displacement and in (b, d, and f) strain fields for three processes of non-refinement in (a and b), median filter in (c and d), and refinement in (e and f) at 4% compression. Figure 6. 15(a) shows initial displacement with estimation outliers that have been still in low rate of occurrence as in 2% and 3% compressions by empirical optimization of correlation windows length. Figure 6. 15(b) shows how these outliers reduce the effectiveness of strain in terms of regional contrast. Similarly, 3x3 median filter process has failed again to remove some complex outliers as shown Figure 6. 15(c), that reduces the contrast of strain field as shown in Figure 6. 15(d). Refinement process regularizes most of these complex outliers and some are alleviated to support strain to be in acceptable contrast as shown in Figure 6. 15(e and f). It is also clear the performance of refinement process is slightly degraded at 4% compression due to a development of decorrelation noise which is a clear sign that 2D tracking is substantial for higher compression of $>4\%$.

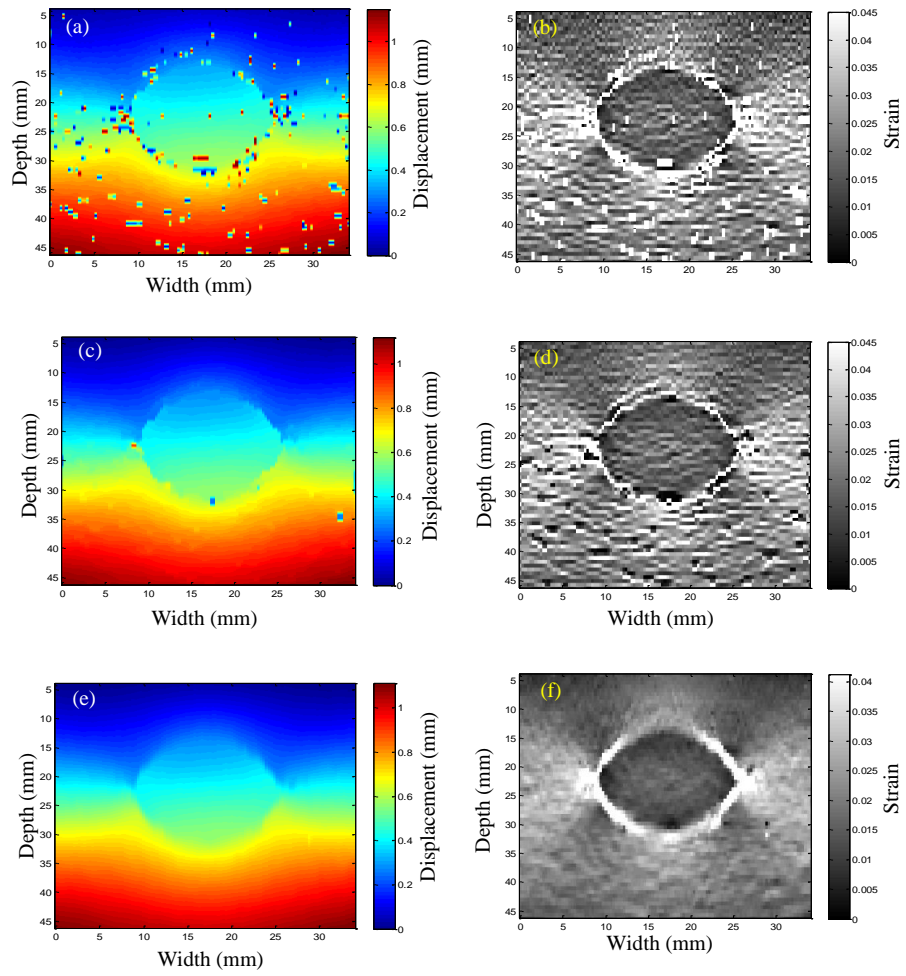


Figure 6. 15 (a, c, e) Displacement and (b, d, f) strain fields of heterogeneous TMM (a and b) without refinement, (c and d) median filter and (e and f) with refinement processes at 4% applied compression.

6.4.4 Investigation of freehand compression

Figure 6. 16 shows the displacement and strain fields of freehand axial compression. The compression force was applied by an operator hand, while holding the transducer-plate adapter. Using 3λ correlation window length and 1.2 pre-to-post window length ratio to produce the initial displacement field that is shown in Figure 6. 16(a). The displacement estimation outliers in the initial displacement field corrupts the visualization of low strain region of interest, Figure 6. 16(b). Figure 6. 16(c) shows how the 3×3 median filter is only able to regularize some of these outliers where some others exist. The existence of estimation outliers and non-smooth gradient displacement reduce the contrast of strain field, Figure 6. 16(d). On the other hand, the refinement process of parameters $T_{cd}=4$, $T_{rd}=0.03$, $T_{cc}=0.1$ completely regularizes the displacement field and provides smooth enough gradient displacement, Figure 6. 16(e). In Figure 6. 16(f), the low strain region (hard inclusion) is easy to be differentiated from higher strain background. The strain field produced from refined displacement is superior than those produced the displacement without refinement and with 3×3 median filter.

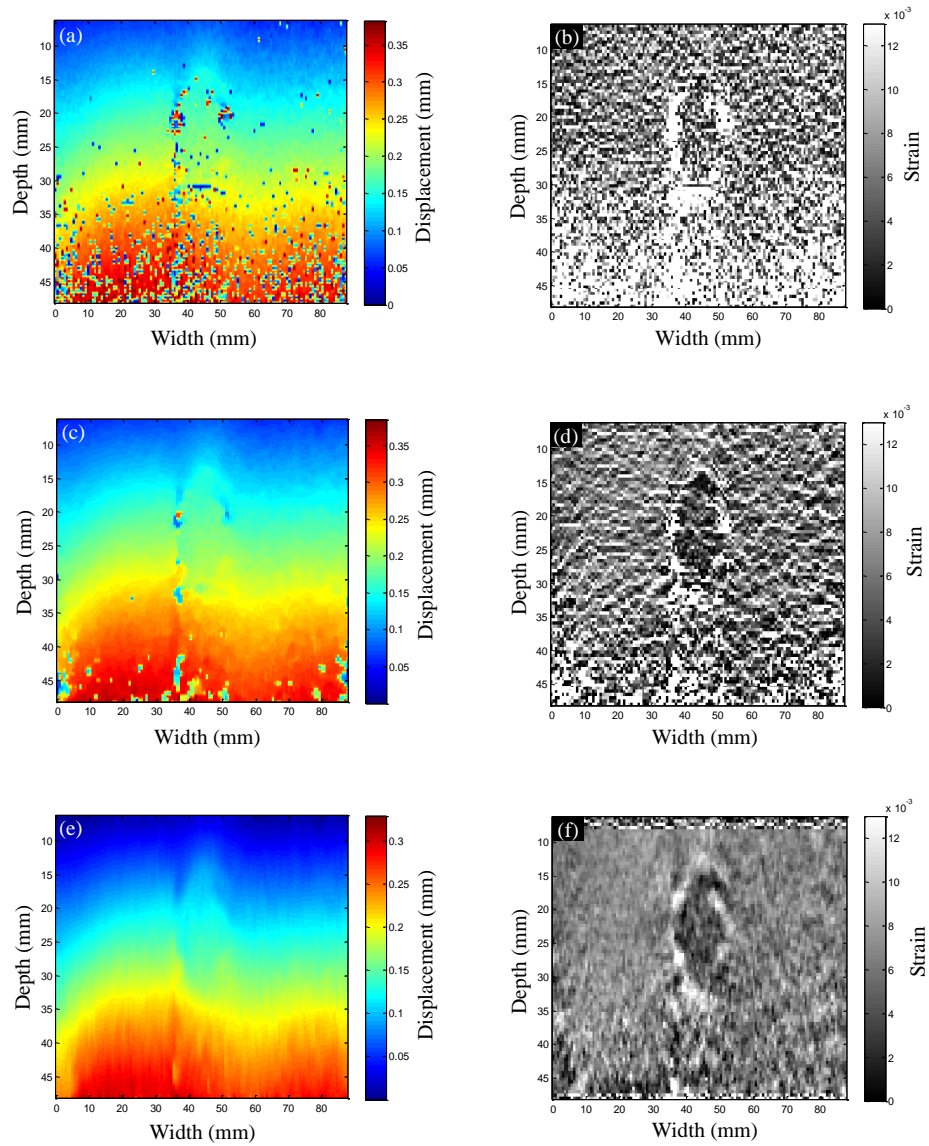


Figure 6. 16 (a, c e) Displacement and (b, d f) strain fields of freehand compression over heterogeneous TMM using 5MHz transducer-plate adapter, raw data process (a and b) without refinement, (c and d) median filter and (e and f) with refinement.

Figure 6. 17 shows the performance of refinement process when the freehand compression tilts in one side. The displacement fields Figure 6. 17(a,c,e) shows tilting in displacement vectors, which means a diagonal deviation of the scatterers motion. It is also clear that the strain field of refinement process has a unique contrast and the inclusion is easy to be visualized, Figure 6. 17(b,d,f).

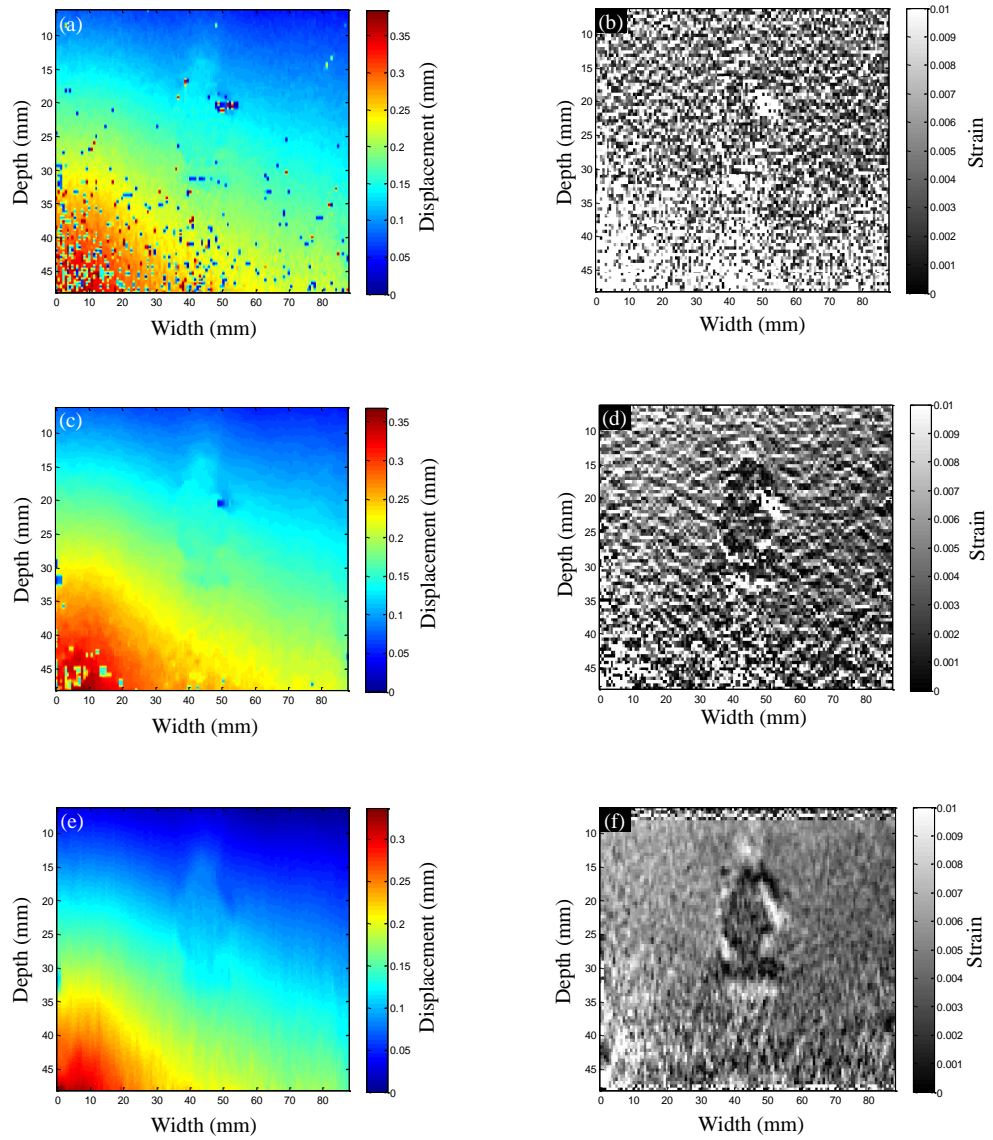


Figure 6. 17 (a, c e) Displacement and (b, d f) strain fields of freehand compression over heterogeneous TMM using 5MHz transducer-plate adapter, raw data process (a and b) without refinement, (c and d) median filter and (e and f) with refinement.

Figure 6. 18 shows displacement and strain fields, which were produced by freehand compression of using the transducer physical surface (without plate) for compression. Figure 6. 18 shows in (a, c, and e) displacement fields and in (b, d, and f) strain fields for non-refinement in Figure 6. 18(a and b), 3x3 median filter in Figure 6. 18(c and d), and refinement in Figure 6. 18(e and f). In Figure 6. 18(a) the estimation outliers are shown to be higher compared to Figure 6. 16(a) and Figure 6. 17(a). An increase in estimation outliers indicates that freehand compression using transducer physical surface is subject to additional decorrelation noise. However, the refinement process is able to illuminate these outliers and produces outlier free displacement field Figure 6. 18(e). The performance of refinement process is superior compared to non-refinement and 3x3 median processes Figure 6. 18(a and c). The strain field of Figure 6. 18(f) shows a differentiable low strain region (hard inclusion), which is easy to be recognized relative to the background (soft region). While at the same time strain fields of Figure 6. 18(b and d) are non-differentiable and contaminated with huge amount of worm noise. Figure 6. 18 confirms the ability of using freehand compression by transducer physical surface.

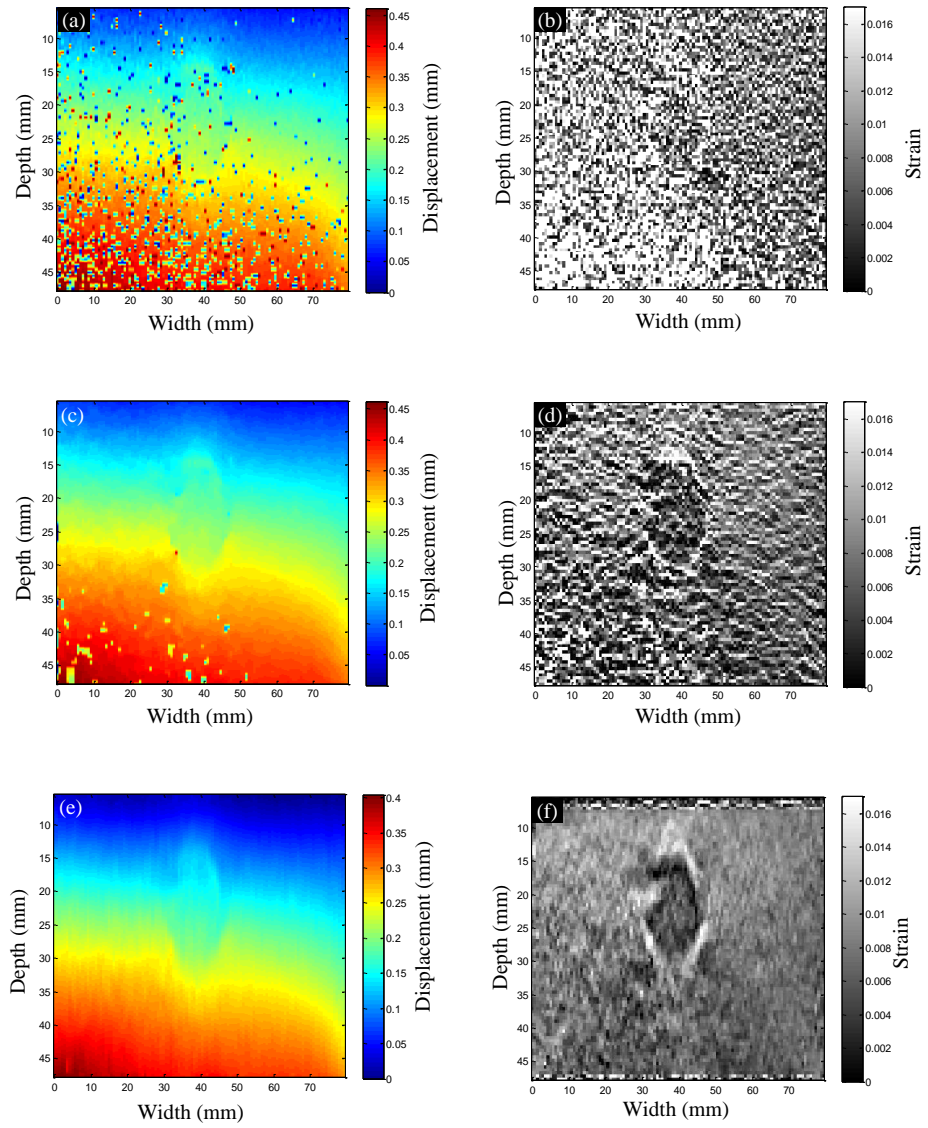


Figure 6. 18 (a, c e) Displacement and (b, d f) strain fields of freehand compression over heterogeneous TMM using 5MHz transducer, raw data process (a and b) without refinement, (c and d) median filter and (e and f) with refinement.

6.5 Conclusion

Pre-compression and post-compression raw data acquired using DYNARAY ultrasonic Phased Array Controller to test a newly proposed refinement algorithm for strain field mapping. Initial displacement field is estimated using cross-correlation tool for optimal small windows length that exhibits acceptable spatial resolution. A refinement process was proposed to eliminate displacement estimation outliers. The performance of the proposed algorithm of refinement compares favourably for estimation of non-refinement and 3x3 median filter processes in terms of visual and quantitative comparison. In visual comparison, refinement processing shows an ability to recognize the imbedded hard inclusion. While quantitative measurement of SNR and CNR of strain, shows superiority of refinement against non-refinement and 3x3 median filter processes.

The robustness of the refinement process was also investigated in terms visual comparison for the situation of applied compression scale 2%, 3%, and 4%. The refinement process exhibits superiority against both of non-refinement and 3x3 median filter processes.

Freehand compression was also applied over heterogeneous TMM using transducer-plate adapter and transducer physical surface alone, the raw data is acquired while the compression applied for low frame rate of 2frame/second. In which the refinement algorithm was shown to be superior against non-refinement and 3x3 median filter processes. The experiment of freehand compression was shown to be successful even when the freehand compression tilts in one side. In addition, using transducer physical surface only for compression is shown to be promises toward clinic practice situation.

Chapter 7

Conclusions and Future Works

7.1 Conclusions

The main aim of this research study was accomplished by presenting a new technique of ultrasound speckle tracking for strain mapping. The new algorithm of refinement was validated using proposed simulation models and presented experimental models. Validation by biological tissue of using i.e. left ventricle is addressed in future works of this thesis.

The results from the simulation model are in good agreement with the results from experiment scenarios. This agreement motivates us to simulate more complex models before conducting experiments. The agreement of experiment and simulation results confirmed that the experimental set-up of using DYNARY ultrasound and emulated TMM models can be extended for more complex situations. These situations correspond to clinic practice situations. In this thesis, the proposed algorithm of processing the raw data before and after compression was shown to be robust against large-scale compression and freehand compression. The proposed algorithm provides qualitative strain field in an acceptable spatial resolution in the order of few wavelengths.

The fundamentals concept of ultrasound elastography was introduced in chapter 2. Chapter 2 was explained the ultrasound system, artefacts, and technology. In chapter 3, a principle of ultrasound scatterer theory was presented. This chapter was also introduced the fundamentals of an interaction of pulse each ultrasound and biological tissue. The literature review of previous work was also presented in chapter 3.

In chapter 4, the simulation algorithm of producing raw data of before and after compression was presented. The proposed algorithm combines Field II program and FEM program to move the scatterers according to the displacement vector of the

simulation model. The bases of the algorithm were introduced for compression scale of 0.2%. The displacement field and strain field of simulation model were compared favourably with the numerical analyses of FEM program. In this chapter, we also have shown how performance of the algorithm degrades at 1% applied compression.

In chapter 5, data from experiment scenarios and simulation were processed. The refinement processing was introduced to cope decorrelation noise development due to an increase in compression scale for 1% compression. The performance of refinement process was validated by experiment and simulation models. The results of experiment and simulation data are compared favourably. The performance of refinement process was shown to be subject to increased estimation outliers at compression scale of 2%.

In chapter 6, the robustness of the refinement process was increased by including an exclusion of inconsistent neighbours into recalculation process. The effectiveness of refinement process was shown to be increased for a large-scale of 2%-4% compressions.

In chapter 6, freehand compression of using transducer-plate adaptor and transducer physical surface were also performed. This experiment has significantly opened the direction of the research toward real-time processing. The real-time processing is important to improve the quality of estimation. This was achieved by observing outcome on time, and then changing the orientation and the scale of compression force accordingly.

7.2 Future Works

In this section a recommendation for the future works are highlighted based on the conclusion of the results from simulation models and experiment scenarios. According to the improvement in the performance of the refinement process against large-scale compression, it is recommended to test the refinement process for the situation of small size hard inclusion. The test would begin by first using the simulation algorithm that was introduced in chapter 4. The simulation algorithm could then be used to design new models by considering an object with an inclusion of 10mm diameter located at 50mm depth, an object with multiple inclusion of different stiffness. It is also feasible to test the refinement process for simulation models of different biological tissues such as, fibroses tissue of left ventricle, malignant female breast tissue, etc. Validation could then be extended to include experiment scenario of heterogeneous TMM with multiple inclusions with different stiffness, size and depth.

An advanced stage of the future work of this research, would be to implement the algorithm of refinement for real-time processing to determine the strain mapping in clinic practice situation of malignant breast, liver, kidney, and prostate under freehand compression. Then, the real-time processing could be extended to left ventricle contraction phases in echocardiography. A final stage of proposed future work, is to use the freehand compression at different orientation of compression to estimate the axial shear strain in addition to axial strain to differentiate the type of breast tumour (benign or malignant).

Appendix A

Wave Propagation Equation

A pulse-echo ultrasonic system that propagates into homogeneous and heterogeneous media is considered. For simplicity, it is assumed that a one dimensional ultrasound wave propagates in soft tissue with a spatially varying intensity. In normal state, the soft tissue can be considered as stationary medium. On the other hand, propagation of ultrasound wave inside the soft tissue modifies the stationary state in terms of pressure perturbation (p) and density disturbance (ρ). The pressure perturbation and density disturbance causes a local motion that displaces the small elements of the soft tissue [63]. The local motion was employed to track tissue deformation based on acoustic radiation force [64]. In this research, the local motion is ignored, where it is no longer effective due to the external applied compression.

The wave propagating in one dimension is expressed in the form of pressure parameter p as follows [65]:

$$\frac{\partial^2 p}{\partial x^2} - \frac{1}{c_0^2} \frac{\partial^2 p}{\partial t^2} = \left(\frac{\partial}{\partial x} \ln \rho_0 \right) \frac{\partial p}{\partial x} \quad (\text{A.1})$$

where t is the time, and x is the direction of propagation c_0 is the wave velocity with $c_0^2 \equiv (\rho_0 \beta_0)^{-1}$, β_0 is an adiabatic compressibility of the medium is given as $\beta_0 = \frac{1}{\rho_0} \left[\frac{\partial \rho}{\partial p} \right]$.

In a heterogeneous medium, fluctuation (spatial variation) in density $\tilde{\rho}$ and compressibility $\tilde{\beta}$ are defined in terms of constant (ρ_0 and β_0) and spatial mean values ($\bar{\rho}$ and $\bar{\beta}$). A series of analysis allows the heterogeneous wave equation to be written as follows [66]

$$\frac{\partial^2 p}{\partial x^2} - \frac{1}{\bar{c}^2} \frac{\partial^2 p}{\partial t^2} = \frac{1}{\bar{c}^2} \tilde{\beta} \frac{\partial^2 p}{\partial t^2} + \frac{\partial p}{\partial x} \left[\tilde{\rho} \frac{\partial p}{\partial x} \right] \quad (\text{A.2})$$

where the constant wave velocity is $\bar{c}^2 \equiv (\bar{\rho} \bar{\beta})^{-1}$.

In the right hand side of (A.2), the spatially varying terms $\tilde{\beta}$ and $\tilde{\rho}$ represent the property of the medium that produces wave scattering. For the property of homogeneous medium, fluctuations in $\tilde{\beta}$ and $\tilde{\rho}$ are assumed to be constant, and the right hand side in (A.2) is reduced to represent homogeneous wave equation as

$$\frac{\partial^2 p}{\partial x^2} - \frac{1}{c^2} \frac{\partial^2 p}{\partial t^2} = 0 \quad (\text{A.3})$$

assuming that scattering is non observable when wave penetrating through spatially uniform medium.

An interesting wave propagation concept is to highlight the coincidences between electromagnetic and acoustic wave propagation, where both of them have the same properties of reflection, refraction, diffraction, etc. Parameters of compressibility and density for acoustic have been analogous to the permittivity and permeability of electromagnetic wave in term of their influence over wave propagation equation [67].

A representation of (A.2) in three dimensional form can expressed as follows;

$$\nabla^2 p - \frac{1}{c^2} \frac{\partial^2 p}{\partial t^2} = \frac{1}{c^2} \tilde{\beta} \frac{\partial^2 p}{\partial t^2} + \nabla \cdot [\tilde{\rho} \nabla p] \quad (\text{A.4})$$

now p is a function of three dimensional position vector, r , and the time t . The symbols of ∇^2 represents Laplacian operator, ∇ represents gradient operator (*grad*), $\nabla \cdot$ represents divergence operator (*div*).

Then wave equation becomes,

$$\begin{aligned} \nabla^2 p(r, t) - \frac{1}{c^2} \frac{\partial^2 p(r, t)}{\partial t^2} & \quad (A.5) \\ & = \frac{1}{c^2} \frac{\partial^2 p(r, t)}{\partial t^2} \cdot \tilde{\beta}(t) + \text{div}[\tilde{\rho}(r) \cdot \text{grad}.p(r, t)] \end{aligned}$$

where $c^2 = (\rho_0 \beta_0)^{-1}$.

In scattering, an isotropic point source radiator is considered to represent each point source individually, which radiates energy equally in all directions. Thus, Greens' function is the solution of (A.5) with the right hand side equal to a point source radiator, [62].

$$\begin{aligned} P(r, t) = P_i(r, t) & \quad (A.6) \\ & + \int_{-\infty}^{\infty} dt_0 \int_V \left\{ \frac{1}{c^2} \frac{\partial^2 P(r_0, t_0)}{\partial t^2} \cdot \tilde{\beta}(t_0) \right. \\ & \left. + \text{div}[\tilde{\rho}(r_0) \cdot \text{grad}.P(r_0, t_0)] \right\} \frac{\delta\left(\frac{t - t_0 - |r_0 - r|}{c}\right)}{4\pi|r_0 - r|} d^3 r_0 \end{aligned}$$

The Born approximation for a point source radiator term of (A.6) allows us to substitute the incident wave $P_i(r, t)$ traveling through a homogeneous volume of V , instead of $P(r, t)$, for the state of non-substantial difference in incident wave and total wave. A validity of the Born approximation is restricted for weak scattering state (small fluctuation in $\tilde{\rho}$ and $\tilde{\beta}$). However, an existence of observable scattering state corroborates the point source radiator term of (A.6) by an iterative solution of the integration to represent the scattering wave of $P_s(r, t)$ in (A.6) as;

$$P(r, t) = P_i(r, t) + P_s(r, t) \quad (A.7)$$

where, $P_i(r, t)$ is plane wave of angular frequency ω and amplitude P_0 .

$$P_s(r, t) = \int_{-\infty}^{\infty} dt_0 \int_V \left\{ \frac{1}{c^2} \frac{\partial^2 P_i(r_0, t_0)}{\partial t^2} \cdot \tilde{\beta}(t_0) + \text{div}[\tilde{\rho}(r_0) \cdot \text{grad} \cdot P_i(r_0, t_0)] \right\} \frac{\delta\left(\frac{t - t_0 - |r_0 - r|}{c}\right)}{4\pi|r_0 - r|} d^3r_0 \quad (\text{A.8})$$

$$P_i(r, t) = P_0 e^{j(k_i \cdot r - \omega t)} \quad (\text{A.9})$$

By inserting (A.9) into (A.8);

$$P_s(r, t) = P_0 e^{j(\omega t)} \int_{V_0} \left\{ k_i^2 \tilde{\beta}(r_0) - j \text{div} \tilde{\rho}(r_0) \cdot k_i \right\} \frac{e^{j[k_i \cdot r_0 - k|r - r_0|]}}{4\pi|r - r_0|} d^3r_0 \quad (\text{A.10})$$

where a wave-number $k = \frac{\omega}{c} = |k_i|$.

As illustrated in Figure 3. 3, $|r| \gg |r_0|$, where $k_i \cdot r_0 - k|r - r_0| \approx (k_i - k_s) \cdot r_0 - k_r \cdot r$.

$$P_s(r, t) = \frac{P_0 e^{j(kr - \omega t)}}{4\pi r} \int_{V_0} \left\{ k_i^2 \tilde{\beta}(r_0) - j \text{div} \tilde{\rho}(r_0) \cdot k_i \right\} e^{j(k_i - k_s) \cdot r_0} d^3r_0 \quad (\text{A.11})$$

Author's Presentations and Publications

- ✓ Al-azawi, A., J. Soraghan, and I. Glover, *Echocardiography Image Analysis*. Faculty of Engineering, RPD-University of Strathclyde, Jan. 2011, p.106, Glasgow-UK.
- ✓ Al-azawi, A., J. Soraghan, and I. Glover, *Elastography Based Left Ventricle Cardiac Tissue Strain Mapping Using Ultrasound Speckle*. Faculty of Engineering, RPD-University of Strathclyde, June 2012, p.117, Glasgow-UK.
- ✓ Al-azawi, A. and J. Soraghan, *Simulation and In-vitro Validation of Elastography based Signal Processing*. Faculty of Engineering, RPD-University of Strathclyde, June 2013, p.22, Glasgow-UK.
- ✓ Al-azawi, A., J. Dziewierz, J. Soraghan, and S. Inglis, *Elastography, Displacement Field Regularization and Strain Field Smoothing of Ultrasonic Calibration Raw Data*. Annual Symposium of UK's Bioengineering Society, Bioengineering13, Sep. 2013, p. 62-63, Glasgow-UK.
- ✓ Al-azawi, A. and J. Soraghan, *Dynamic Ultrasound Scatterer Simulation Model Using Field-II and FEM for Speckle Tracking*. International Conference On Biotechnology, Bioengineering and Bioprocess Engineering, Sept. 2013, Rome-Italy.
- ✓ Al-azawi, A. and J. Soraghan, *Dynamic Ultrasound Scatterer Simulation Model Using Field-II and FEM for Speckle Tracking*. International Journal of Medical, Pharmaceutical Science and Engineering, 2013. 7: p. 77-82.
- ✓ Al-azawi, A., J. Dziewierz, J. Soraghan, S. Inglis, and A. Gachagan, *Ultrasound Elastography: Axial Displacement Field Refinement of Anthropomorphic Phantom*. Under revision for resubmission to IEEE Transactions on Ultrasonics, Ferroelectrics and Frequency Control.
- ✓ Al-azawi, A., J. Dziewierz, J. Soraghan, S. Inglis, and A. Gachagan, *Ultrasound Elastography: Performance Evaluation of Displacement Field Refinement For Large Scale Compression*. Under editing for submission to 4th MICCAI 2015 Workshop on Clinical Image-based Procedures: Translational Research in Medical Imaging, CLIP 2015, Munich, Germany.
- ✓ Al-azawi, A., J. Dziewierz, J. Soraghan, S. Inglis, and A. Gachagan, *Ultrasound Elastography: Performance Evaluation of Displacement Field Refinement For Freehand Compression*. Under editing for submission to 3rd International Conference on Biological and Medical Sciences, APCBEES-ICBMS 2015, Shanghai, China.

References

- [1]. Rivaz, H., et al., *Real-time regularized ultrasound elastography*. IEEE TRANSACTIONS ON MEDICAL IMAGING, 2011. 30(4): p. 928-945.
- [2]. <http://field-ii.dk/?examples.html>.
- [3]. Ophir, J., et al., *Elastography: Ultrasonic estimation and imaging of the elastic properties of tissues*. Proceedings of the Institution of Mechanical Engineers, Part H: Journal of Engineering in Medicine, 1999. 213(3): p. 203-233.
- [4]. VARGHESE, T., et al., *Ultrasonic Imaging of Myocardial Strain Using Cardiac Elastography*. ULTRASONIC IMAGING, 2003. 25: p. 1-16.
- [5]. TANTER, M., et al., *Quantitative assessment of breast lesion viscoelasticity: initial clinical results using supersonic shear imaging*. Ultrasound in Med. & Biol., 2008. 34(9): p. 1373–1386.
- [6]. NGUYEN, N.Q., *OBJECTIVE ASSESSMENT OF SONOGRAPHIC QUALITY FOR BREAST CANCER IMAGING*. University of Illinois, 2012. DISSERTATION.
- [7]. OPHIR, J., et al., *ELASTOGRAPHIC IMAGING*. Ultrasound in Med. & Biol., 2000. 26: p. S23–S29.
- [8]. Thitaikumar, A., et al., *Breast tumor classification using axial shear strain elastography: a feasibility study*. Phys Med Biol, 2008. 53(17): p. 4809-23.
- [9]. Ophir, J., et al., *Elastography: a quantitative method for imaging the elasticity of biological tissues*. Ultrasonic Imaging, 1991. 13: p. 111-134.
- [10]. OPHIR, J., et al., *ELASTOGRAPHIC IMAGING*. Ultrasound in Med. & Biol., 2000. 26(Supplement 1): p. S23–S29.
- [11]. Pellot-Barakat, C., et al., *Ultrasonic Elasticity Imaging as a Tool for Breast Cancer Diagnosis and Research*. Current Medical Imaging Reviews, January 2006. 2(1): p. 157.
- [12]. Hall, T.J., Y. Zhu, and C.S. Spalding, *In vivo Real-Time Freehand Palpation Imaging*. Ultrasound in Med. & Biol., 2003. 29(3): p. 427–435.
- [13]. Céspedes, I., et al., *Elastography: Elasticity imaging using ultrasound with application to muscle and breast in vivo*. Ultrason. Imag., 1993. 15(2): p. 73-88.
- [14]. Konofagou, E.E., J. D’hooge, and J. Ophir, *Myocardial elastography a feasibility study in vivo*. Ultrasound in Med. & Biol., 2002. 28(4): p. 475–482.
- [15]. Szabo, T.L., *Chapter 1 - Introduction*, in *Diagnostic Ultrasound Imaging: Inside Out (Second Edition)*, T.L. Szabo, Editor 2014, Academic Press: Boston. p. 1-37.
- [16]. Szabo, T.L., *Chapter 3 - Acoustic Wave Propagation*, in *Diagnostic Ultrasound Imaging: Inside Out (Second Edition)*, T.L. Szabo, Editor 2014, Academic Press: Boston. p. 55-80.
- [17]. Szabo, T.L., *Chapter 16 - Elastography*, in *Diagnostic Ultrasound Imaging: Inside Out (Second Edition)*, T.L. Szabo, Editor 2014, Academic Press: Boston. p. 699-733.
- [18]. Chuang, B., et al. *Interpreting ultrasound elastography: Image registration of breast cancer ultrasound elastography to histopathology images*. in *Biomedical Imaging: From Nano to Macro, 2010 IEEE International Symposium on*. 2010.
- [19]. Erkamp, R.Q., et al. *Nonlinear elasticity imaging*. in *Ultrasonics Symposium, 2002. Proceedings. 2002 IEEE*. 2002.
- [20]. Brusseau, E., et al., *2-D Locally Regularized Tissue Strain Estimation From Radio-Frequency Ultrasound Images: Theoretical Developments and Results on Experimental Data*. IEEE Transactions on Medical Imaging, 2008. 27(2): p. 145-160.

- [21]. Amar, M.E.H., F. Patat, and J.P. Remenieras. *Brain tissue motion estimation: 2D speckle tracking using synthetic lateral phase technique*. in *Ultrasonics Symposium (IUS), 2010 IEEE*. 2010.
- [22]. D'Hooge, J., et al., *Echocardiographic strain and strain-rate imaging: a new tool to study regional myocardial function*. *IEEE Transactions on Medical Imaging*, 2002. 21(9): p. 1022-1030.
- [23]. Jianwen, L., L. Wei-Ning, and E. Konofagou, *Fundamental performance assessment of 2-D myocardial elastography in a phased-array configuration*. *IEEE Transactions on Ultrasonics, Ferroelectrics and Frequency Control*, 2009. 56(10): p. 2320-2327.
- [24]. Jia, C., et al. *3D Elasticity imaging using principal stretches on an open-chest dog heart*. in *Ultrasonics Symposium (IUS), 2010 IEEE*. 2010.
- [25]. Lopata, R.G.P., *2D and 3D Ultrasound Strain Imaging: Methods and in vivo Applications*. PhD Thesis, Radboud University Nijmegen, 2010.
- [26]. Treece, G., et al., *Real-time quasi-static ultrasound elastography*. *Interface Focus*, 2011. Review: p. 1-13.
- [27]. Ophir, J., et al., *Elastography: a quantitative method for imaging the elasticity of biological tissues*. *Ultrasonic Imaging*, 1991. Vol.13: p. 111-134.
- [28]. Bilgen, M. and M.F. Insana, *Error analysis in acoustic elastography. I. Displacement estimation*. *Acoustical Society of America*, 1997. 101(2).
- [29]. Varghese, T. and J. Ophir, *Enhancement of echo-signal correlation in elastography using temporal stretching*. *IEEE Transactions on Ultrasonics, Ferroelectrics and Frequency Control*, 1997. 44(1): p. 173-180.
- [30]. Kallel, F. and J. Ophir, *A least-squares strain estimator for elastography*. *Ultrasonic Imaging*, 1997. 19: p. 195–208.
- [31]. Hopkins, D., G. Neau, and L.L. Ber, *ADVANCED PHASED-ARRAY TECHNOLOGIES FOR ULTRASONIC INSPECTION OF COMPLEX COMPOSITE PARTS*. *International Workshop SMART MATERIALS, STRUCTURES & NDT in AEROSPACE 2011*.
- [32]. Feigenbaum, H., W.F. Armstrong, and T. Ryan, *Echocardiography*. Lippincott Williams & Wilkins, 15 Jan. 2004. 6th Edition (chapter 2): p. 25.
- [33]. Hoskins, P., K. Martin, and A. Thrush, *Diagnostic Ultrasound: Physics and Equipment*. Cambridge University Press, 2010. Second Edition(chapter 1): p. 1-3.
- [34]. Bilgen, M., *Wavelet transform-based strain estimator for elastography*. *IEEE Transactions on Ultrasonics, Ferroelectrics and Frequency Control*, 1999. 46(6): p. 1407-1415.
- [35]. Pesavento, A., et al., *A time-efficient and accurate strain estimation concept for ultrasonic elastography using iterative phase zero estimation*. *IEEE Transactions on Ultrasonics, Ferroelectrics and Frequency Control*, 1999. 46(5): p. 1057-1067.
- [36]. EE, K., et al., *Power spectral strain estimators in elastography*. *Ultrasound in Medicine and Biology*, 1999. vol. 25(no. 7): p. 1115–1129.
- [37]. Righetti, R., J. Ophir, and P. Ktonas, *Axial Resolution in Elastography*. *Ultrasound in Med. & Biol.*, 2003. 28(1): p. 101-113.
- [38]. Righetti, R., J. Ophir, and P. Ktonas, *Axial Resolution in Elastography*. *Ultrasound in Med. & Biol.*, 2002. 28(1): p. 101-113.
- [39]. RIGHETTI, R., S. SRINIVASAN, and J. OPHIR, *LATERAL RESOLUTION IN ELASTOGRAPHY*. *Ultrasound in Med. & Biol.*, 2003. 29(5): p. 695–704.
- [40]. Konofagou, E. and J. Ophir, *A new elastographic method for estimation and imaging of lateral displacements, lateral strains, corrected axial strains and Poisson's ratios in tissues*. *Ultrasound in Medicine and Biology*, 1998. 24: p. 1183–1199.

- [41]. Jensen, J.A. and N.B. Svendsen, *Calculation of pressure fields from arbitrarily shaped, apodized, and excited ultrasound transducers*. IEEE Transactions on Ultrasonics, Ferroelectrics and Frequency Control, 1992. 39(2): p. 262-267.
- [42]. Jensen, J.a., *Field: a Program For simulating Ultrasound systems*. Med. Biol. Eng. Comput, 1996. 34(1 , Part 1): p. 1351-1353.
- [43]. Jensen, J.A. *Simulation of advanced ultrasound systems using Field II*. in *Biomedical Imaging: Nano to Macro, 2004. IEEE International Symposium on*. 2004.
- [44]. Marion, A. and D. Vray, *Toward a real-time simulation of ultrasound image sequences based on a 3-D set of moving scatterers*. IEEE Transactions on Ultrasonics, Ferroelectrics and Frequency Control, 2009. 56(10): p. 2167-2179.
- [45]. Madenci, E. and I. Guven, *THE FINITE ELEMENT METHOD AND APPLICATIONS IN ENGINEERING USING ANSYS*. Springer, 2006.
- [46]. Palmeri, M.L., et al., *A finite-element method model of soft tissue response to impulsive acoustic radiation force*. IEEE Transactions on Ultrasonics, Ferroelectrics and Frequency Control, 2005. 52(10): p. 1699-1712.
- [47]. Lopata, R.G.P., et al., *Performance Evaluation of Methods for Two-Dimensional Displacement and Strain Estimation Using Ultrasound Radio Frequency Data*. Ultrasound in Medicine & Biology, 2009. 35(5): p. 796-812.
- [48]. Feldman, M.K., S. Katyal, and M.S. Blackwood, *US Artifacts*. RadioGraphics, July-August 2009 29 (4): p. 1179-1189.
- [49]. Ophir, J., et al., *Elastography: ultrasonic imaging of tissue strain modulus in vivo*. European Journal of Ultrasound, 1996. 3 p. 49-70.
- [50]. Alam, S.K. and J. Ophir, *The effect of nonlinear signal transformations on bias errors in elastography*. IEEE Transactions on Ultrasonics, Ferroelectrics, and Frequency Control, 2000. 47(1): p. 297-303.
- [51]. Cespedes, I., et al., *Methods for estimation of subsample time delays of digitized echo signals*. Ultrason Imaging, 1995. 17(2): p. 142-71.
- [52]. <http://ultrasonics.bioengineering.illinois.edu/URI/uri-info.asp>.
- [53]. Ashfaq, M., et al., *An ultrasound research interface for a clinical system*. IEEE Transactions on Ultrasonics, Ferroelectrics, and Frequency Control, 2006. 53(10): p. 1759-1771.
- [54]. <http://www.zetec.com/2010/06/dynaray-product-line/>.
- [55]. Azhari, H., *Basics of Biomedical Ultrasound for Engineers*. Wiley-IEEE Press, 2010: p. 5-6.
- [56]. McDicken, W.N. and T. Anderson, *CHAPTER 1 - Basic physics of medical ultrasound*, in *Clinical Ultrasound (Third Edition)*, P.L.A.M.B.J. Weston, Editor 2011, Churchill Livingstone: Edinburgh. p. 3-15.
- [57]. Derin, H. and P.A. Kelly, *Algorithms for the segmentation of speckled images*. in Proc. 22nd Asilomar Corrf: Signals, Syst., Cornput. Graph. Image Processing, Nov. 1988.
- [58]. Heimdal, A., *Doppler based ultrasound imaging methods for noninvasive assessment of tissue viability*. PhD thesis, the Norwegian University of Science and Technology., Sept. 1999.
- [59]. Adams, D. and E. Forsberg, *Conducting a Cardiac Ultrasound Examination*, in *Echocardiography*, P. Nihoyannopoulos and J. Kisslo, Editors. 2009, Springer London. p. 31-46.
- [60]. Zamorano, J.L., *Developments in 3D echocardiography*. European Cardiology, 2009. 5: p. 3-7.
- [61]. Buckberg GD1, W.M., Ballester M, Beyar R, Burkhoff D, Coghlan HC, Doyle M, Epstein ND, Gharib M, Ideker RE, Ingels NB, LeWinter MM, McCulloch AD, Pohost

- GM, Reinlib LJ, Sahn DJ, Sopko G, Spinale FG, Spotnitz HM, Torrent-Guasp F, Shapiro EP., *Left ventricular form and function: scientific priorities and strategic planning for development of new views of disease*. American Heart Association, 2004 Oct 5. 110(14): p. 333-6.
- [62]. Hill, C.R., J.C. Bamber, and G.R.t. Harr, *Physical Principles of Medical Ultrasonics*. John Wiley & Sons Ltd, 2004. Second Edition: p. 193.
- [63]. Hill, C.R., J.C. Bamber, and G.R.t. Harr, *Physical Principles of Medical Ultrasonics*. John Wiley & Sons Ltd, 2004. Second Edition: p. 2.
- [64]. Palmeri, M.L., et al., *Ultrasonic tracking of acoustic radiation force-induced displacements in homogeneous media*. IEEE Transactions on Ultrasonics, Ferroelectrics, and Frequency Control, 2006. 53(7): p. 1300-1313.
- [65]. Hill, C.R., J.C. Bamber, and G.R.t. Harr, *Physical Principles of Medical Ultrasonics*. John Wiley & Sons Ltd, 2004. Second Edition: p. 5.
- [66]. Hill, C.R., J.C. Bamber, and G.R.t. Harr, *Physical Principles of Medical Ultrasonics*. John Wiley & Sons Ltd, 2004: p. 6.
- [67]. Evans, J.A., *Physics in Medical Ultrasound*. The Institute of Physical Sciences in Medicine, 1986. 47: p. 15.
- [68]. Wagner, R.F., M.F. Insana, and D.G. Brown, *Statistical properties of radio-frequency and envelope-detected signals with applications to medical ultrasound*. J. Opt. Soc. Am., May 1987. A/Vol. 4(No. 5).
- [69]. Hill, C.R., J.C. Bamber, and G.R.t. Harr, *Physical Principles of Medical Ultrasonics*. John Wiley & Sons Ltd, 2004. Second Edition: p. 195-196.
- [70]. Hill, C.R., J.C. Bamber, and G.R.t. Harr, *Physical Principles of Medical Ultrasonics*. John Wiley & Sons Ltd, 2004: p. 197-199.
- [71]. O'Donnell, M., et al., *Internal displacement and strain imaging using ultrasonic speckle tracking*. IEEE Transactions on Ultrasonics, Ferroelectrics and Frequency Control, 1994. 41(3): p. 314-325.
- [72]. Skovoroda, A.R., et al., *Theoretical analysis and verification of ultrasound displacement and strain imaging*. IEEE Transactions on Ultrasonics, Ferroelectrics and Frequency Control, 1994. 41(3): p. 302-313.
- [73]. Lindop, J.E., et al., *Phase-based ultrasonic deformation estimation*. IEEE Transactions on Ultrasonics, Ferroelectrics and Frequency Control, 2008. 55(1): p. 94-111.
- [74]. Bohs, L.N. and G.E. Trahey, *A Novel Method for Angle Independent Ultrasonic-Imaging of Blood-Flow and Tissue Motion*. IEEE Transactions on Biomedical Engineering, 1991. 38(3): p. 280-286.
- [75]. Chaturvedi, P., M.F. Insana, and T.J. Hall, *2-D companding for noise reduction in strain imaging*. IEEE Transactions on Ultrasonics, Ferroelectrics and Frequency Control, 1998. 45(1): p. 179-191.
- [76]. Zhu, X., et al. *Displacement and strain estimation based on numerical optimization method with powell algorithm and wavelet analysis in ultrasound elastography*. in *4th International Congress on Image and Signal Processing 2011*.
- [77]. Insana, M.F., et al. *Signal processing strategies in acoustic elastography*. in *Ultrasonics Symposium, 1996. Proceedings., 1996 IEEE*. 1996.
- [78]. Brusseau, E., et al., *Axial Strain Imaging Using Local Estimation of the Scalling Factor from RF Ultrasound Signals*. Ultrasonic Imaging, 2000. 22: p. 95-107.
- [79]. Viola, F. and W.F. Walker, *A comparison of the performance of time-delay estimators in medical ultrasound*. IEEE Transactions on Ultrasonics, Ferroelectrics and Frequency Control, 2003. 50(4): p. 392-401.

- [80]. Céspedes, I. and J. Ophir, *Reduction of image noise in elastography*. Ultrasonic Imaging, 1993. 15: p. 89-102.
- [81]. Pellot-Barakat, C., et al., *Ultrasound elastography based on multiscale estimations of regularized displacement fields*. IEEE TRANSACTIONS ON MEDICAL IMAGING, 2004. 23(2): p. 153-163.
- [82]. M, M. and O. S, *Noninvasive method for the assessment of subcutaneous oedema*. Medical and Biological Engineering and Computing, 1986. 24(4): p. 393-398.
- [83]. Ophir, J., et al., *Elastography*. Optical and acoustical imaging of biological media, 2001. 2(IV): p. 1193–1212.
- [84]. Ophir, J., et al., *Elastography: Imaging the elastic properties of soft tissues with ultrasound*. Med Ultrasonics, 2002. 29(Winter): p. 155-171.
- [85]. T, V., et al., *Direct strain estimation in elastography using spectral cross-correlation*. Ultrasound in Medicine and Biology, 2000. vol. 26(no. 9): p. 1525–1537.
- [86]. SK, A., et al., *Adaptive spectral strain estimators for elastography*. Ultrason Imaging, 2004. 26(3): p. 131-149.
- [87]. Dibattista, A. and J. Noble, *An efficient block matching and spectral shift estimation algorithm with applications to ultrasound elastography*. IEEE Transactions on Ultrasonics, Ferroelectrics, and Frequency Control, 2014. 61(3): p. 407-419.
- [88]. Alam, S.K., J. Ophir, and E.E. Konofagou, *An adaptive strain estimator for elastography*. IEEE Transactions on Ultrasonics, Ferroelectrics and Frequency Control, 1998. 45(2): p. 461-472.
- [89]. Ramalli, A., et al., *Frequency-domain-based strain estimation and high-frame-rate imaging for quasi-static elastography*. IEEE Transactions on Ultrasonics, Ferroelectrics, and Frequency Control, 2012. 59(4): p. 817-824.
- [90]. Hussain, M.A., et al., *Direct and gradient-based average strain estimation by using weighted nearest neighbor cross-correlation peaks*. IEEE Transactions on Ultrasonics, Ferroelectrics and Frequency Control, 2012. 59(8): p. 1713-1728.
- [91]. Bilgen, M. and M.F. Insana, *Error analysis in acoustic elastography. II. Strain estimation and SNR analysis*. Acoustical Society of America, 1997. 101(2): p. 1147-1154.
- [92]. Cespedes, E.I., C.L. de Korte, and A.F.W. van der Steen, *Echo decorrelation from displacement gradients in elasticity and velocity estimation*. IEEE Transactions on Ultrasonics, Ferroelectrics and Frequency Control, 1999. 46(4): p. 791-801.
- [93]. Varghese, T., J. Ophir, and I. Céspedes, *Noise reduction in elastograms using temporal stretching with multicompression averaging*. Ultrason. Med. Biol., 1996. 22(1043-1052).
- [94]. Srinivasan, S., et al., *Analysis of an adaptive strain estimation technique in elastography*. Ultrasonic Imaging, 2002. 24(2): p. 109-118.
- [95]. Kallel, F. and J. Ophir, *Three-dimensional tissue motion and its effect on image noise in elastography*. IEEE Transactions on Ultrasonics, Ferroelectrics and Frequency Control, 1997. 44(6): p. 1286-1296.
- [96]. Varghese, T., et al., *Tradeoffs in elastographic imaging*. Ultrasonic Imaging, 2001. 23: p. 216-248.
- [97]. Chaturvedi, P., M.F. Insana, and T.J. Hall, *Testing the limitations of 2-D companding for strain imaging using phantoms*. IEEE Transactions on Ultrasonics, Ferroelectrics and Frequency Control, 1998. 45(4): p. 1022-1031.
- [98]. Alam, S.K., et al., *A deconvolution filter for improvement of time-delay estimation in elastography*. IEEE Transactions on Ultrasonics, Ferroelectrics and Frequency Control, 1998. 45(6): p. 1565-1572.

- [99]. Liu, K., et al., *A 2D strain estimator with numerical optimization method for soft-tissue elastography*. *Ultrasonics*, 2009 49(8): p. 723-732.
- [100]. Deprez, J.F., et al., *3D estimation of soft biological tissue deformation from radio-frequency ultrasound volume acquisitions*. *Med Image Anal*, 2009. 13(1): p. 116-127.
- [101]. Langeland, S., et al. *A parametric study on processing parameters for two-dimensional cardiac strain estimation: an in-vivo study*. in *Ultrasonics Symposium, 2005 IEEE*. 2005.
- [102]. Xunchang, C., et al., *Lateral speckle tracking using synthetic lateral phase*. *IEEE Transactions on Ultrasonics, Ferroelectrics and Frequency Control*, 2004. 51(5): p. 540-550.
- [103]. Rivaz, H., et al., *Ultrasound elastography: A dynamic programming approach*. *IEEE TRANSACTIONS ON MEDICAL IMAGING*, 2008. 27(10): p. 1373-1377.
- [104]. Jingfeng, J. and T.J. Hall. *6F-3 A Regularized Real-Time Motion Tracking Algorithm Using Dynamic Programming for Ultrasonic Strain Imaging*. in *Ultrasonics Symposium, 2006. IEEE*. 2006.
- [105]. Ramalli, A., et al. *Real-time implementation of a novel algorithm for ultrasound freehand elastography of breast lesions*. in *Acoustics, Speech and Signal Processing (ICASSP), 2014 IEEE International Conference on*. 2014.
- [106]. Chen, H., H. Shi, and V. T., *Improvement of Elastographic Displacement Estimation Using Two-Step Cross-correlation*. *Ultrasonic Med Biol*, 2007. 33(1): p. 48-56.
- [107]. T., V. and O. J., *Characterization of elastographic noise using the envelope of echo signals*. *Ultrasound in Medicine and Biology*, 1998. vol. 24(no. 4): p. 543-555.
- [108]. Lindop, J., et al., *Dynamic Resolution Selection in Strain Imaging*, in *Acoustical Imaging*, I. Akiyama, Editor 2009, Springer Netherlands. p. 33-38.
- [109]. Remley, W.R., *Correlation of signals having a linear delay*. *THE JOURNAL OF THE ACOUSTICAL SOCIETY OF AMERICA*, 1963. 35(1): p. 65-69.
- [110]. Adams, W., J. Kuhn, and W. Whyland, *Correlator compensation requirements for passive time-delay estimation with moving source or receivers*. *IEEE Transactions on Acoustics, Speech and Signal Processing*, 1980. 28(2): p. 158-168.
- [111]. Walker, W.F. and G.E. Trahey, *A fundamental limit on delay estimation using partially correlated speckle signals*. *IEEE Transactions on Ultrasonics, Ferroelectrics and Frequency Control*, 1995. 42(2): p. 301-308.
- [112]. Zahiri-Azar, R. and S.E. Salcudean, *Motion estimation in ultrasound images using time domain cross correlation with prior estimates*. *IEEE Transactions on Biomedical Engineering*, 2006. 53(10): p. 1990-2000.
- [113]. Al-azawi, A. and J. Soraghan, *Dynamic Ultrasound Scatterer Simulation Model Using Field-II and FEM for Speckle Tracking*. *International Journal of Medical, Pharmaceutical Science and Engineering*, 2013. 7: p. 77-82.
- [114]. McCormick, M., N. Rubert, and T. Varghese, *Bayesian regularization applied to ultrasound strain imaging*. *IEEE Transactions on Biomedical Engineering*, 2011. 58(6): p. 1612-1620.
- [115]. Nixon, M.S. and A.S. Aguado, *Feature Extraction and Image Processing*. Elsevier Ltd, 2008. Second edition: p. 91-96.
- [116]. Inglis, S., et al., *An anthropomorphic tissue-mimicking phantom of the oesophagus for endoscopic ultrasound*. *Ultrasound in Med. & Biol.*, 2006. 32(2): p. 249-259.
- [117]. Ramnarine, K.V., T. Anderson, and P.R. Hoskins, *Construction and geometric stability of physiological flow rate wall-less stenosis phantoms* *Ultrasound in Medicine & Biology*, 2001. 27(2): p. 245-250.

- [118]. Institution, B.S., *Ultrasonic - Flow measurement systems - Flow test object*. BS EN 61685:2002, 2002. British Standards Online [online] Available through: University of Edinburgh Library [Accessed 37 August 2013].
- [119]. Burger, W. and M.J. Burge, *Principles of Digital Image Processing*. Springer, 2009: p. 118-124.